# Multi-walled Carbon Nanotubes Mixed Matrix Membranes

***Dissertation***

zur Erlangung des akademischen Grades

Doktor der Naturwissenschaften

(Dr. rer. nat.)

der Technischen Fakultät

der Christian-Albrechts-Universität zu Kiel

**Shahid Majeed**

**Kiel**

**2013**

Gutachter 1: Prof. Dr. Volker Abetz

Gutachter 2: Prof. Dr. Rainer Adelung

Datum der mündlichen Prüfung: 26.03.2013

**Declaration**

I declare that the submitted thesis has been prepared by me and I have not used any helping material other than cited. This thesis has never been submitted to any University or examining body for evaluation. Some parts of dissertation have been published as mentioned below:

- Shahid Majeed, Volkan Filiz, Sergey Shishatskiy, Jan Wind, Clarissa Abetz, Volker Abetz, *Nanoscale Research Letters* **2012**, *7*, 296

- Shahid Majeed, Daniel Fierro, Kristian Buhr, Jan Wind, Bing Du, Adriana Boschetti-de-Fierro, Volker Abetz, *Journal of Membrane Science* **2012**, *403–404*, 101–109

The thesis has been prepared maintaining the Rules of Good Scientific Practice of the German Research Foundation.

Shahid Majeed

Geesthacht, 06.10.2012

## Table of Contents

## List of Figures

## List of Tables

## List of Abbreviations

| | |
|---|---|
| AFM | Atomic Force Microscope |
| AP*i*B-POSS | Aminopropylisobutyl POSS® |
| ATRP | Atom Transfer Radical Polymerization |
| CA | Cellulose Acetate |
| CNTs | Carbon Nanotubes |
| CVD | Chemical Vapor Deposition |
| DMAc | *N, N*-dimethylacetamide |
| DMF | *N, N*-dimethylformamide |
| DMSO | Dimethyl Sulfoxide |
| DWCNTs | Double-walled Carbon Nanotubes |
| GPC | Gel Permeation Chromatography |
| KBr | Potassium Bromide |
| MMCMs | Mixed Matrix Composite Membranes |
| MMMs | Mixed Matrix Membranes |
| MWCNTs | Multi-walled Carbon Nanotubes. |
| MWCNTs-Br | Initiator Modified MWCNTs |
| MWCNTs-*gf*-PMMA | PMMA Modified MWCNTs via “grafting from” Technique |
| MWCNTs-*gt*-PMMA | PMMA Modified MWCNTs via “grafting onto” Technique |
| MWCNTs-$NH_2$ | Amine Functionalized MWCNTs |
| MWCNTs-OH | Hydroxyl Functionalized MWCNTs |
| MWCNTs-P | Purified or Untreated MWCNTs |
| MWCNTs-PPy | Pyrene-POSS Modified MWCNTs |
| PAN | Polyacrylonitrile |
| PBA | 1-pyrenebutyric acid |
| PDMS | Poly(dimethylsiloxane) |
| PES | Poly(ether sulfone) |
| PMMA | Poly(methyl methacrylate) |
| POSS | Polyhedral Oligomeric Silsesquioxanes |
| PPy | Pyrene-POSS |
| PS | Polystyrene |
| PSf | Polysulfone |
| PVDF | Poly(vinylidene fluoride) |
| SEM | Scanning Electron Microscope |
| SWCNTs | Single-walled Carbon Nanotubes |
| TEM | Transmission Electron Microscope |
| TGA | Thermogravimetric Analysis |
| THF | Tetrahydrofuran |

## List of Symbols

| | |
|---|---|
| a | Lattice constant |
| A | Membrane area |
| $a_1$ | Unit vector |
| $a_2$ | Unit vector |
| $C_h$ | Chiral vector |
| D | Diffusivity coefficient |
| D | Pore diameter |
| J | Flux |
| l | membranes thickness |
| L | Permeance |
| $M_n$ | Number average molecular weight |
| $M_t$ | Transition metal |
| $M_w$ | Weight average molecular weight |
| P | Permeability coefficient |
| PDI | Polydispersity index |
| p | Pressure |
| R | Universal gas constant |
| S | Solubility coefficient |
| T | Temperature |
| Vol % | Volume percent |
| $V_p$ | Permeate volume |
| Wt. % | Weight percent |
| Δp | pressure difference |
| $\theta$ | Chiral angle |
| θ | Contact angle |
| Θ | Time lag |
| ρ | Conductivity |
| σ | Surface tension |
| Ω | Resistance |
| Ω/□ | Sheet resistance |
| $\alpha$ | Compaction factor |

## Chapter 1. Introduction

Membrane technology is a major paradigm for separation and purification of mixtures comprised of various components. Unlike conventional separation processes e.g. distillation and adsorption, carried out under complicated operations, membrane technology is advantageous because of the improved efficiency, low energy consumption, and ease of operation. Polymeric membranes are widely used in a variety of separation processes like microfiltration, ultrafiltration, nanofiltration, pervaporation, dialysis, and gas separation [1].

With the development of gas separation processes, conventional membrane materials are reported to possess an inherent drawback i.e. the trade-off between selectivity and permeability of gases. In 1991, Robeson plotted the available data of permeability versus selectivity of polymeric membranes on logarithmic scale. From the plot data a so-called “upper bound” was found which indicates that the polymers with low permeability possess higher selectivity and vice versa [2]. In 2008 the upper bound was reviewed again including new data after 1991 [3]. Fig. 1.1 shows the upper bound correlation of $O_2/N_2$ separation.

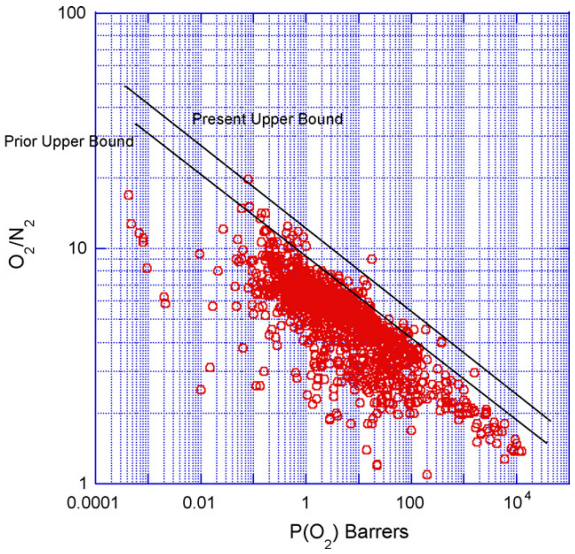


Figure 1.1: Upper bound correlation between $O_2$ permeability and $O_2/N_2$ selectivity [3].

Different attempts have been done to improve the gas separation performance of membranes. Polymer blends and modification of backbone and side chains of conventional polymers have been reported for the improvement of gas separation. The trends to improve the membrane separation have also led to the emergence of an important membrane class, known as mixed matrix membranes (MMMs) [1]. In this membrane type, nano sized fillers are incorporated in conventional polymers. The use of nanoparticles in polymer membrane materials has received considerable attention for the improvement of gas separation properties. Nano sized fillers either improved the separation factor or permeability of gases for conventional membrane materials [4-8].

Porous polymer membranes are a commercially important class of membranes prepared via phase inversion process. The application of porous polymeric membranes includes microfiltration, ultrafiltration, reverse osmosis, and gas separation. They are also used as porous supports in composite membrane fabrication where a thin dense layer acts as the separating barrier and a porous support provides the mechanical stability to the separation layer [9]. The mechanical stability of the porous membranes is a prerequisite for better separation performance. At high transmembrane pressures, the porous structure of the membranes undergoes compaction leading to flux decline [10]. A very promising approach to improve the mechanical stability of the porous membranes is to use organic-inorganic blends for the fabrication of membranes. The presence of an inorganic phase in the form of nanofillers increases the mechanical stability while interactions between polymer and inorganic phase improve the mechanical stability of the membranes by transferring the load from polymer to the filler. The addition of nanoparticles plays also an important role in microporous membranes by controlling the membrane fouling problem, besides improving their mechanical stability and improving the separation performance compared to neat systems [11].

For mixed matrix membranes various nano sized fillers e.g., zeolite, $SiO_2$, and carbon nanotubes (CNTs) etc. have been used in different polymer matrices to obtain the improved separation properties compared to neat polymer matrices [4-8]. CNTs are excellent mass transport channels and appealing membrane fillers and have been widely studied in polymeric membranes during the past decade [12-13]. Also their extraordinary electrical and mechanical properties make them interesting fillers for the preparation of nanocomposite materials [14-15].

The focus of present work is the fabrication of MMMs by incorporating multi-walled carbon nanotubes (MWCNTs) in different polymer matrices i.e., Poly(vinylidene fluoride) (PVDF), polyacrylonitrile (PAN), and Poly(dimethylsiloxane) (PDMS). PVDF and PAN integral asymmetric membranes are prepared by phase inversion technique for ultrafiltration applications and dense PDMS membranes for gas separation processes. The aim of adding MWCNTs in PVDF and PAN is to obtain the porous MMMs with superior properties compared to pure membranes e.g. mechanically more stable, resistant against compaction induced at higher operating pressures, and of improved performance. PDMS is well known for hydrocarbon separation and MWCNTs are incorporated in PDMS to improve the gas separation performance. PDMS MMMs are also cast on porous membrane supports to fabricate the composite membranes where the thin selective PDMS layer acts as the separation barrier. One significant aspect to introduce MWCNTs in PDMS, other than improvement in gas separation, is to obtain membranes with an electrically conductive surface. Owing to their electrical conductivity [14], MWCNTs are expected to improve the surface electrical conductivity of the membranes which may provide the security for their application against electrostatic charging in spiral wound modules having a plastic housing. Electrostatic charging phenomenon can be minimized if the contact surface of the membranes has a surface resistivity lower than a range between $10^6$ Ω/□ and $10^9$ Ω/□ or bulk electrical conductivity above $10^{-6}$ $Sm^{-1}$ [16-17].

Lack of dispersibility and difficult manipulation of CNTs in many common organic solvents is the major problem to obtain well dispersed CNTs in polymer nanocomposites prepared by solvent evaporation. The strong adhesion among CNTs results from van-der-Waals and $\pi$-$\pi$ stacking interactions which lead to the formation of aggregates in the solvents. These aggregates can be demolished by ultrasonication prior to polymer solution preparation, however, CNTs tend to precipitate with the passage of time. Surface functionalization provides a pathway where the surface chemistry of CNTs is altered by the introduction of chemical functional groups and improves their dispersion in different desired solvents [18]. The functional groups are bound on CNTs by physical or chemical attachment. Additionally, the stable dispersion of CNTs in organic solvents triggers their homogeneous dispersion in resultant polymer nanocomposites. In this contribution the functionalization of CNTs by covalent and non covalent bonding is discussed. Polystyrene (PS) and poly(methyl methacrylate) (PMMA) are attached on MWCNTs by covalent bonding using atom transfer radical polymerization (ATRP) technique, and pyrene based polyhedral oligomeric silsesquioxane (pyrene-POSS) is stacked by non covalent bonding ($\pi-\pi$ stacking). Polymers are blended with MWCNTs to fabricate the membranes, e.g. PAN is blended with purified and hydroxyl functionalized MWCNTs, PVDF with purified, hydroxyl, and PMMA modified MWCNTs, and PDMS with purified, pyrene-POSS, and PS modified MWCNTs. The selection of functional groups on MWCNTs is done either on the basis of good interactions of attached functional groups with polymer matrix or improved dispersion of MWCNTs in the solvents being used for the membrane fabrication. PVDF and PAN MMMs were tested for ultrafiltration process and PDMS MMMs were characterized by gas separation.

The thesis is divided into seven chapters. **Chapter 2** overviews the introduction of CNTs and their synthesis, structure, and properties. Methods for functionalization of CNTs are discussed briefly in this chapter. Membranes, their types, fabrication and separation processes are described. **Chapter 3** describes the experimental work and characterization techniques performed in this thesis.

In **chapter 4**, MWCNTs functionalization via covalent and non covalent means is reported with subsequent discussion on the results of functionalization of CNTs. Polystyrene and poly(methyl methacrylate) are grafted from MWCNTs by covalent functionalization and polyhydral oligomeric silsesquioxane (POSS) moiety is immobilized on MWCNTs by non covalent functionalization. **Chapter 5** is devoted to the PVDF MMMs for ultrafiltration process. The dispersibility of CNTs, both functionalized and non-functionalized, in PVDF matrix and their impact on the membranes properties is discussed. **Chapter 6** is about polyacrylonitrile (PAN) MMMs for ultrafiltration process. Impact of purified and surface modified MWCNTs on performance of PAN membranes is evaluated. PDMS MMMs for gas separation are discussed in **chapter 7**. The gas separation properties of PDMS dense films and composite membranes are given along with the methods to develop the conductive PDMS composite membranes. **Chapter 8** summarizes the work done in this thesis and presents an outlook of the thesis.

## 1.1 References


[1] A. F. Ismail, P.S. Goh, S.M Sanip, M. Aziz, Separ. Purif. Technol., 70 (2009) 12–26.

[2] L. M. Robeson, J. Membr. Sci., 62 (1991) 165-185.

[3] L. M. Robeson, J. Membr. Sci., 320 (2008) 390-400.

[4] M. Jia, K. V. Peinemann, R. D. Behling, J. Membr. Sci., 57 (1991) 289-292.

[5] T. W. Pechar, S. Kim, B. Vaughan, E. Marand, V. Baranauskas, J. Riffle, H. K. Jeong, M. Tsapatsis, J. Membr. Sci., 277 (2006) 210-218.

[6] D. Gomes, S. P. Nunes, K. V. Peinemann, J. Membr. Sci., 246 (2005) 13-25.

[7] S. M. Sanip, A. F. Ismail, P. S. Goh, T. Soga, M. Tanemura, H. Yasuhiko, Separ. Purif. Technol., 78 (2011) 208–213.

[8] S. Kim, T. W. Pechar, E. Marand, Desalination, 192 (2006) 330-339.

[9] M. Mulder, Basic Principles of Membrane Technology, 2nd edi., Kluwar Publishers, 1996.

[10] K. Ebert, D. Fritsch, J. Koll, C. Tjahjawiguna, J. Membr. Sci., 233 (2004) 71-78.

[11] J. Kim, B. V. Bruggen, Env. Pollution, 158 (2010) 2335-2349.

[12] D. M. Ackerman, A. I. Skoulidas, D. S. Sholl, J. K. Johnson, Mol. Simulat., 29 (2003) 677-684.

[13] B.J. Hinds, N. Chopra, T. Rantell, R. Andrews, V. Gavalas, L.G. Bachas, Science, 303 (2004) 62–65.
[14] T. W. Ebbesen, H. J. Lezec, H. Hiura, J. W. Bennett, H. F. Ghaeimi, T. Thio, Nature, 382 (1996) 54-56.
[15] J. P. Salvetat, A. J. Kulik, J. M. Bonard, G. a. D. Briggs, T. Stöckli, K. Méténier, S. Bonnamy, F. Béguin, N. A. Burnham, L. Forró, Adv. Mater., 11 (1999) 161-165.
[16] M. Narkis, G. Lidor, A. Vaxman, L. Zuri, J. Electrostatics, 47 (1999) 201-214.
[17] J. Sandler, M. Shaffer, T. Prasse, W. Bauhofer, K. Schulte, A. Windle, Polymer, 40 (1999) 5967-5971.
[18] D. Tasis, N. Tagmatarchis, A. Bianco, M. Prato, Chem. Rev., 106 (2006) 1105-1136.

# Chapter 2. Theoretical Background and State of the Art

## 2.1 Membranes

A membrane is a permeable or semi permeable barrier allowing the transport of same kind or sized molecules and stopping the passage of others (Fig. 2.1). The membrane definition meets the requirement of normal filter, however, by convention the term filter is usually described to the structures used to separate the particular suspensions containing particles larger than 1 to 10 μm [1]. The transport of the molecules can be active or passive where passive transport can be driven by a concentration, pressure, temperature or electric potential difference. The membranes can be natural or synthetic by their origin [2].

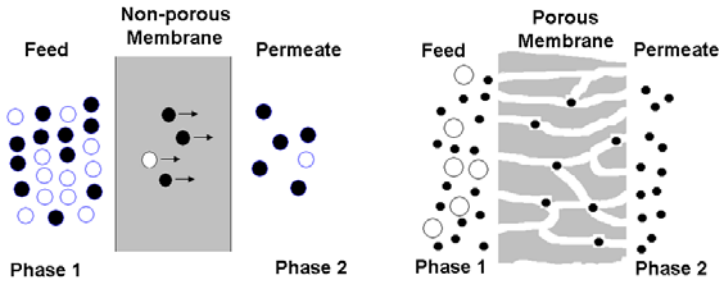


Figure 2.1: Schematic diagram representing the separation of two phases by non-porous and porous membranes.

Synthetic membranes can be categorized into two main classes depending on the constituents of the membranes i.e. inorganic and organic membranes. Inorganic membrane materials include ceramic, glass, and metal etc. and organic membrane materials mainly arise from all kind of polymers [2]. The separation mechanism of the membranes depends on their structure. According to their morphology or structure, the synthetic membranes can be classified as symmetric or isotropic and asymmetric or anisotropic. The classification of the membranes according to their structure is given in Fig. 2.2.

### 2.1.1 Isotropic Membranes

Microporous, non-porous or dense, and electrically charged membranes are categorized under isotropic membranes.

#### 2.1.1.1 Microporous Membranes

Microporous membranes resemble to the conventional filter in their structure and function. They possess highly voided structures along with interconnected and randomly distributed pores. The separation of the particles takes place by sieving effect mechanism where the particles bigger than the membrane pores are rejected while the smaller particles pass through the membrane pores [1]. This type of the membranes is used for microfiltration and ultrafiltration membrane processes which find the application in breweries, pharmaceutical industry, and waste water treatment from chemical industries etc. [2].

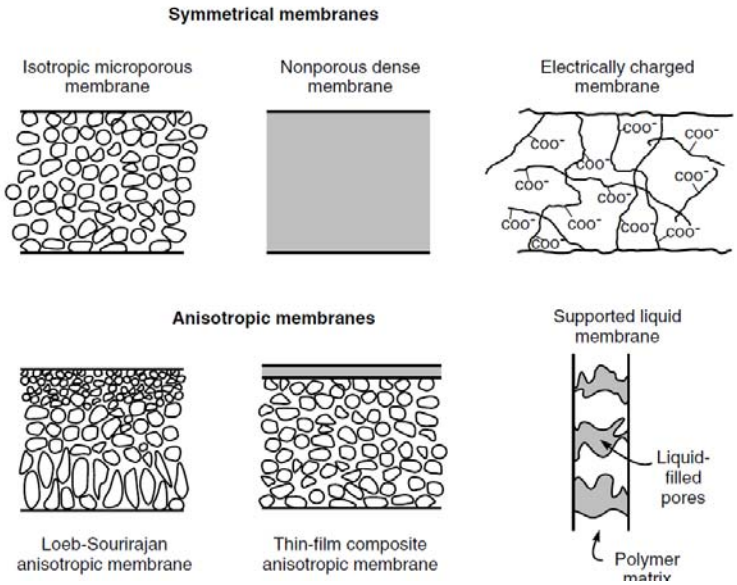


Figure 2.2: Schematic sketch of main types of the membranes. (Reproduced from [1]).

#### 2.1.1.2 Dense Membranes

The dense membranes are comprised of nonporous films through which the transportation of permeants (gases or liquids) takes place under the driving force

of pressure, concentration, or electrical potential gradient. The transport rate of separating species through the non-porous membranes is determined by their diffusion and solubility in the membrane material. The processes like gas separation, pervaporation, and reverse osmosis are carried out using dense membranes. The permeation of the separating mixtures is usually very slow through dense films, so in commercial applications the dense membranes are usually used in the form composite anisotropic membranes for the enhancement of the flux [3].

#### 2.1.1.3 Electrically Charged Membranes

Electrically charged membranes can be dense or microporous. Usually they possess a fine microporous structure where the pore walls contain electrically positive or negative charges. The membranes fixed with positively charged ions bind negatively charged ions (anion) and hence known as anion exchange membranes and the membranes fixed with negatively charged ions bind positively charged ions (cations) and termed as cation exchange membranes. These membranes are applied for the processing of electrolyte solutions through the electrodialysis [1].

### 2.1.2 Anisotropic Membranes

The flux of permeant species through the membranes is inversely proportional to their thickness. For economic reasons higher transport rate of the permeant species is desirable. For this reason the membranes should be as thin as possible. Loeb and Sourirajan prepared the first anisotropic membrane with a dense layer supported by a porous asymmetric structure via the so-called “phase inversion” method for water desalination. The anisotropic membrane with a thin dense selective layer ensures the high flux of the permeants which is economic because of low energy consumption. The composite membranes also come under the category of anisotrpic membranes where a thin dense selective layer is cast on a porous membrane support [3]. Presently the composite membranes are

being used commercially for membrane processes like gas separation, reverse osmosis, nanofiltration and pervaporation.

### 2.1.3 Liquid Membranes

The liquid membranes can be purely liquid or they can be in the form of liquid immobilized within the pores of porous membranes. The liquid can be a suitable organic solvent and may contain some carrier molecules. The carrier molecules enhance the transport of those molecular species having affinity with carrier molecules. These membranes are used only in some specific applications owing to their low selectivity [1, 2].

### 2.1.4 Membrane Separation Processes

The most common membrane separation processes include microfiltration, ultrafiltration, dialysis, nanofiltration, pervaporation, gas separation and reverse osmosis. Microfiltration is widely used in food industry for the clarification of fruit juice, wine, and beer, waste water treatment and separation of oil and water emulsions. Ultrafiltraion processes are used in pharmaceutical industry for the processing of enzymes, antibiotics and pyrogens, in diaries for cheese making and processing of milk proteins, and in water treatment. Nanofiltration is used in separation of bivalent ions, in rejection of micro pollutants like pesticides, herbicides etc. and in textile industries for the retention of dyes. Reverse osmosis is applied in desalination of sea and brackish water, concentration of fruit juices and sugars in food industry, and concentration of milk in diary industries. Pervaporation is mainly used for the dehydration of organic solvents, removal of organic components from water and separation of saturated and unsaturated compounds (e.g. cyclohexane and benzene mixture). Important gas separation processes include hydrogen recovery, organic vapours from the air, nitrogen generation and oxygen enrichment etc. [1-3].

### 2.1.5 Fabrication of the Membranes

The membranes can be fabricated from all kinds of polymers by applying different techniques. The membrane material is the deciding factor for the employment of fabrication techniques, membrane morphology and applied separation principle. The dense membranes can be prepared by simple evaporation of the polymer solutions. However, for commercial application the thin dense layered composite membrane is obtained by the coating of polymer solution on microporous membrane support and subsequent solvent evaporation. The porous membranes can be prepared by stretching, sintering, track etching and phase inversion processes. The phase inversion is used for most of the commercially available membranes and it will be discussed in detail.

#### 2.1.5.1 Phase Inversion

The phase inversion process for the membrane preparation can be divided into three different categories i.e. thermally induced, dry, and wet phase inversion. In thermally induced phase inversion process a low molecular weight component in polymer solution acts as a solvent at high temperature and non solvent at low temperature. As temperature is decreased the phase separation is induced leading to the porous structure and finally the solvent is removed by extraction or evaporation. In the dry phase inversion method, the polymer solution is exposed to the vapours of non solvent leading to the porous membrane structure.

The most commercialised method for the production of the membranes is wet phase inversion method. In wet phase inversion, the polymer solution is cast on a substrate like glass or non woven and then it is immersed in a non solvent bath for phase separation. The solvent rich part of the solution gives rise to pores and the polymer rich part acts as a matrix for porous structure. The phase separation takes place mainly by liquid-liquid demixing for this scenario. In the case of semicrystalline polymers solid-liquid demixing may also play an additional role in

the membrane formation mechanism. The mechanism of membrane formation during phase separation is shown in Fig. 2.3.

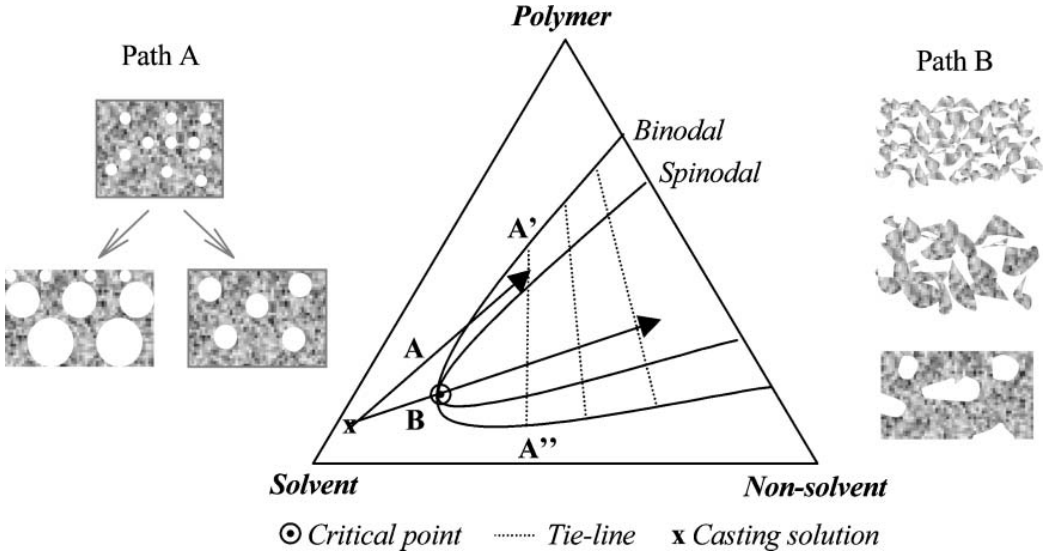


Figure 2.3: Membrane formation mechanism by phase inversion (reproduced from [4]).

In this ternary diagram, the corners of the triangle represent the pure components i.e. polymer, solvent, and non-solvent. The axes of the triangle represent the binary composition, and any point within the triangle represents the mixture of three components. The ternary phase diagram consists of a homogeneous region and liquid-liquid demixing gap region represented by the binodal. In the homogeneous region all the three components are miscible. As the concentration of non-solvent increases, the liquid-liquid demixing gap develops. The unstable region is characterized by the spinodal curve. The region between binodal and spinodal curves represents the metastable state of the system. If the exchange of solvent and non-solvent takes place through metastable region (path A), the nucleation and growth mechanism (NG) is favoured. NG leads to the closed porous structure at the initial stage but NG at the later stages may lead to pores touching each other resulting interconnected pores. In this way, a polymer poor phase leads to pores which are dispersed in polymer matrix. If demixing takes place through the critical point (path B) and goes directly into the unstable region, then spinodal decomposition (SD) predominates. The initially homogeneous solution develops a sinusoidal

concentration fluctuation with increasing amplitude and leads to a separation into two co-continuous phases. Also, in this case the polymer poor phase leads to porous structure. SD favours the formation of interconnected pores in the beginning [3].

Asymmetric structure is usually observed during the phase inversion mechanism resulting in the formation of finger like structures i.e., macrovoids, because of the non-solvent entry into the polymer solution. The macrovoidic structure may lead to less mechanical stability of the membranes used at high transmembrane pressures. The formation of macrovoids can be suppressed by increasing the polymer concentration of the casting solution, increasing the viscosity of the polymer solution using fillers or crosslinking agents, and adding solvent to the non-solvent bath [3].

### 2.1.6 Ultrafiltration Membranes

The structure of ultrafiltration membranes is mainly asymmetric where a thin top layer is supported by a porous sublayer. Ultrafiltration membranes contain the surface pore size ranging from 2 to 100 nm. The resistance to mass transfer is mainly determined by the top layer [2]. For this reason the characterization of the ultrafiltration mainly involves the characterization of its top layer i.e., its thickness, pore size and their distribution, surface porosity, and polarity. The solvent flux of ultrafiltration membranes is determined under pressure as the driving force. The SI unit of mass flux is $Kg.m^{-2}.s^{-1}$. During this study, the water flux was measured in $l.m^{-2}.h^{-1}$ at a defined transmembrane pressure (bar) as expressed by the eq. 2.1:

$$J = \frac{V}{A \cdot t} \qquad 2.1$$

where 'J' represents the flux of the membrane measured as $lm^{-2}\ h^{-1}$, 'V' the permeate volume measured in liter (l), 'A' the membrane active surface area ($m^2$)

and ‘t’ the time required to obtain the required volume across the membrane (h). The permeance of the ultrafiltration membrane can be calculated by introducing the transmembrane pressure factor in flux (eq. 2.2).

$$L = \frac{V}{A \cdot t \cdot \Delta p} \qquad 2.2$$

where ‘$\Delta$p’ is the transmembrane pressure. The permeance was measured in this study as $l.m^{-2}.h^{-1}.bar^{-1}$. The membrane separation performance is characterized by rejection measurements. The concept of cut-off is used by many manufacturers for ultrafiltration membrane separation performance. The cut-off can be defined as the molecular weight of the solutes which is rejected over 90 % by the membrane. The cut-off value for ultrafiltration membranes is strongly dependent of the shape of the solute molecule to be retained. The retention measurements performed using linear dextrans, polyglycols or poly(vinyl pyrrolidone) is much lower compared to globular proteins for the same membrane. It is believed that linear molecules pass through the membrane pore and globular proteins due to their characteristic shape are retained by the membrane [1].

Porous composite membranes may experience a reduction in flux under the effect of high pressure. The majority of composite membranes can undergo compaction during the filtration process. This reduces the pore sizes or free volume inside the membrane and thus reduces the permeability coefficient, which leads to a reduction of permeate flux [3]. Compaction studies can be conducted to observe the response of the porous structure of the membranes at increased pressures and its impact on water flux during the filtration. The flux of a component ‘I’, ‘$J_i$’, across a membrane often is a linear function of the transmembrane pressure (pressure drop) $\Delta$p.

$$J_i = L_i \cdot \Delta p \qquad 2.3$$

'$L_i$' denotes the permeability coefficient of component 'I' (permeance). Machado et al. reported the dropping behavior of flux with the increase in transmembrane pressure for nanofiltration membranes [5], which can be expressed by equation 2.4:

$$J_i = L_i^{\circ} \cdot e^{-\alpha \cdot \Delta p} \cdot \Delta p \qquad 2.4$$

where '$L_i^{\circ}$' is the permeance under atmospheric pressure, and '$\alpha$' is the compaction factor, respectively. By comparing eq. 2.3 and 2.4, the transmembrane pressure dependence of the permeability coefficient is obtained:

$$L_i = L_i^{\circ} \cdot e^{-\alpha \cdot \Delta p} \qquad 2.5$$

where '$\alpha$', the membrane compaction factor ($bar^{-1}$), can be calculated by plotting permeance against the applied pressure, where the slope of the line gives '$\alpha$' value.

A variety of polymers can be used for the fabrication of ultrafiltration membrane e.g., poly(vinylidene fluoride) (PVDF), polyacrylonitrile (PAN), polysulfone (PSf), poly(ether sulfone) (PES) and poly(ether imide) (PEI) and cellulose acetate (CA). In this study, PVDF and PAN have been used for the fabrication of ultrafiltration membranes via the phase inversion method. PVDF is a hydrophobic and semicrystalline polymer with $T_g$ ~ - 40°C. It is resistant to organic and inorganic acids, and it can be used for a wide pH range. *N,N*-dimethylacetamide (DMAc), *N,N*-dimethylformamide (DMF), and dimethyl sulfoxide (DMSO) etc. are most common solvents for PVDF. PAN is highly crystalline and relatively hydrophilic polymer and it is copolymerized with more hydrophilic monomers to improve its processability and to reduce its brittleness. It is an interesting material for ultrafiltration membrane preparation because of its resistance against oxidation

and hydrolysis. DMF, DMAc, and N-methyl pyrrolidone (NMP) has been used for the membrane preparation via phase inversion process [3].

### 2.1.7 Gas Transport through the Membranes

The porous and dense membranes can be used as barriers for selective gas separation. Transport of gases through porous and dense membranes can be explained by pore flow and solution-diffusion models.

#### 2.1.7.1 Pore Flow Model

According to the pore flow model, the permeants are transported by pressure driven flow through the membrane pores. In order to describe this model, three membranes with different pore size are shown in Fig. 2.4. If the pore size lies in the range 0.1-10 μm, the gas molecules permeate through the membrane via convective flow and no separation occurs. A pore size smaller than 0.1 μm, is equal or smaller than the mean free path of the gas molecules. The diffusion in these membranes takes place via Knudsen diffusion where the transport rate of any gas is inversely proportional to the square root of its molecular weight. However, the separation factor is small for the case of Knudsen diffusion. For the membranes with small pores, of the order of 5-20 Å, the separation takes place via molecular sieving. If the membrane has pore sizes ranging between the smaller and larger gas molecules, then small molecules can pass through the pores easily resulting in enhanced separation factor [1].

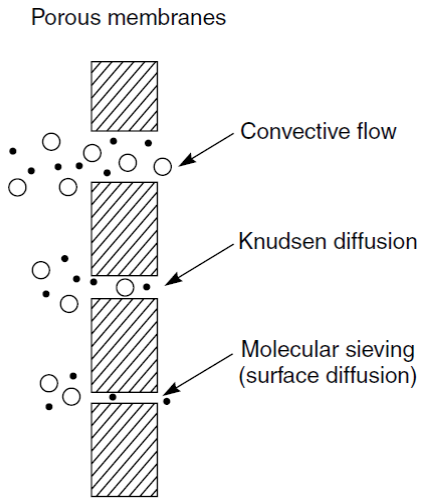


Figure 2.4: Schematic representation of pore flow model [1].

#### 2.1.7.2 Solution Diffusion Model

The transport of gases in non-porous or dense membranes takes place via the solution diffusion mechanism. According to solution diffusion mechanism, the permeation of gas molecules across the membrane can be described by two distinguishing parameters i.e., diffusivity (D) and solubility (S). The permeant molecules dissolve in the membrane material and then diffuse through the membrane at downstream via concentration gradient (Fig. 2.5). The transport of molecules in solution diffusion model takes place in three steps: (a) The molecules are adsorbed or absorbed at the membrane surface on the upstream side (feed side), (b) activated diffusion (solubility) of the molecules through the membrane material and (c) desorption or evaporation on the downstream side (permeate side). The separation of the permeant molecules depends on the solubility and diffusivity coefficients.

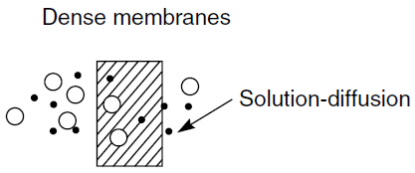


Figure 2.5: Schematic representation of solution diffusion model [1].

$$P = S \cdot D \qquad 2.6$$

where ‘P’ is the permeability coefficient and it is the product of solubility (S) and diffusivity (D) coefficients.

### 2.1.8 Common Definitions of Membrane Performance

The performance of the gas separation membranes is described by two characteristic parameters i.e., permeability and selectivity. The permeability describes the transport of gas molecules through the unit surface area and thickness of the membrane per unit time and pressure difference across the membrane.

$$\text{Permemability (P)} = \frac{\text{flow rate} \times \text{thickness}}{\text{area} \times \text{pressure difference}} \qquad 2.7$$

The most commonly used unit for the gas permeability is Barrer, after the name of Richard Barrer. Barrer is a non SI unit where 1 Barrer = $10^{-10}$ $cm^3 \cdot cm/cm^2 \cdot s \cdot cm$ Hg. 1 Barrer expressed in terms of SI units corresponds to $7.5005 \times 10^{-18}$ $m^2 \cdot s^{-1} \cdot Pa^{-1}$. The flux of the composite membranes, where the thickness of the selective layer is unknown, is described by permeance in literature where it was measured in $m^3/m^2 \cdot h \cdot bar$. The selectivity of a gas separation membrane is described by a separation factor ‘α’ which is the ratio of permeability of two different gases ‘a’ and ‘b’.

$$\alpha_{a/b} = \frac{P_a}{P_b} \qquad 2.8$$

The selectivity ‘α’ is chosen in such a way that it is greater than unity. If the permeability of gas ‘a’ is greater than gas ‘b’ the separation factor is represented as ‘$\alpha_{a/b}$’; if gas ‘b’ has a higher permeability than ‘a’, then the separation factor is represented as ‘$\alpha_{b/a}$’. Therefore the separation factor is never smaller than one. If

$\alpha_{a/b} = \alpha_{b/a} = 1$, then no separation is achieved. The gas diffusion through the non-porous membranes can be described by Fick's law (eq. 2.9):

$$J = -D\frac{dc}{dx} \qquad 2.9$$

where '$J_i$' is the gas flow across the membrane, 'D' is the diffusion coefficient, and dc/dx is concentration gradient across the membrane where it acts as the driving force. The minus sign indicates that the direction of diffusion is downward the concentration gradient. Under steady state conditions eq. 2.9 can be integrated to give the following expression:

$$J_i = \frac{D_i\left(c_{u,i} - c_{d,i}\right)}{l} \qquad 2.10$$

where '$c_{u,i}$' and '$c_{d,i}$' are the concentration of gas component 'i' in the membrane on the upstream and downstream side, respectively, and 'l' is the thickness of the membrane.

According to Henry's law, the concentration of gas molecules inside a polymer is proportional to the applied pressure.

$$c_i = S_i.p_i \qquad 2.11$$

where '$S_i$' ($cm^3$(STP)/$cm^3$.bar) is the solubility coefficient of the component 'i' in the membrane. For the solubility behaviour, Henry's law is mainly applicable to amorphous eleastomeric polymers. Eq. 2.11 can be expressed as follows:

$$J_i = S_i D\frac{\left(p_{u,i} - p_{d,i}\right)}{l} \qquad 2.12$$

$$J_i = S_i D\frac{\Delta p}{l} \qquad 2.13$$

The product of solubility ($S_i$) and diffusivity ($D_i$) coefficient gives the permeability coefficient ($P_i$) of a gas component i.

$$J_i = \frac{P_i}{l}.\Delta p \qquad 2.14$$

From eq. 2.14, it is evident that the flow of a gas is directly proportional to the pressure difference and inversely proportional to the thickness of the membrane.

### 2.1.9 Gas Sorption in Polymer Membranes

The sorption isotherm is linear for the system where the solubility does not depend on the concentration i.e., it obeys Henry's law (Fig. 2.6). For rubbery polymers, the gas solubility follows the Henry's law i.e. the concentration of a gas is directly proportional to the driving force (pressure) and results in a linear sorption isotherm.

$$c_D = K_D.p \qquad 2.15$$

However, glassy polymers are typically assumed to be in a non-equilibrium state which is related with the presence of non-equilibrium excess free volume between the chain segments. Therefore, the gas sorption isotherm for a glassy polymer exhibits non-linear pressure dependence and follows the dual sorption mode which is the combination of Henry's law sorption and Langmuir sorption (Fig. 2.6).

$$c = c_D + c_H \qquad 2.16$$

where 'c' is the total concentration of a gas, '$c_D$' is the gas concentration based on Henry's law sorption and '$c_H$' is the gas concentration based on Langmuir sorption. In Langmuir sorption the gas molecules are filled in the free cavities or

voids created by non equilibrium free volume of glassy polymers. The gas concentration by Langmuir sorption can be expressed by eq. 2.17.

$$c_H = \frac{c'_H bp}{1+bp} \qquad 2.17$$

where 'b' is the hole affinity ($bar^{-1}$) and '$c'_H$' is the saturation constant $cm^3(STP).cm^{-3}$. The dual sorption for glassy polymers can be expressed by combining eq. 2.15 and eq. 2.17.

$$c = K_D.p + \frac{c'_H bp}{1+bp} \qquad 2.18$$

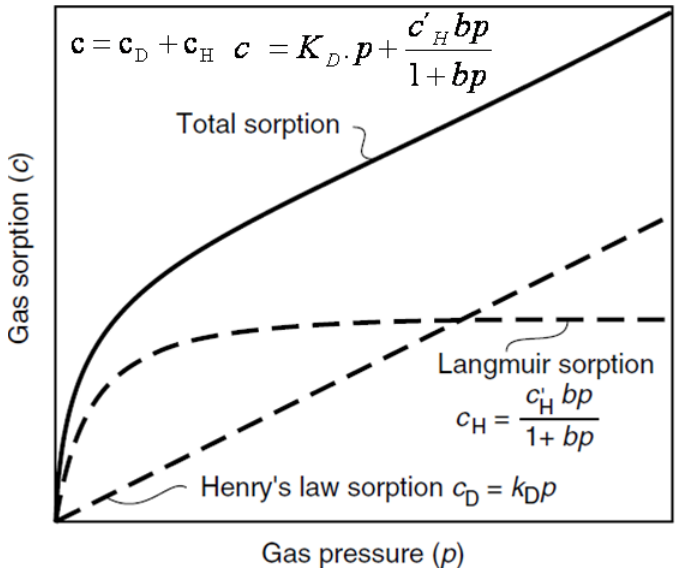


Figure 2.6: Gas sorption isotherms by Henry's law, Langmuir sorption and dual sorption (derived from [1]).

### 2.1.10 Gas Separating Membranes

The history of gas separation dates back to 1829 when Thomas Graham measured the permeation rates of different gases through available diaphragms. Graham's work on porous membranes led to Graham's law of diffusion. In 1940s Graham's law of diffusion was exploited for the separation of $U^{235}F_6$ from $U^{238}F_6$. From 1940s to 1950s, the basis of modern theories of gas permeation was laid.

The solution-diffusion model developed in this era is still an accepted model for gas permeation through non-porous membranes. The development of asymmetric membranes having high flux laid the basis for modern gas separation technology in late 1960s and early 1970s. Monsanto was the first company who commercialized the hydrogen separating Prism® membrane from ammonia-plant purge gas streams in 1980 [1]. Monsanto's successful achievement encouraged other companies to promote their own technology for gas separation. Currently, various companies in the market are using membrane based gas separation for many applications [3]. The salient applications include the $O_2/N_2$ separation for $N_2$ and $O_2$ enrichment, $H_2$/hydrocarbons for refinery hydrogen recovery, hydrocarbon from process stream for organic solvent recovery and hydrocarbon / air for pollution control and hydrocarbon recovery. In Table 2.1, gas permeability data of different gases through different polymeric membranes is presented.

Table 2.1: Gas permeability data of different polymers [3]

| Polymer | Permeability at 30°C (Barrer*) | | | | |
|---|---|---|---|---|---|
| | $H_2$ | $N_2$ | $O_2$ | $CH_4$ | $CO_2$ |
| Cellulose acetate | 2.63 | 0.21 | 0.59 | 0.21 | 6.3 |
| Ethyl cellulose | 87 | 8.4 | 26.5 | 19 | 26.5 |
| Polycarbonate, brominated | - | 0.18 | 1.36 | 0.13 | 4.23 |
| Poly(dimethylsiloxane) | 550 | 250 | 500 | 800 | 2700 |
| Polyimide (Matrimid) | 28.1 | 0.32 | 2.13 | 0.25 | 10.7 |
| Polymethylpentene | 125 | 6.7 | 27 | 14.9 | 84.6 |
| Polyphenyleneoxide | 113 | 3.81 | 16.8 | 11 | 75.8 |
| Polysulfone | 14 | 0.25 | 1.4 | 0.25 | 5.6 |

* 1 Barrer = $10^{-10}$ $cm^3$.cm/$cm^2$.s.cmHg

## 2.2 Carbon Nanotubes

Carbon nanotubes (CNTs) were re-discovered and characterized in 1991 by Iijima and this was made possible by the use of state of the art transmission electron microscopy [6]. CNTs are cylinder-shaped tubes, with their diameter as small as a few nanometers and their length varying from a few microns to centimeters, hence making them the high aspect ratio nanoparticles [7-9]. These cylindrical shaped tubes are comprised of rolled graphene sheets and can be

classified according to the number of graphene layers. A roll up of single graphene layer leads to single-walled carbon nanotubes (SWCNTs) and several concentric layers to multi-walled carbon nanotubes (MWCNTs) [10]. The first identified CNTs were comprised of 2 to 50 concentric cylindrical like shells. These shells were regularly spaced by a distance of 0.34 nm as in conventional graphite materials [6]. SWCNTs were synthesized in 1993 after the identification of MWCNTs [11].

### 2.2.1 Structure of Carbon Nanotubes

The structure of CNTs strongly depends on the rolling pattern of graphene sheet. The rolling of graphene layer can be described by a chiral vector $C_h$ which connects two crystallographically equivalent sites (A and A´ in Fig. 2.7) on the sheet [12].

The chiral vector $C_h$ can be defined as:

$$C_h = na_1 + ma_2 \qquad 2.19$$

where '$a_1$' and '$a_2$' are unit vectors of the hexagonal honey comb lattice and 'n' and 'm' are the integers denoting the relative position of the pair of atoms on the graphene sheet.

The chiral vector '$C_h$' defines the circumference of the tube and the diameter of the nanotube ($d_t$) can be estimated by eq. 2.20:

$$d_t = \frac{a}{\pi}\sqrt{n^2 + nm + m^2} \qquad 2.20$$

where '$a$' is the lattice constant of the honeycomb network

$$a = \sqrt{3} \times a_{cc} \qquad 2.21$$

where '$a_{cc}$' ~ 0.142 nm, the C-C bond length.

The chiral vector '$C_h$' defines a particular (n,m) tube, as well as its chiral angle '$\theta$' which is the angle between '$C_h$' and '$a_1$' The chiral angle can be calculated using eq. 2.22:

$$\cos\theta = \frac{2n+m}{2\sqrt{n^2+nm+m^2}} \qquad 2.22$$

Because of the hexagonal symmetry of the graphene lattice, '$\theta$' value lies in the range $0 \le |\theta| \le 30^\circ$. The chiral angle '$\theta$' represents the tilt angle of the hexagons with respect to the direction of CNTs axis. CNTs of the type (n,0) ($\theta$=0°) are classified as zigzag tubes, because they exhibit a zigzag pattern along the circumference. C-C bonds in these tubes exist parallel to the tube axis. CNTs of type (n,m=n) ($\theta$=30°) are categorized as armchair tubes, because they exhibit an armchair pattern along the circumference. These tubes display C-C bonds perpendicular to the tube axis. Both zigzag and armchair CNTs are grouped together under achiral tubes in contrast with general chiral tubes (n,m≠n≠0) (Fig. 2.8). For DWCNTs and MWCNTs, the control of chirality along the graphene layers is complicated. Hence, it is difficult to classify them according to their chirality [12].

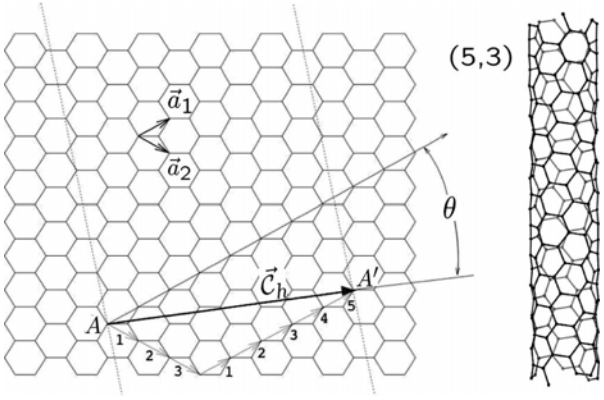


Figure 2.7 : Graphene sheet with lattice vectors '$a_1$' and '$a_2$' The chiral vector $C_h = 3a_1 + 5a_2$ represents a possible wrapping of the two dimensional graphene sheet into a tubular form. The resulting (5,3) nanotube is shown on the right side having chiral character. (Reproduced from [12]).

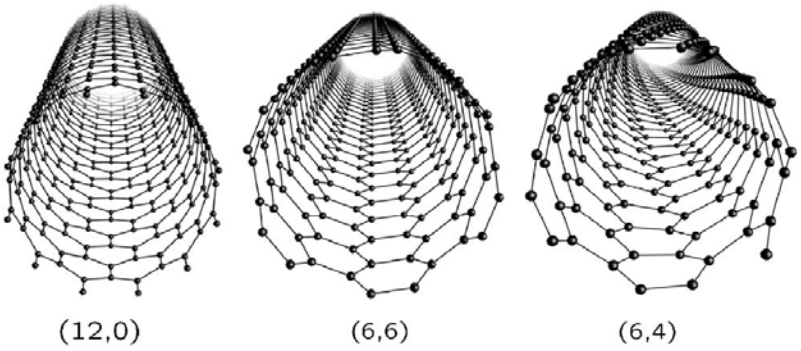


Figure 2.8 : Atomic structures of (12,0) zigzag, (6,6) armchair and (6,4) chiral nanotubes. (Reproduced from [12]).

### 2.2.2 Synthesis of Carbon Nanotubes

CNTs are produced by three main techniques: arc discharge, laser ablation and chemical vapor deposition.

#### 2.2.2.1 Arc Discharge Method

Iijima used the arc discharge method to synthesize MWCNTs in 1991 [6]. This method involves the evaporation of carbon atoms from the anode when DC arc plasma is generated between graphite anode and cathode under an inert atmosphere. The anode is consumed by the evaporation of carbon atoms and filamentous deposit containing carbon nanotubes and other byproducts are collected on the cathode (Fig. 2.9 (a)). MWCNTs produced by arc discharge method are very straight which is indicative of their high crystallinity. There exist a few defects such as pentagons or heptagons on the side walls of arc produced nanotubes [13]. Byproducts of this process are multilayered graphitic particles with polyhedron shapes. For the growth of single-walled carbon nanotubes, a metal catalyst is needed in arc-discharge system and the first success was achieved by Bethune et al. in 1993. They used carbon anode with small percentage of cobalt catalyst in the discharge experiment and found abundance of SWCNTs in the soot material [11].

#### 2.2.2.2 Laser Ablation Method

Smalley and coworkers used this method for the synthesis of SWCNTs [14]. In this method intense laser pulses are used to ablate a carbon precursor containing 0.5 atomic percent of nickel and cobalt at 1200°C with continuous inert gas flow. The flow of inert gas leads to a collection of CNTs on a cold finger (Fig. 2.9 (b)) [13]. This method is not suitable for mass production; nevertheless CNTs with good quality, controlled diameter, and diameter distribution are possible by this technique. SWCNTs samples prepared by this method have been used extensively for fundamental studies [15].

#### 2.2.2.3 Chemical Vapor Deposition

Walker et al. reported the catalytic chemical vapor deposition of carbon in 1959 [16], however, it was used in 1993 for the production of CNTs [17]. This method is used for the production of CNTs on industrial scale. It involves the decomposition of hydrocarbon gas for a period of time through a tube reactor containing the catalyst material at higher temperatures (Fig. 2.9 (c)). CNTs grown over the catalyst are collected upon the cooling of the system to room temperature. The key parameters and components for CVD growth of CNTs include the types of hydrocarbons, catalysts, and temperature. In most of CVD methods, ethylene or acetylene are used as carbon feedstock. The temperature range for the CVD process is 550-750°C and iron, nickel or cobalt nanoparticles are employed as catalyst systems [13].

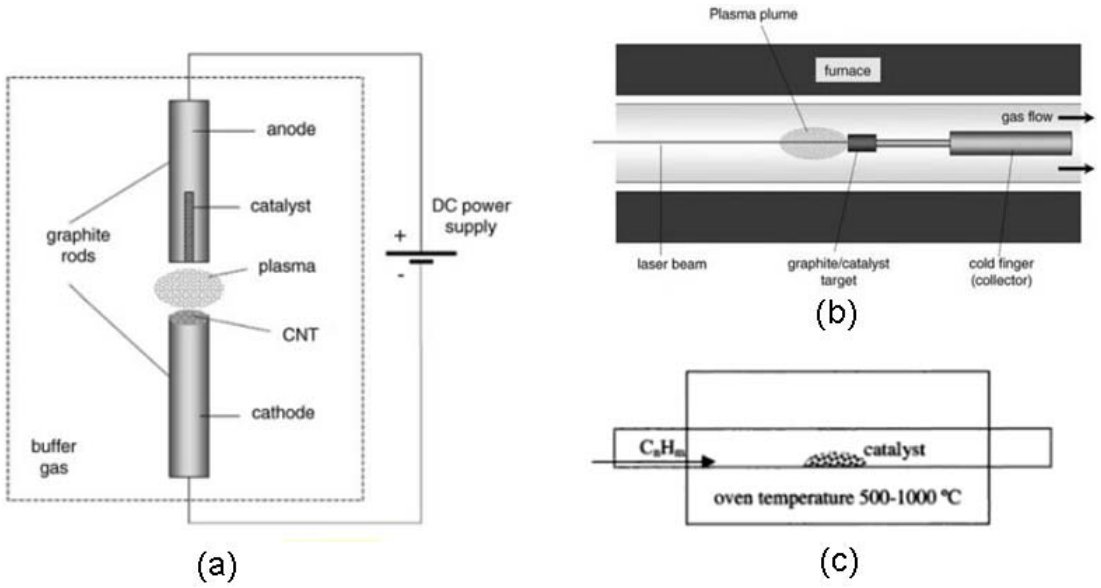


Figure 2.9: Schematic diagram of (a) Arc discharge method, (b) Laser ablation method and (c) CVD reactor, for carbon nanotube growth. (a) and (b) reproduced from [10] and (c) reproduced from [13].

### 2.2.3 Mechanical Properties of Carbon Nanotubes

Like graphite, MWCNTs possess $sp^2$ hybrid bonding among carbon atoms and graphene layers are 0.34 nm spaced [6]. It is known that graphite has in plane modulus of 1.06 TPa and MWCNTs were expected to display the similar stiffness [18]. Computer based simulation studies also forecasted their extraordinary mechanical properties [19]. The first actual mechanical measurements were performed on MWCNTs by Treacy et al. in 1996. They calculated Young's moduli (0.41-4.15 TPa) using the measurement of the amplitude of intrinsic thermal vibrations by transmission electron microscopy (TEM) [20]. Wong et al. conducted the first direct measurement of mechanical properties of arc-grown MWCNTs using atomic force microscopy (AFM) in 1997. They reported Young's modulus of 1.28 TPa and bending strength of 14 GPa [21]. Salvetat et al. measured the average modulus value of 810 GPa for arc-MWCNTs using AFM [22]. They measured a modulus of ~1TPa for small diameter SWCNTs bundles using the same method [23].

The mechanical properties of CNTs strongly depend upon the concentration of defect sites and type [24]. Xie et al. synthesized MWCNTs via CVD method and the values of Young's modulus and tensile strength were found as 0.45 TPa and 3.6 GPa, respectively. The modulus and strength values were much lower compared to arc grown CNTs. The defects in the tubes and the interwall slides of MWCNTs may be responsible for the depression of mechanical properties of the tubes [25]. The magnificent mechanical properties of CNTs make them valuable candidates for their application in composite materials.

### 2.2.4 Electrical Properties of Carbon Nanotubes

A SWCNT possesses metallic or semiconducting behavior depending on their structure i.e., rolling pattern of the graphene sheet which is driven by chiral vector with n and m as integers (Fig. 2.7) [12]. A SWCNT (n,m) is metal like, if n=m i.e., armchair SWCNT. A nanotube with n-m=3*l*, where *l* is an integer, behaves like a semi metal [26]. With n-m≠3*l*, resulting SWCNT is a semiconductor. The average abundance of metallic SWCNTs is one third of total, and the rest of SWCNTs are semiconductors [27]. MWCNTs have also been reported to have quite good electrical conductivity. Ebbesen et al. measured the conductivities of individual MWCNTs that ranged between 20 and $2\times10^7$ S/m. They reported that MWCNTs can carry current densities of values as high as $6\times10^6$ A·cm$^{-2}$ without damaging the sample [28]. Electrical conductivity of CNTs is greatly influenced with the introduction of defects created during production and by functionalization on their surface. The extraordinary electrical properties of CNTs make them interesting fillers to introduce electrical conductivity in synthetic plastics which are mostly insulators.

### 2.2.5 Functionalization of Carbon Nanotubes

Carbon nanotubes are produced in the form of bundles where the individual CNTs are stacked together in the form of aggregates via van-der-Waals and

$\pi-\pi$ stacking interactions. Modification of their surface chemistry is an important tool for better dispersion in solvents and polymer matrices. Surface functionalization involves the introduction of various functional groups or reacting sites on side walls of CNTs [29]. Surface functionalization of CNTs can be divided into two main categories; covalent and non-covalent functionalization.

#### 2.2.5.1 Covalent Functionalization

Covalent functionalization creates defects on the side walls of CNTs to incorporate various functional groups. It changes the hybridization of carbon atoms on the walls of CNTs from $sp^2$ to $sp^3$, resulting in loss of conjugation [30]. Covalent functionalization of CNTs has been reported by oxidation [31, 32], halogenation [33, 34], radical addition [35], electrophilic or neucleophilic addition [36, 37] etc. The attached functional groups can be small functional groups like –COOH, –OH, –F, $–NH_2$ etc. depending upon the followed functionalization pathway. These primary functional groups can be used for the attachment of various chemical species and polymers on the surface of CNTs. Covalent binding of the polymer functionalities on CNTs takes place via “grafting from” or “grafting onto” approaches [38].

##### 2.2.5.1.1 “Grafting From”

“Grafting from” means that polymerization of monomers from the active functional groups present on side walls of carbon nanotubes [31, 32]. This approach can be carried out by employing different polymerization mechanisms i.e., free radical polymerization, anionic polymerization, reversible addition-fragment chain transfer (RAFT) polymerization, and atom transfer radical polymerization (ATRP) etc. ATRP is the most commonly used technique for this approach. Yao et al. incorporated phenol end groups on SWCNTs using an 1,3 dipolar cycloaddition reaction [39]. The phenol groups were further derivatized with 2-bromoisobutyryl bromide resulting in an ATRP initiator on the nanotube side walls. Finally, methyl methacrylate (MMA) and *tert*-butyl acrylate (*t*BA) were grafted from the initiator

modified SWCNTs via ATRP. Yan et al. modified MWCNTs with carboxyl groups using nitric acid and carboxyl groups were further activated with thionyl chloride to create carbonyl chloride end groups [32]. Carbonyl chloride end groups were modified by ethylene glycol to introduce –OH end groups. –OH functionalized MWCNTs were then reacted with 2-bromoisobutyryl bromide to bind ATRP initiator on the side walls of MWCNTs. Finally, the ATRP technique was used to graft PMMA from the initiating sites present on the MWCNTs. The polymer thickness was controlled by varying the weight ratio between monomer and initiator modified MWCNTs. Polymer modified nanotubes showed good solubility in non polar solvents and weakly polar solvents like chloroform and tetrahydrofuran (THF) etc.

The above mentioned examples describe multiple reaction steps for modification of CNTs with polymer. The production of polymer functionalized CNTs via grafting from technique can be performed on hydroxyl and amine functionalized CNTs produced industrially by special thermal oxidation methods. The immobilization of ATRP initiator on CNTs follows the grafting of polymers from the initiator moieties. In this work polystyrene and poly(methyl methacrylate) were grafted from industrially supplied prefunctionalized MWCNTs i.e MWCNTs containing amine functional groups by applying ATRP.

#### 2.2.5.1.2 “Grafting Onto”

In the “grafting onto” approach, the polymers with reactive end functional groups are attached with functional groups present on the CNTs. Polymer chains can be attached to the carboxyl functionalized MWCNTs by amidation and esterification reactions [40, 41]. Lin et al. grafted poly(vinyl alcohol) (PVA) onto carboxyl functionalized CNTs by carbodiimide-activated esterification reactions. PVA functionalized CNTs showed stable dispersion in water, dimethyl sulfoxide (DMSO), and PVA matrix [42]. Sano et al. performed $SOCl_2$ reaction with carboxyl functionalized SWCNTs to create carbonyl chloride end functional

groups. They grafted amino terminated polyethylene oxide onto carbonyl chloride functional groups via amidation reaction. The modified SWCNTs showed better dispersion in water and *N, N*-dimethylformamide (DMF) [40]. Lou et al. reported the grafting of polystyrene (PS), poly(ε-caprolactone) (PCL), and their block copolymers, end capped with (2,2,6,6-Tetramethylpiperidin-1-yl)oxyl (TEMPO), onto MWCNTs by the radical addition mechanism [43]. PS and PCL modified MWCNTs showed stable dispersion in toluene and THF. The grafting density of polymer chains is lower for "grafting onto" technique compared to "grafting from" technique.

#### 2.2.5.2 Non-covalent Functionalization

In comparison to covalent functionalization, non-covalent functionalization preserves the $sp^2$ configuration of CNTs and thus conserves their electrical and mechanical properties. Organic mediating molecules, ranging from low molecular weight species to polymers, are used for non-covalent functionalization of CNTs [30]. These mediating molecules change the surface characteristics of CNTs by either adsorption or wrapping the CNTs surface. Amphiphilic molecules like surfactants, copolymers, and polyaromatic compounds etc. adsorb on the surface of CNTs and lead to better dispersibility without any destruction or defects on the surface of CNTs. The most commonly used surfactants for dispersing CNTs in aqueous media include sodium dodecyl sulfate (SDS) [44], sodium dodecyl benzene sulfonate (SDBS) [44], Brij, Tween [45, 46], and Triton X 100 [44] etc. The individual dispersion of CNTs is made possible by their encapsulation inside the micelles having hydrophobic interiors [47]. Islam et al. found that SDBS is more powerful surfactant to disperse SWCNTs compared to SDS at 20 mg/mL in aqueous media. In addition to surfactant interactions, SDBS possess aromatic ring $\pi$–$\pi$ interaction with the graphitic walls of SWCNTs [44].

Polyaromatic compounds also possess $\pi$–$\pi$ interactions with CNTs. Tomonari et al. found that ammonium salts based on pyrene moieties led to better and stable

dispersions of SWCNTs in aqueous solution compared to phenyl and naphtyl based ammonium salts [48]. The strong adsorption capability of the pyrene moiety on the surface of CNTs provides the opportunity to attach their derivatives containing different functionalities on CNTs. Chen et al. attached proteins on SWCNTs surfaces using 1-pyrenebutanoic acid, succinimidyl ester [49]. Ji et al. reported surfactants based on polysiloxane derivatives of pyrene and porphyrin [50]. The surfactant containing the pyrene moiety led to dispersed SWCNTs and MWCNTs in non polar solvent like petroleum ether. However, they found that the surfactant with porphyrin moiety gave rise to a better dispersion of only SWCNTs. Liu et al. functionalized MWCNTs in water using poly(ethylene glycol) (PEG) derivative of pyrene [51]. They proved the adsorption of pyrene-PEG on MWCNTs by analyzing the dispersion of MWCNTs, obtained after different cycles of dialysis, by UV-Vis spectroscopy. Adsorption of pyrene-PEG was also confirmed by thermogravimetric analysis (TGA). Various research groups have attached pyrene with different polymers and subsequently functionalized CNTs using pyrene modified polymers by non covalent functionalization [52].

Polymer wrapping on CNTs surface also improves their dispersion in organic and aqueous medium. Conjugated polymers like poly(m-phenylene vinylene) (PmPV) [53] or poly(3-hexylthiophene) (P3HT) [54] interact with CNTs via strong $\pi-\pi$ interactions which drives the wrapping of polymers around CNTs. Zou et al. reported the $\pi-\pi$ interaction of a conjugated block copolymer, poly(3-hexylthiophene)-*block*-polystyrene (P3HT-b-PS), with CNTs [55]. The conjugated block interacts with CNTs while the PS block improves the dispersion of CNTs in chloroform. The wrapping of the conjugated polymer weakens the inter-tube van-der-Waals interactions and the PS block improves the dispersion of CNTs. Other polymers like poly(vinyl pyrrolidone) [56], Polystyrene-*block*-poly(acrylic acid) [57] or poly(styrene sulfonate) [56] display week $\pi-\pi$ interaction with CNTs but they can be used to wrap CNTs.

## 2.3 Atom Transfer Radical Polymerization (ATRP)

The polymer chains have been successfully grafted from MWCNTs by controlled radical polymerization (CRP) and ATRP is one of the used CRP. Its principle is based upon creation of a dynamic equilibrium between a large number of dormant species and a small number of propagating radicals. These propagating radicals are produced through a reversible redox process which is catalyzed by a transition metal complex. A broad range of molecular weights and narrow molecular weight distribution are possible through this mechanism [58].

The mechanism of ATRP is described in Fig. 2.10. A transition metal complex $M_t^m(L)_z$ acts as an activator where $M_t^m$ represents the transition metal having oxidation state m and L represents ligand attached to transition metal. The metal catalyst undergoes one electron oxidation with the abstraction of a radically transferable atom or group from the dormant species $P_nX$ and produces an active radical. This active radical adds monomers to carry out propagation.

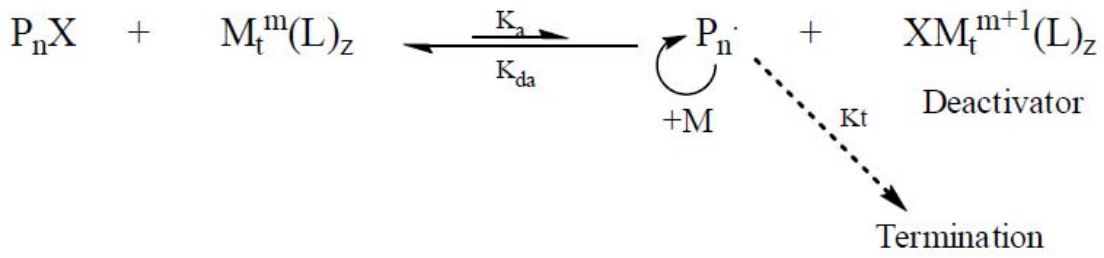


Figure 2.10: Schematic diagram representing the mechanism of ATRP [58].

The halogen atom (X) is transferred and this transfer is reversible as the propagating radical also can abstract a halogen atom from the oxidized metal complex (deactivator) in a reverse reaction leading to generation of dormant species (deactivation). Activation of dormant species takes place with rate constant $K_a$, deactivation takes place with rate constant $K_{da}$ and rate constant for the dynamic equilibrium can be written by eq. 2.23:

$$K_{eq} = \frac{K_a}{K_{da}} \qquad 2.23$$

ATRP can be used for grafting (co)-polymers of vinyl monomers including styrenes, acrylates, methacrylates and acrylonitrile etc from CNTs. For each type of monomers there is a specific set of conditions to conduct ATRP. Alkyl halides (RX) are used as the initiator for ATRP. Use of copper catalyst system in ATRP is advantageous compared to other transition metal catalysts like nickel, rhodium and palladium etc. in terms of cost and effectivity. Nitrogen based ligands e.g. N,N,N',N',N''-Pentamethyldiethylenetriamine (PMDETA) and 2,2'-bipyridine work efficiently for copper catalysed ATRP systems compared to oxygen, or phosphorus based ligands [58].

A typical ATR Polymerization is conducted in bulk or solution. Non polar solvents, e.g. *p*-xylene, *p*-dimethoxy benzene, anisole, diphenyl ether, etc., are used usually but some polar solvents are also used like ethylene carbonate and propylene carbonate to carryout ATRP. The rate of polymerization increases with increasing temperature due to increase of radical propagation rate constant and atom transfer equilibrium constant. However, at higher temperatures the rate of side reactions becomes more pronounced. The solubility of metal catalyst increases with the increase in temperature, however, the decomposition of transition metal catalyst takes place at elevated temperatures as well. The selection of optimal temperature depends on the monomer, the catalyst, and the targeted molecular weight [58].

## 2.4 Mixed Matrix Membranes

### 2.4.1 For Gas Separation

Conventional polymeric membranes for gas separation exhibit a trade off between permeability and selectivity, described by Robeson in 1991 [59] by developing upper bound limit which was later revised in 2008 [60]. For the

improvement in gas separation performance in conventional polymeric membranes, the direction is now focused towards the altering of the chemical structure of the conventional polymers and addition of inorganic porous fillers in the polymers. The addition of nanosized porous inorganic fillers into polymers has given rise to the important class of membranes known as mixed matrix membranes (MMMs). The first MMMs for gas separation were reported in 1955 when Amerongen used carbon black and other light inorganic fillers in butyl rubber where the addition of fillers in butyl rubber decreased the permeability of the gases. In 1991 Jia et al. reported the addition of zeolite filler in silicone rubber in which case the addition of the zeolite fillers led to increase in permeability and selectivity of the resultant composite membranes [61]. In literature, improved gas separation performance has been reported by using MMMs incorporated with zeolites, silica, mesoporous molecular sieves, carbon molecular sieves, and carbon nanotubes (CNTs) [48, 61-63].

CNTs are the potential fillers with their diameter ranging from several Angstroms to tens of nanometers. Molecular simulation studies have revealed that CNTs, having comparable diameter to the pores of zeolite, showed higher diffusivity compared to zeolite [64]. Higher diffusive properties of CNTs compared to zeolite make them the interesting candidate to fabricate MMMs. During the last five years MMMs incorporated with CNTs were extensively studied. Kim et al. reported that open ended SWCNTs mixed into poly(imide siloxane) membranes showed increase in permeability of $O_2$, $N_2$, and $CH_4$. The diffusivity of gas molecules across the nanocomposite membranes increased which was believed to take place through the open ended SWCNTs, however, the solubility of the gas remained unchanged [63]. They also incorporated SWCNTs, functionalized with long chain amines, into polysulfone and concluded that permeability increased with the addition of SWCNTs where the diffusivity of gases through the SWCNTs increased through SWCNTs [65]. The selectivity of gas pairs $He/CH_4$ and $CO_2/CH_4$ decreased but of $CH_4/N_2$ increased compared to neat polysulfone membranes. Fonseca et al. mixed shortened MWCNTs in PEBAX® 1074 and

reported a 40 % increase in permeability of $CO_2$ compared to the neat polymer, however, no significant effect on selectivity of $CO_2$ was found [66]. Sanip et al. prepared the polyimide membranes incorporated with β-cyclodextrin functionalized MWCNTs via phase inversion method [67]. The selectivity of $CO_2$ over $CH_4$ increased 100 % with the addition of functionalized MWCNTs. The increase in permeance of $CO_2$ was also observed which was related to the stronger adsorbing property of $CO_2$ through MWCNTs channels compared to $O_2$ and $N_2$. CNTs containing MMMs is still a developing field and a lot of research is being carried out for the development in this field.

### 2.4.2 Membranes for Water Treatment

Membranes have been extensively used for the removal of various contaminants present in water. Successful attempts were done to incorporate different fillers like titania, silica, alumina, and CNTs in polymeric membranes for improving the separation performance and resistance against fouling and compaction phenomena. Choi et al. blended carboxylated multi-walled carbon nanotubes (MWCNTs) with polysulfone and prepared the membranes by a phase inversion process [68]. The pure water flux increased by increasing MWCNTs content up to 1.5 wt. % and then decreased with further loading of MWCNTs. The higher flux was attributed to a hydrophilic surface and large surface pores, resulting from the addition of MWCNTs. Tang et al. used PEG6000 and MWCNTs for the fabrication of chitosan porous membranes [69]. They observed that membranes with 10 wt. % MWCNTs loading showed 4.6 times higher water flux than pure chitosan membranes. The higher water flux was observed due to the formation of MWCNTs nanochannels in chitosan pores. Moreover, the tensile strength of the membranes increased with MWCNTs addition. Celik et al. incorporated carboxyl functionalized MWCNTs in polyethersulfone membranes prepared by a phase inversion method [70]. Improved separation performance along with low fouling rates were found in MWCNTs embedded membranes compared to neat membranes. Recently, hydroxyl functionalized MWCNTs mixed polyacrylonitrile

(PAN) membranes have been reported with improved resistance against compaction at 2 wt. % loading along with improved separation performance compared to neat PAN membranes [71].

## 2.5 References


[1] R. W. Baker, Membrane Technology and Applications, 2nd edi., Wiley-VCH, 2004.

[2] M. Mulder, Basic Principles of Membrane Technology, 2nd edi., Kluwar Publishers, 1996.

[3] S. P. Nunes, K. V. Peinemann, Membrane Technology in the Chemical Industry, 2nd edi., Wiley-VCH, 2006.

[4] P. Vandezande, L. E. M. Gevers, I. F. J. Vankelecom, Chem. Soc. Rev., 37 (2007) 365-405.

[5] D. R. Machado, D. Hasson, R. Semiat, J. Membr. Sci., 163 (1999) 93-102.

[6] S. Iijima, Nature, 354 (1991) 56-58.

[7] K. Balasubramanian, M. Burghard, Small, 1 (2005) 180-192.

[8] H. W. Zhu, C. L. Xu, D. H. Wu, B. Q. Wei, R. Vajtai, P. M. Ajayan, Science, 296 (2002) 884-886.

[9] X. Wang, Q. Li, J. Xie, Z. Jin, J. Wang, Y. Li, K. Jiang, S. Fan, Nano Lett., 9 (2009) 3137-3141.

[10] S. Reich, C. Thomsen, J. Maultzsch, Carbon Nanotubes: Basic Concepts and Physical Properties, Wiley-Vch 2004.

[11] D. Bethune, C. Klang, M. De Vries, G. Gorman, R. Savoy, J. Vazquez, R. Beyers, Nature, 363 (1993) 605-607.

[12] J. C. Charlier, X. Blase, S. Roche, Rev. of Modern Phy., 79 (2007) 677.

[13] H. Dai, Carbon Nanotubes: Synthesis, Structure, Properties and Applications., Springer, 2001.

[14] A. Thess, R. Lee, P. Nikolaev, H. Dai, P. Petit, J. Robert, C. Xu, Y. H. Lee, S. G. Kim, A. G. Rinzler, D. T. Colbert, G. E. Scuseria, D. Tomanek, J. E. Fischer, R. E. Smalley, Science, 273 (1996) 483-487.

[15] M. H. Rümmeli, P. Ayala, T. Pichler, Carbon Nanotubes and Related Structures, (2010) 1-21.

[16] P. Walker Jr, J. Rakszawski, G. Imperial, J. Phy. Chem., 63 (1959) 133-140.

[17] M. Jose-Yacaman, M. Miki-Yoshida, L. Rendon, J. Santiesteban, App. Phy. Lett., 62 (1993) 202-204.

[18] J. N. Coleman, U. Khan, Y. K. Gun'ko, Adv. Mater., 18 (2006) 689-706.

[19] G. Overney, W. Zhong, D. Tomanek, Molecules and Clusters, 27 (1993) 93-96.

[20] M. Treacy, T. Ebbesen, J. Gibson, Nature, 381 (1996) 678-680.

[21] E. W. Wong, P. E. Sheehan, C. M. Lieber, Science, 277 (1997) 1971-1975.

[22] J. P. Salvetat, A. J. Kulik, J. M. Bonard, G. a. D. Briggs, T. Stöckli, K. Méténier, S. Bonnamy, F. Béguin, N. A. Burnham, L. Forró, Adv. Mater., 11 (1999) 161-165.
[23] J. P. Salvetat, G. a. D. Briggs, J. M. Bonard, R. R. Bacsa, A. J. Kulik, T. Stöckli, N. A. Burnham, L. Forró, Phy. Rev. Lett., 82 (1999) 944-947.
[24] J. P. Salvetat, J. M. Bonard, N. Thomson, A. Kulik, L. Forro, W. Benoit, L. Zuppiroli, App. Phy. Mater. Sci. Processing, 69 (1999) 255-260.
[25] S. Xie, W. Li, Z. Pan, B. Chang, L. Sun, J. Phy. Chem. Solids, 61 (2000) 1153-1158.
[26] H. Dai, A. Javey, E. Pop, D. Mann, Y. Lu, Nano, 1 (2006) 1-13.
[27] H. Kataura, Y. Kumazawa, Y. Maniwa, I. Umezu, S. Suzuki, Y. Ohtsuka, Y. Achiba, Synthetic Metals, 103 (1999) 2555-2558.
[28] T. Ebbesen, H. Lezec, H. Hiura, J. Bennett, H. Ghaemi, T. Thio, Nature, 382 (1996) 54-56.
[29] D. Tasis, N. Tagmatarchis, A. Bianco, M. Prato, Chem. Rev., 106 (2006) 1105-1136.
[30] S. W. Kim, T. Kim, Y. S. Kim, H. S. Choi, H. J. Lim, S. J. Yang, C. R. Park, Carbon, 50 (2012) 3-33.
[31] S. Qin, D. Qin, W. T. Ford, D. E. Resasco, J. E. Herrera, J. Am. Chem. Soc., 126 (2004) 170-176.
[32] H. Kong, C. Gao, D. Yan, J. Am. Chem. Soc., 126 (2004) 412-413.
[33] E. Mickelson, C. Huffman, A. Rinzler, R. Smalley, R. Hauge, J. Margrave, Chem. Phy. Lett., 296 (1998) 188-194.
[34] V. N. Khabashesku, W. E. Billups, J. L. Margrave, Accounts Chem. Res., 35 (2002) 1087-1095.
[35] J. Liu, M. R. I. Zubiri, M. Dossot, B. Vigolo, R. H. Hauge, Y. Fort, J. J. Ehrhardt, E. Mcrae, Chem. Phy. Lett., 430 (2006) 93-96.
[36] M. Holzinger, O. Vostrowsky, A. Hirsch, F. Hennrich, M. Kappes, R. Weiss, F. Jellen, Angew. Chem., 40 (2001) 4002-4005.
[37] N. Tagmatarchis, V. Georgakilas, M. Prato, H. Shinohara, Chem. Commun., (2002) 2010-2011.
[38] P. Liu, Eur. Polym. J., 41 (2005) 2693-2703.
[39] Z. Yao, N. Braidy, G. A. Botton, A. Adronov, J. Am. Chem. Soc., 125 (2003) 16015-16024.
[40] M. Sano, A. Kamino, J. Okamura, S. Shinkai, Langmuir, 17 (2001) 5125-5128.
[41] J. Albuerne, A. Boschetti-de-Fierro, V. Abetz, J. Polym. Sci. Polym. Phy., 48 (2010) 1035-1046.
[42] Y. Lin, B. Zhou, K. a. S. Fernando, P. Liu, L. F. Allard, Y. P. Sun, Macromolecules, 36 (2003) 7199-7204.
[43] X. Lou, C. Detrembleur, V. Sciannamea, C. Pagnoulle, R. Jérôme, Polymer, 45 (2004) 6097-6102.
[44] M. Islam, E. Rojas, D. Bergey, A. Johnson, A. Yodh, Nano Lett., 3 (2003) 269-273.
[45] W. Wenseleers, I. I. Vlasov, E. Goovaerts, E. D. Obraztsova, A. S. Lobach, A. Bouwen, Adv. Funct. Mater., 14 (2004) 1105-1112.

[46] V. C. Moore, M. S. Strano, E. H. Haroz, R. H. Hauge, R. E. Smalley, J. Schmidt, Y. Talmon, Nano Lett., 3 (2003) 1379-1382.
[47] T. Fujigaya, N. Nakashima, Polym. J., 40 (2008) 577-589.
[48] Y. Tomonari, H. Murakami, N. Nakashima, Chem. A, Eur. J., 12 (2006) 4027-4034.
[49] R. J. Chen, Y. Zhang, D. Wang, H. Dai, J. Am. Chem. Soc., 123 (2001) 3838-3839.
[50] Y. Ji, Y. Y. Huang, A. R. Tajbakhsh, E. M. Terentjev, Langmuir, 25 (2009) 12325-12331.
[51] J. Liu, O. Bibari, P. Mailley, J. Dijon, E. Rouvière, F. Sauter-Starace, P. Caillat, F. Vinet, G. Marchand, New J. Chem., 33 (2009) 1017-1024.
[52] S. Meuer, L. Braun, R. Zentel, Macromol. Chem. Phy., 210 (2009) 1528-1535.
[53] A. Star, J. F. Stoddart, D. Steuerman, M. Diehl, A. Boukai, E. W. Wong, X. Yang, S. W. Chung, H. Choi, J. R. Heath, Angew. Chem., 40 (2001) 1721-1725.
[54] M. Giulianini, E. R. Waclawik, J. M. Bell, M. De Crescenzi, P. Castrucci, M. Scarselli, N. Motta, App. Phy. Letters, 95 (2009) 013304.
[55] J. Zou, L. Liu, H. Chen, S. I. Khondaker, R. D. Mccullough, Q. Huo, L. Zhai, Adv. Mater., 20 (2008) 2055-2060.
[56] M. J. O'connell, P. Boul, L. M. Ericson, C. Huffman, Y. Wang, E. Haroz, C. Kuper, J. Tour, K. D. Ausman, R. E. Smalley, Chem. Phy. Lett., 342 (2001) 265-271.
[57] Y. Kang, T. A. Taton, J. Am. Chem. Soc., 125 (2003) 5650-5651.
[58] K. Matyjaszewski, J. Xia, Chem. Rev., 101 (2001) 2921-2990.
[59] L. M. Robeson, J. Membr. Sci., 62 (1991) 165-185.
[60] L. M. Robeson, J. Membr. Sci., 320 (2008) 390-400.
[61] M. Jia, K. V. Peinemann, R. D. Behling, J. Membr. Sci., 57 (1991) 289-292.
[62] H. Kim, H. G. Kim, S. Kim, S. S. Kim, J. Membr. Sci., 344 (2009) 211-218.
[63] S. Kim, T. W. Pechar, E. Marand, Desalination, 192 (2006) 330-339.
[64] D. M. Ackerman, A. I. Skoulidas, D. S. Sholl, J. K. Johnson, Mol. Simulat., 29 (2003) 677-684.
[65] S. Kim, L. Chen, J. K. Johnson, E. Marand, J. Membr. Sci., 294 (2007) 147-158.
[66] A. Fonseca, S. Reijerkerk, J. Potreck, K. Nijmeijer, Z. Mekhalif, J. Delhalle, Desalination, 250 (2010) 1150-1154.
[67] S. Sanip, A. Ismail, P. Goh, T. Soga, M. Tanemura, H. Yasuhiko, Separ. Purif. Technol., (2011).
[68] J. H. Choi, J. Jegal, W. N. Kim, J. Membr. Sci., 284 (2006) 406-415.
[69] C. Tang, Q. Zhang, K. Wang, Q. Fu, C. Zhang, J. Membr. Sci., 337 (2009) 240-247.
[70] E. Celik, H. Park, H. Choi, Water Res., 45 (2011) 274-282.
[71] S. Majeed, D. Fierro, K. Buhr, J. Wind, B. Du, A. Boschetti-de-Fierro, V. Abetz, J. Membr. Sci., 403-404 (2012) 101-109.

# Chapter 3. Experimental Part

## 3.1 Materials

1-pyrenebutyric acid, sodium sulfate, *n*-hexane, N,N,N′,N″,N″-Pentamethyldiethylenetriamine (PMDETA), copper bromide (CuBr), anisole, styrene, methyl methacrylate, ethyl α-bromoisobutyrate, 2,2'-Azobis(4-methoxy-2,4-dimethylvaleronitrile), triethylamine (TEA), and 2-methyl-3-nitro-2-nitrosopropionate were purchased from Sigma Aldrich. Aminopropylisobutyl POSS (APiB-POSS) was purchased from Hybrid Plastics. Methanol, ethanol, butanol, diethylether, tetrahydrofuran (THF), lithium chloride (LiCl), *N,N*-dimethylacetamide (DMAc), *N,N*-dimethylformamide (DMF), and toluene were purchased from Merck. All organic solvents were used as received or were additionally distilled. The MWCNTs obtained by chemical vapor deposition with purity of >98 %, surface area of 250 $m^2/g$, tube diameter in the range of 12 to 15 nm and 8 to 12 walls were provided by FutureCarbon GmbH. Pre-functionalized MWCNTs containing amine and hydroxyl groups were also received from FutureCarbon GmbH.

Poly(vinylidene fluoride) (PVDF) Kynar® F6000, with an average molecular weight of 250 Kg/mol, was obtained from Atofina Chemicals Inc. Polyacrylonitrile (PAN) with an average molecular weight of 200 Kg/mol was obtained from Dolan GmbH, Germany. Dehesive 940 (PDMS precursor), crosslinker V24, and catalyst OL were purchased from Wacker Silicones GmbH, Germany. In house prepared polyacrylonitrile (PAN) microporous membrane, with average pore size 20 nm and 15 % surface porosity, was used for composite membrane fabrication.

## 3.2 Surface Functionalization of MWCNTs

Molecular species were immobilized on MWCNTs by covalent and non-covalent bonding.

### 3.2.1. Non-Covalent Functionalization

Pyrene-POSS was used as dispersant for non-covalent functionalization of MWCNTs. Pyrene-POSS was prepared from pyrenebutyric acid and APiB-POSS via amidation reaction.

#### 3.2.1.1 Synthesis of Pyrene-POSS Nanohybrid

The reaction scheme for the synthesis of pyrene-POSS is shown in Fig. 3.1. 1-pyrenebutyric acid (3.5 mmol) and an excess amount of thionyl chloride (68 mmol) were transferred to a 25 mL flask and refluxed at 65 °C for 2 h. After reflux, unreacted thionyl chloride was removed by distillation until the dry pyrenebutyryl chloride remained in the flask. The solid pyrenebutyryl chloride was dissolved in 5 mL anhydrous tetrahydrofuran (THF). APiB-POSS (3.5 mmol) and triethylamine (7.1 mmol) were dissolved in 10 mL anhydrous THF separately. The APiB-POSS solution was taken in an additional funnel and added dropwise to the pyrenebutyryl chloride solution below 0 °C. After complete addition of APiB-POSS, the reaction content was stirred for 20 h at ambient temperature. The reaction mixture was dissolved in diethyl ether and washed with water excessively. After washing with water, the organic layer was extracted and dried over sodium sulfate. Finally, diethyl ether was evaporated and the product was vacuum-dried at room temperature resulting in the product with 80 % yield [1].

#### 3.2.1.2 Functionalization of MWCNTs by Pyrene-POSS

The reaction data of pyrene-POSS for functionalization of MWCNTs is shown in Table 3.1. Pyrene-POSS (300 mg) was dissolved in 50 mL THF, and dry MWCNTs were added to reach 1:1 weight ratio. The resultant mixture was sonicated for 5 h using Sonorex Super RK 255 H ultrasonic bath from Bandelin (Bandelin Electronic GmbH & Co. KG, Berlin, Germany), operated at a frequency of 35 KHz and an effective power of 160 W. The temperature was maintained at 20–25 °C during sonication. After sonication, MWCNTs were washed at least five

times with THF to remove non-adsorbed pyrene-POSS followed by vacuum drying at room temperature for 24 h. The functionalization of MWCNTs was also carried out at 1:0.2, 1:0.6, 1:2, and 1:3 weight ratios between MWCNTs and pyrene-POSS, respectively, to investigate the effect of the increased quantity of pyrene-POSS on its degree of adsorption on MWCNTs.

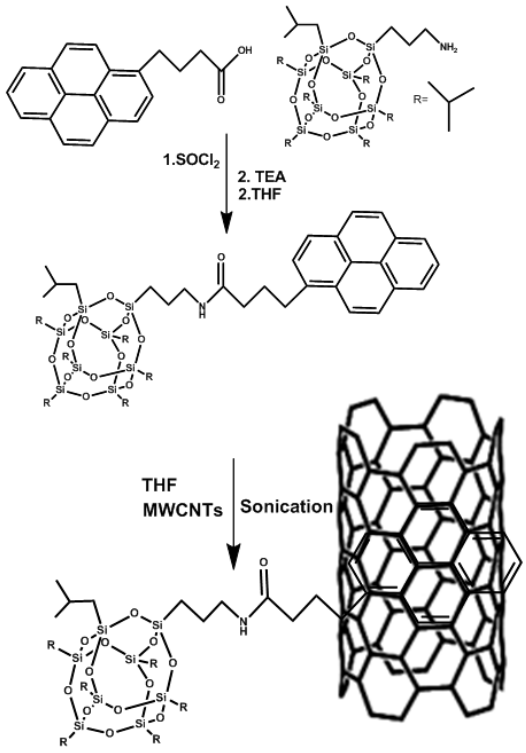


Figure 3.1: Reaction scheme for the preparation of pyrene-POSS and functionalization of MWCNTs with pyrene-POSS.

Table 3.1: Data for functionalization of MWCNTs by pyrene-POSS

| Ent. | MWCNTs/Pyrene-POSS ratio [a)] | Pyrene/MWCNTs surface area ratio [b)] |
|---|---|---|
| 1 | 1:0.2 | 63:250 |
| 2 | 1:0.6 | 190:250 |
| 3 | 1:1 | 315:250 |
| 4 | 1:2 | 630:250 |
| 5 | 1:3 | 950:250 |

a) Ratio of pyrene-POSS to pristine MWCNT used for modification.
b) Surface area ratio by considering the area of pyrene unit as 60 $Å^2$ in pyrene-POSS w.r.t. MWCNTs.

### 3.2.2. Covalent Functionalization of MWCNTs

Prefunctionalized i.e., amine end functionalized MWCNTs (MWCNTs-$NH_2$) were used for covalent functionalization of MWCNTs. FutureCarbon GmbH supplied MWCNTs-$NH_2$, functionalized via diazotation reaction. Phenylamine was the end group molecular specie in MWCNTs-$NH_2$. The concentration of –$NH_2$ functional groups was calculated by thermogravimetric analysis (TGA).

#### 3.2.2.1 Initiator Immobilization on MWCNTs

The scheme of initiator immobilization is shown in Fig. 3.2. MWCNTs-$NH_2$ were taken in the Schlenk flask and anhydrous tetrahydrofuran (THF) was added (12 mL/100 mg MWCNTs) followed by 10 minutes ultrasonication. Then triethylamine (TEA) was added to the above mixture and the system was purged with argon (Ar) for 30 minutes. Five cycles of Ar and vacuum were applied to the system by purging Ar and evacuating the system in an alternating way. Then the solution of 2-BriB, prepared in THF (1:10 V/V), was added drop wise to carry out the amidation reaction below 0°C. The molar ratio between 2-BriB and TEA was kept 1:1.2, respectively. After addition of 2-BriB the system was kept below 0°C for two hours and later for 48 hours at room temperature (18-20°C). MWCNTs were washed with chloroform 5 times to remove quarternary amine salt produced during the reaction. Finally, initiator immobilized MWCNTs were dried under vacuum at room temperature for 24 h.

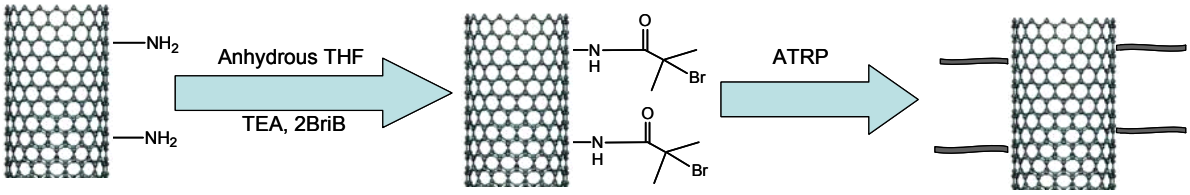


Figure 3.2: Schematic representation of initiator immobilization on MWCNTs-$NH_2$ and ATRP reaction.

#### 3.2.2.2 Grafting of Poly(methyl methacrylate) and Polystyrene via ATRP

Initiator modified MWCNTs were charged to the Schlenk flask. CuBr (0.66 mol % with respect to monomer), PMDETA (0.66mol % with respect to monomer) and monomer (styrene or methyl methacrylate) were added to the Schlenk flask according to the preset monomer to initiator ratio. In all the experiments anisole was used as solvent and the amount of solvent was taken ¼ times the amount of monomers (by volume). The above mixture was sonicated for 10 minutes and bubbled with Ar for 30 min. Then sacrificial initiator, ethyl 2-bromoisobutyrate (EBiB), was added to the reaction mixture and the flask was put inside the oil bath preheated to the required temperature for the desired time duration (temperature was chosen 60 °C for MMA and 90 °C for styrene). The described procedure was for ATRP reactions carried out in the presence of sacrificial initiator. For the reactions carried out in the absence of sacrificial initiator, PMDETA was added at the end after the bubbling of the reaction mixture with Ar. Polymer grafted MWCNTs were washed with THF to remove the content of free polymer. Finally, MWCNTs were dried under vacuum at room temperature for 24 h.

#### 3.2.2.3 Grafting of Poly(methyl methacrylate) onto MWCNTs

PMMA modified MWCNTs via “grafting onto” method were supplied by our project partner, Université DE Liège, Belgium. The PMMA chains were synthesized by nitroxide mediated polymerization (NMP) and end-capped by a cleavable alkoxyamine (PMMA-$ONR_2$). The schematic representation of PMMA grafting onto MWCNTs is shown in Fig. 3.3.

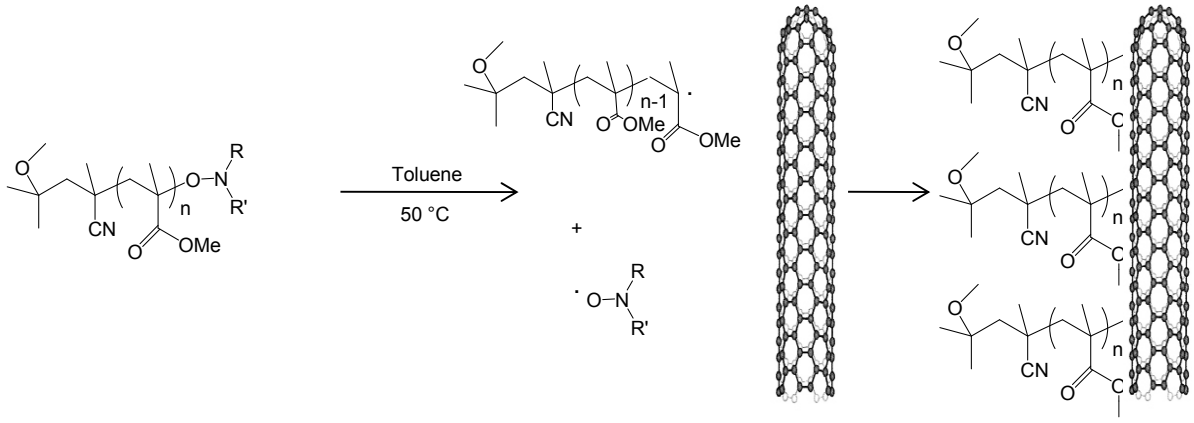


Figure 3.3: Schematic diagram of the grafting of alkoxyamine end-capped PMMA chains onto MWCNTs.

0.075 g (0.426 mmol) of 2-methyl-3-nitro-2-nitrosopropionate and 0.13 g (0.421 mmol) of 2,2'-Azobis(4-methoxy-2,4-dimethylvaleronitrile) were charged in a 500 ml round bottomed flask and degassed by several vacuum-nitrogen cycles. Degassed MMA (200 mL, 1.88 mol) was then added and the mixture was heated at 50°C for 3h. Then THF was added in reaction mixture for dilution. The polymer was precipitated in methanol. After filtration the polymer was dried under vacuum.

1 g MWCNTs and 10 g of PMMA-ONR$_2$ were added in a 250 mL round bottomed flask and degassed by several vacuum-nitrogen cycles. 100 mL of degassed toluene was added and the mixture was placed under sonication for 5 min and then heated under vigorous stirring (1000 rpm) at 50 °C for 17 h. MWCNTs were washed with toluene to remove non grafted polymer and finally vacuum dried at 80°C for 24 h.

### 3.3 PVDF Membrane Fabrication

The polymer solution for pure PVDF membranes comprised of 5.6 wt. % of LiCl, 78.4 wt. % DMAc, and 16 wt. % PVDF. For nanocomposite membrane preparation, MWCNTs were loaded with respect to PVDF. For the preparation of solutions, LiCl was dissolved in DMAc followed by addition of the MWCNTs to

the solution. This mixture was sonicated by tip sonication for 45 min and then by bath sonication for 3 h under mechanical stirring (500 rpm) at 60°C. Finally, PVDF was added to the sonicated mixture and dissolved at 60°C for 24 hours. The solution was cooled down to room temperature and evacuated for approximately 10 min to remove bubbles. The solution was cast on polyester nonwoven fleece by casting machine with a knife gap of 200 µm. The cast solution was coagulated in distilled water at 20°C (±1) to carry out phase separation. After the completion of phase separation the membranes were washed with hot water (70°C) and finally dried at 100 °C.

### 3.4 PAN Membrane Fabrication

The casting solution for pure membranes comprised of 14 wt. % PAN and 86 wt. % DMF. The solution for MMMs contained 14 wt. % PAN/MWCNTs and 86 wt. % of DMF. The ratios between PAN and MWCNTs were kept as 99.5:0.5, 99:1 and 98:2, in order to maintain the loading of MWCNTs as 0.5, 1.0 and 2.0 wt. %, respectively. For the preparation of the solution, MWCNTs were mixed with DMF and the resultant mixture was subjected to tip sonication (operated at 55 W) for 5 minutes. Then PAN was added to the dispersion and the mixture was stirred for 48 hours at 70°C to obtain a homogeneous solution. After cooling the solution to room temperature, it was degassed to ensure complete removal of air bubbles before membrane casting.

Non-woven polyester was attached to a glass plate and the polymer solution was cast with a doctor blade using a knife gap of 200 µm followed by immediate immersion into the coagulation bath containing water at 20°C. After complete precipitation, the membranes were kept in water at room temperature for at least 24 hours to remove the remaining solvent prior to further characterization [2].

### 3.5 Fabrication of PDMS Membranes

PDMS dense films and composite membranes were prepared by the solvent evaporation method.

### 3.5.1 Fabrication of PDMS Dense Membranes

PDMS dense films were fabricated using purified and pyrene-POSS modified MWCNTs. 50 g PDMS solution, prepared in toluene, contained 5 wt. % PDMS, different loading of MWCNTs (0.5, 1 and 3 wt. %) with respect to PDMS, catalyst (OL) and crosslinker (V24). To prepare the solution, MWCNTs were mixed in toluene and the resultant mixture was sonicated for 1 h followed by the addition of Dehesive 940 (PDMS precursor). The above mixture was stirred for 3 h to homogenize the solution. The required amounts of catalyst (OL) and crosslinker (V24) were very small and for their accurate addition, 1 wt. % solution was prepared in toluene. 1 wt. % solution of crosslinker (V24) was added in PDMS solution followed by brief stirring of the system for 10 min. Finally, 1 wt. % solution of catalyst (OL) was added in the solution and system was stirred again for 10 min to complete the solution preparation. The solution was cast in Teflon support and evaporated at 40°C. After complete evaporation of the solvent, the PDMS films were dried and crosslinked at 80°C under vacuum for 12 h.

### 3.5.2 Fabrication of PDMS Composite Membranes

Appropriate amounts of MWCNTs were dispersed in 25 g toluene by sonication. Dehesive 940 was added to the MWCNTs dispersion to maintain a 4 wt. % concentration of PDMS/MWCNTs and effective loading of 1, 2, 3, 4, and 5 wt. % of MWCNTs with respect to PDMS. The mixture was stirred for 3 h to obtain a homogeneous dispersion. Crosslinker (V24) and catalyst (OL) were added to the solution followed by brief vigorous stirring to homogenize the system. The PDMS solution was dip-coated on top of a polyacrylonitrile (PAN) microporous membrane. The solvent was evaporated at room temperature and PDMS composite membranes were cross-linked in an oven at 70 °C for 1 h.

## 3.6 Characterization Techniques

### 3.6.1 Fourier Transform Infrared Spectroscopy (FTIR)

Fourier transform infrared (FTIR) spectroscopy was conducted using a Bruker Equinox 55. The MWCNTs samples were prepared by dispersing them in KBr and pressing the mixed powders to form pellets. A pure KBr pellet was also prepared and used as a reference. PAN membrane samples were prepared by grinding dried membrane in KBr and then pressing the ground powder to form KBr pallet. The pellets were vacuum dried at 35 °C for 12 hours. FTIR spectra of organic compounds were taken on an ATR cell fitted with a diamond crystal. The measurements were carried out in a spectral range of 400-4000 $cm^{-1}$ with a spectral resolution of 4 $cm^{-1}$and 64 scans.

### 3.6.2 Raman Spectroscopy

The Raman spectra of PAN nanocomposite membranes and MWCNTs were measured by Bruker SENTERRA Raman microscope ($\lambda$ = 785 nm, 10 mW) at room temperature.

### 3.6.3 Viscosity Measurements

The viscosities of PVDF and PAN solutions were measured with a Europhysics® Rheo 2000 rheometer. Measurements were performed for two min at 20 °C using cone / plate geometry (C25-1). The viscosity measurement of PVDF solution was carried out at a shear rate of 500 $s^{-1}$ and of PAN solution was measured at a shear rate of 100 $s^{-1}$.

### 3.6.4 Scanning Electron Microscopy (SEM)

Scanning electron microscope studies on the membranes were carried out with a LEO Gemini 1550 VP from Zeiss with field emission cathode operated at 1 – 1.5

kV. The sample preparation for cross section analysis was done under cryogenic conditions. The membrane samples were sputtered by a very thin layer of Au/Pd.

### 3.6.5 Transmission Electron Microscopy (TEM)

TEM experiments were carried out using FEI Tecnai $G^2$ F20 at 200kV. MWCNTs were dispersed in THF (1 % w/v) by tip sonication for 15 min. 5 µL of MWCNTs dispersion was deposited on TEM grid. For TEM studies, PAN nanocomposite membranes were fabricated by phase inversion on a glass plate without using non-woven polyester as a support. Films having an approximate thickness of 50 µm were embedded with epoxy. Ultrathin sections of approximately 70 nm were cut in a Leica Ultra microtome under cryogenic conditions (-130°C).

### 3.6.6 Porosity Measurements

The porosity measurements of PAN membranes were carried out by the dry-wet method using the expression given in eq. 3.1:

$$Porosity = \frac{W_2 - W_1}{V \cdot d_{butanol}} \times 100\% \qquad 3.1$$

where '$w_1$' (g) is the weight of dry membrane, '$w_2$' (g) is the weight of membrane after dipping into 1-butanol for 2 hours, '$v$' ($cm^3$) is the volume of the membrane and $d_{butanol}$ ($g/cm^3$) is the density of 1-butanol at room temperature.

### 3.6.7 Contact Angle Measurements

The contact angle goniometer from Kruess was used to characterize the membrane surface polarity. The contact angle measurements on the membrane surface were carried out using a droplet of 5 µL at room temperature. The measurements were recorded after 5 sec of water droplet deposition. As the final

data, the mean of five values of contact angles on different areas of the membranes was used.

### 3.6.8 Water Flux Measurements

Water flux measurements were performed using a cross flow cell where the membranes with an effective area of 1.54 $cm^2$ were analyzed at 22°C. The schematic diagram of the cross flow cell is shown in Fig. 3.4. The water flux was calculated by eq. 3.2:

$$J = \frac{V}{A \cdot t} \qquad 3.2$$

where 'J' represents the flux of the membrane measured as $lm^{-2}h^{-1}$, 'V' the permeate volume measured in litre (l), 'A' the membrane active surface area ($m^2$) and 't' the time required to obtain the required volume across the membrane (h). The feed flow rate was kept at 480 ml/min and the flux was calculated at different transmembrane pressures i.e. 2, 4, 6, 8, and 10 bar in order to study the membrane compaction behaviour. For the flux measurements, the transmembrane pressure was maintained at 2 bar for 40 minutes and then water flux was calculated. Afterwards, the pressure was increased gradually and each pressure (4 to 10 bars) was maintained for 10 minutes followed by the measurement of water flux at that corresponding pressure. Three membrane stamps were analyzed to demonstrate the water flux behaviour.

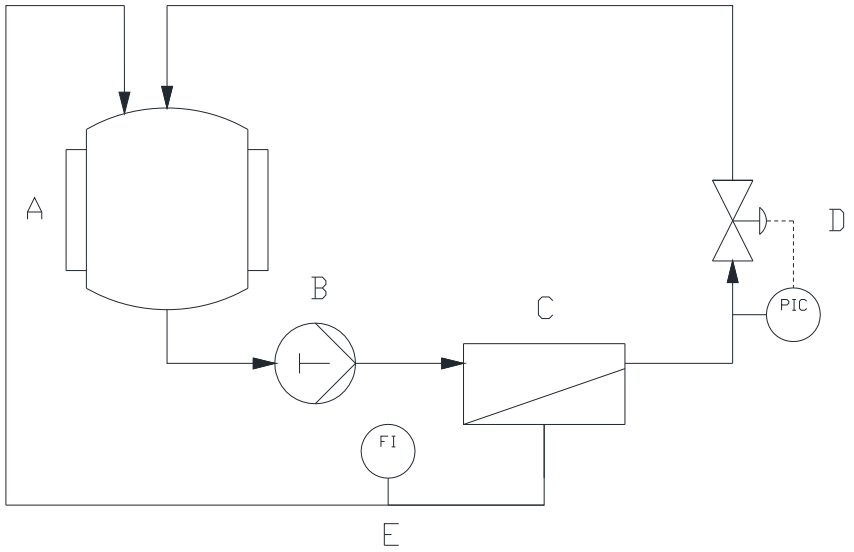


Figure 3.4: Schematic diagram of cross flow mode depicting different parts: (A) Support vessel, (B) Feed pump, (C) Membrane cell, (D) PIC (Pressure indicator and controller), (E) FI (Flow indicator).

### 3.6.9 Rejection Measurements

330 ppm solution of dextrans with different molecular weights (Table 3.2) was prepared in deionized water. The membrane stamps having an effective area of 15.2 $cm^2$ were used and measurements were done in a Millipore cell under a pressure drop of 2 bar. The analysis of feed, permeate, and retentate solutions was carried out by high performance liquid chromatography (HPLC) using a Waters® instrument equipped with a PSS® column (0.8 × 300 mm, 10 μm, Suprema Linear M) attached with a differential refractometer (Waters® 2410 RI), autosampler Waters 717+ at a flow rate of 1 ml/min at 35°C using tetrahydrofuran (THF) as internal standard. The results were calibrated with dextran standards. The values of retention were calculated using eq. 3.3:

$$R = 1 - \frac{c_P}{(c_F + c_R)/2} \qquad 3.3$$

where '$c_P$', '$c_F$' and '$c_R$' are the concentrations of permeate feed and retentate solutions (g/l), respectively.

Table 3.2: Data of molecular weight of dextrans used for retention measurements

| Dextran Type | Molecular weight (Kg/mol) |
|---|---|
| Dextran FP1 | 0.9-1.2 |
| Dextran 4 | 4-6 |
| Dextran 35 | 35-50 |
| Dextran 100 | 100-200 |
| Dextran 500 | 350-550 |

### 3.6.10 Mechanical Characterization

PAN nanocomposite membranes were prepared by phase inversion process without using non-woven polyester to carry out mechanical characterization. A universal testing machine from Zwick, model Z020, with a load cell of 20 N was used to carry out the analysis. 5 cm effective length and 1 cm width stripes of the membranes were measured at a crosshead speed of 5 mm/min.

### 3.6.11 Gas Transport Properties

The diffusion, permeability, and solubility coefficients of $N_2$, $O_2$, $CH_4$, $CO_2$, $H_2$, and $C_2H_6$ for the dense membrane samples were measured using a constant volume/variable pressure time lag setup. The permeability coefficient was measured by eq. 3.4 [3].

$$P = D \cdot S = \frac{V_p \cdot l}{A \cdot R \cdot T \cdot \Delta t} \ln\left(\frac{p_f - p_{P1}}{p_f - p_{p2}}\right) \qquad 3.4$$

where ‘D’ is the diffusion coefficient, ‘S’ is the solubility coefficient, ‘$V_p$’ is the permeate volume, ‘l’ is the membrane thickness, ‘A’ is the effective membrane area, ‘R’ is the universal gas constant, ‘T’ is measurement temperature, ‘Δt’ is the time difference between the two points on the pressure increase curve, ‘$p_f$’ is the

feed pressure, and '$p_{p1}$' and '$p_{p2}$' are permeate pressures at two different time points (Fig. 3.5).

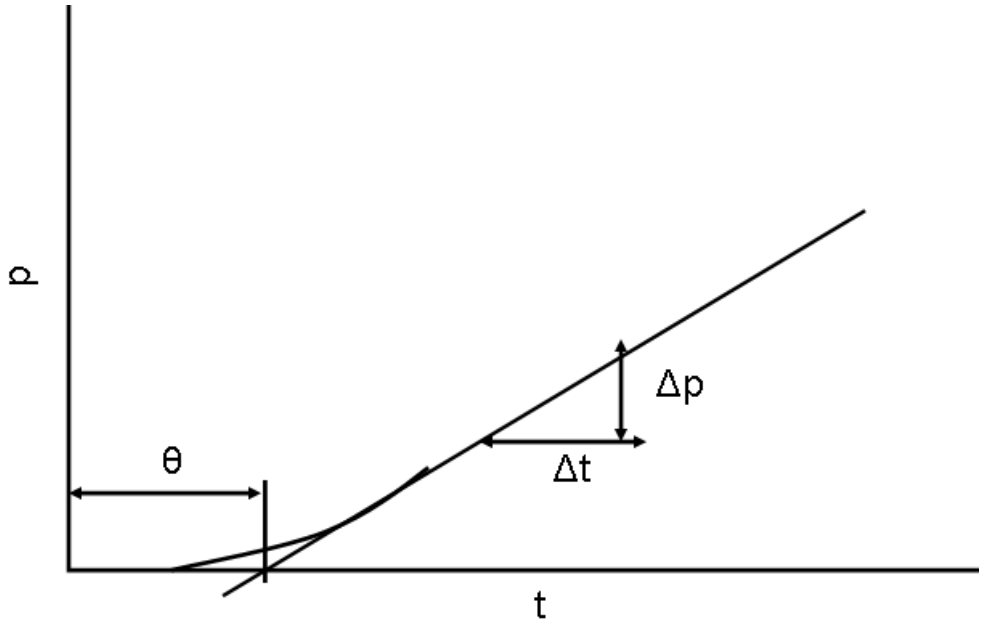


Figure 3.5: A typical time lag diagram for the gas transport measurement of dense membranes.

The diffusion coefficient was calculated using eq. 3.5:

$$D = \frac{l^2}{6\Theta} \qquad 3.5$$

Where '$\Theta$' is the time lag measured by extrapolating the permeation curve to transmembrane pressure of 0 (Fig. 3.5) and 'l' is the membrane thickness.

Gas permeance of PDMS composite membranes was measured by pressure increase test unit (Fig. 3.6) at 23 °C. The permeance values of the membranes were measured in $m^3/m^2 \cdot h \cdot bar$. The gas permeance of the membranes was also measured as a function of temperature. The activation energy of permeation was measured by Arrhenius formula (eq. 3.6) [4]:

$$L = L_{\circ} e^{\left(\frac{-E_p}{RT}\right)} \qquad 3.6$$

where 'L' is the permeance, 'L$_\circ$' is the exponential factor, '$E_p$' is the activation energy of permeation (KJ/mol), 'R' is the universal gas constant and 'T' is absolute temperature (K).

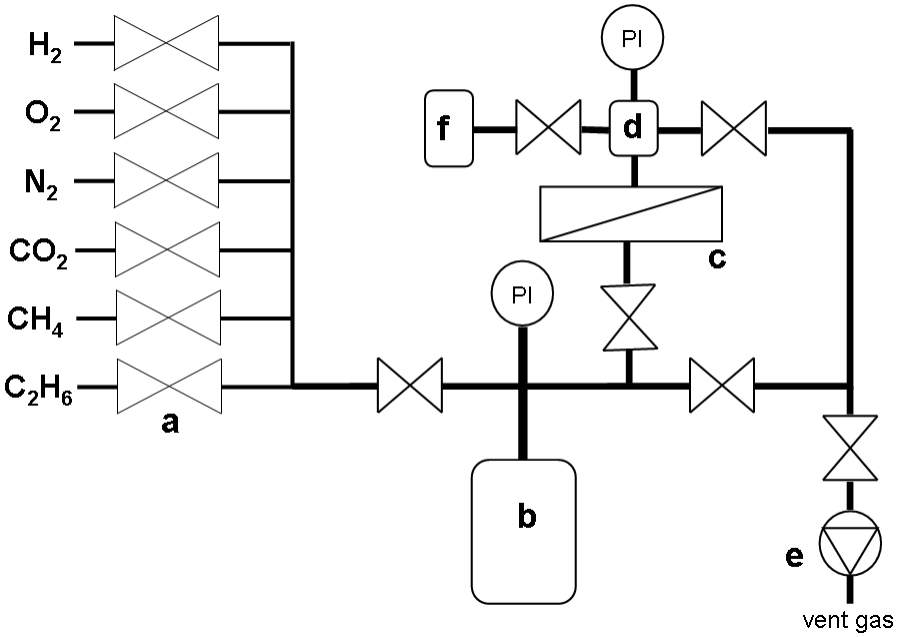


Figure 3.6: Pressure increase test unit (a) gas inlet, (b) feed pressure volume, (c) membrane test cell, (d) permeate volume, (e) vacuum pump, and (f) extra permeate volume.

### 3.6.12 Electrical Conductivity

Surface resistivity was analyzed with a 4-point measurement equipment from Jandel. It was measured in Ω/□. For the calculation of bulk resistivity (ρ) of a rectangular sample, the dimensions of the sample (Fig. 3.7) i.e., cross sectional area (A) and length (l) are put in eq. 3.7:

$$\rho = R\frac{A}{l} \qquad 3.7$$

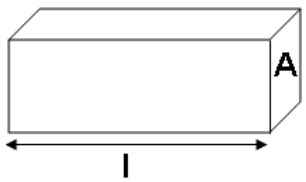


Figure 3.7: Dimensions of a rectangular sample for bulk conductivity measurement.

where 'R' is the resistance. Since the PDMS nanocomposite layers had non uniform thickness, their electrical properties are described in terms of resistivity measured in Ω/□.

### 3.6.13 Thermogravimetric Analysis (TGA)

TGA measurements were done using Netzsch TG209 F1 Iris, under constant argon flow of 20 mL/min, from 25 °C to 900 °C, at a constant rate of 20°C/min.

### 3.6.14 Nuclear Magnetic Resonance (NMR) Spectroscopy

Nuclear magnetic resonance (NMR) spectra of organic compounds were recorded on Bruker AV-300 (Bruker Biospin GmbH, Karlsruhe, Germany) at 300 MHz. The samples were dissolved in $CDCl_3$ containing tetramethylsilane (TMS).

### 3.6.15 Optical Microscopy

Optical microscopy images were taken with a Leica DMLM and samples were imaged under reflection mode.

### 3.6.16 Bubble Point Measurements

The surface pore size analysis was carried out by poremeter 4.900 from Porous Material Inc. The membrane stamps were cut into a diameter of 2.5 cm followed by dipping in a special liquid (Porewick®) of known surface tension (16 dyn/cm). $N_2$ was kept flowing with gradually increased pressure. The driving force (pressure) takes out the liquid from membrane pores. The pore diameter can be calculated by eq. 3.8 [5]:

$$D = \frac{4\sigma \cos\theta}{p} \qquad 3.8$$

where ‘D’ is the pore diameter, ‘σ’ is the surface tension of the liquid used, ‘θ’ is the contact angle of the liquid and ‘p’ is the applied pressure.

### 3.6.17 Membrane Pressure Treatment

PVDF membranes were treated with high pressure for the evaluation of compaction. Surface of the membrane was covered by aluminum foil and subsequently pressurized at a pressure of 30 bars. The flow of $N_2$ was measured at different time intervals at 0.2 bar feed pressure by taking aside the aluminium foil and then covering and pressurizing the membrane again [6].

## 3.7 References

[1] S. Majeed, V. Filiz, S. Shishatskiy, J. Wind, C. Abetz, V. Abetz, Nanoscale Res. Lett., 7 (2012) 296.
[2] S. Majeed, D. Fierro, K. Buhr, J. Wind, B. Du, A. Boschetti-de-Fierro, V. Abetz, J. Membr. Sci., 403-404 (2012) 101-109.
[3] S. Shishatskiy, J. R. Pauls, S. P. Nunes, K. V. Peinemann, J. Membr. Sci., 359 (2010) 44-53.
[4] M. Mulder, Basic Principles of Membrane Technology, 2nd edi., Kluwar Publishers, 1996.
[5] J. H. Choi, J. Jegal, W. N. Kim, J. Membr. Sci., 284 (2006) 406-415.
[6] K. Ebert, D. Fritsch, J. Koll, C. Tjahjawiguna, J. Membr. Sci., 233 (2004) 71-78.

# Chapter 4. Surface Functionalization of Multi-walled Carbon Nanotubes (MWCNTs)

## 4.1 Introduction

The extraordinary electrical, mechanical, and thermal properties of carbon nanotubes (CNTs) make them the strongest candidates for their application in composite materials [1-3]. Good dispersion of CNTs is required for their application in composite materials. However, CNTs are produced in the form of bundles where they are attracted together by van-der-Waals and π-π interactions. The aggregation of CNTs in the form of bundles influences the properties of the resulting composite materials e.g., ineffective stress transfer and higher percolation thresholds for electrical conductivity. Moreover, the agglomerates of carbon nanotubes may act as conventional carbon black and hence, to obtain improved material properties, the disaggregation of CNTs agglomerates is necessary [4-6].

Surface modification of CNTs is a tool to improve their dispersion in various solvents and matrices and it can be grouped into two different categories: (a) physical adsorption or wrapping of a variety of functional molecules via non-covalent interactions [7-11] and (b) binding the chemical functional groups on the π-conjugated skeleton of CNTs via covalent bonding. Non-covalent functionalization has an advantage over covalent functionalization because no major side wall defects occur thus preserving the electronic properties of π-conjugated tubular structure of CNTs. Such functionalization involves wrapping of the CNTs surface by various polymers, polynuclear aromatic compounds, surfactants, or biomolecules [11]. Ionic and biological surfactants improve the CNTs dispersion in aqueous solutions where CNTs are entrapped into hydrophobic interiors of micelles leading to a stable dispersion [12]. Conjugated polymers interact with CNTs by π-π stacking, resulting in better dispersion of CNTs in specific organic solvents [13]. Block copolymers, having at least one block exhibiting conjugation and other having high affinity towards the solvent,

lead to a better dispersion of CNTs in solvents of different polarities [14]. Polycyclic aromatic compounds e.g., pyrene, are also well known for their π-π stacking on CNTs surface, and the attachment of pyrene to molecular species which are soluble in organic solvents or aqueous media creates the possibility to effectively disperse CNTs in these solvents [12].

Covalent functionalization is also regarded as the defect functionalization as it is carried out by introducing defect sites on perfect structure of CNTs. The hybridization of carbon atoms on CNTs changes from $sp^2$ to $sp^3$ resulting in loss of conjugation. Different chemical functional groups and polymer chains can be covalently bound to the surface of CNTs [15]. A detailed overview of polymer binding on CNTs via “grafting onto” and “grafting from” is described in Chapter 2. Incorporation of chemical functionalities improves their dispersibility in organic solvents, aqueous solutions, and polymer matrices depending on the types of functional groups or polymer chains attached to the CNTs surface.

In this chapter surface modification of multi-walled carbon nanotubes (MWCNTs), carried out by both non-covalent and covalent means, is presented. For non-covalent functionalization of MWCNTs, 1-pyrenebutyric acid (PBA) was attached covalently to polyhedral oligomeric silsesquioxanes (POSS), and MWCNTs were modified with the resultant pyrene-POSS (PPy). π-π stacking interactions of pyrene with graphitic walls of MWCNTs enable the adsorption of PPy hybrid on MWCNTs. POSS possesses an inorganic cage structure, with the possibility for a variety of functional groups of different nature to be attached to the $Si_8O_{12}$ core [16, 17] and provides the opportunity to disperse the functionalized CNTs in organic solvents and polymer matrices. Poly(methyl methacrylate) and polystyrene were grafted from the initiating sites, immobilized on MWCNTs, by atom transfer radical polymerization (ATRP). The obtained functionalized MWCNTs were used for the fabrication of mixed matrix membranes (MMMs) which are discussed in chapter 5, 6, and 7.

## 4.2. Results and Discussion

### 4.2.1 Non-Covalent Functionalization of MWCNTs

Covalent functionalization of MWCNTs with aminopropylisobutyl POSS (AP*i*B-POSS) has been reported in literature for the case of MWCNTs dispersion in THF [18]. In the present study, the preparation of nanohybrid dispersant molecules based on AP*i*B-POSS and pyrene for the physical surface modification of MWCNTs has been presented. Besides conserving the intrinsic properties of the MWCNTs, it was a task to improve their dispersibility not only in a polar solvent like THF, but also in non-polar solvents like toluene and *n*-hexane. The improved dispersion of MWCNTs in non-polar solvents provides a way to fabricate PDMS nanocomposites by solvent evaporation from a mixed solution of polymer and nanofiller.

The successful synthesis of PPy hybrid is evident from $^{1}$H-NMR measured in $CDCl_3$. The amine protons of AP*i*B-POSS (at 1.38 ppm in Fig. 4.1) disappeared in PPy after the amidation reaction. The appearance of the amide proton was confirmed by integrating the peak area of pyrene protons, whereby an increase in the peak area indicates the addition of one proton which is the amide proton (Fig. 4.2). Fig. 4.1 shows that after the amidation reaction, aliphatic chain protons of 1-pyrenebutyric acid (PBA) i.e., a (3.42 ppm), b (2.18 ppm), and c (2.51 ppm) underwent shifts to a´ (3.30 ppm), b´ (1.85 ppm), and c´ (2.18 ppm), respectively, in PPy. Also, h (1.53 ppm) and j (2.68 ppm) protons of AP*i*B-POSS shifted to h´ (1.62 ppm) and j´ (3.30 ppm) in PPy after reaction. These peak shifts clearly indicate the absence of unreacted PBA and AP*i*B-POSS.

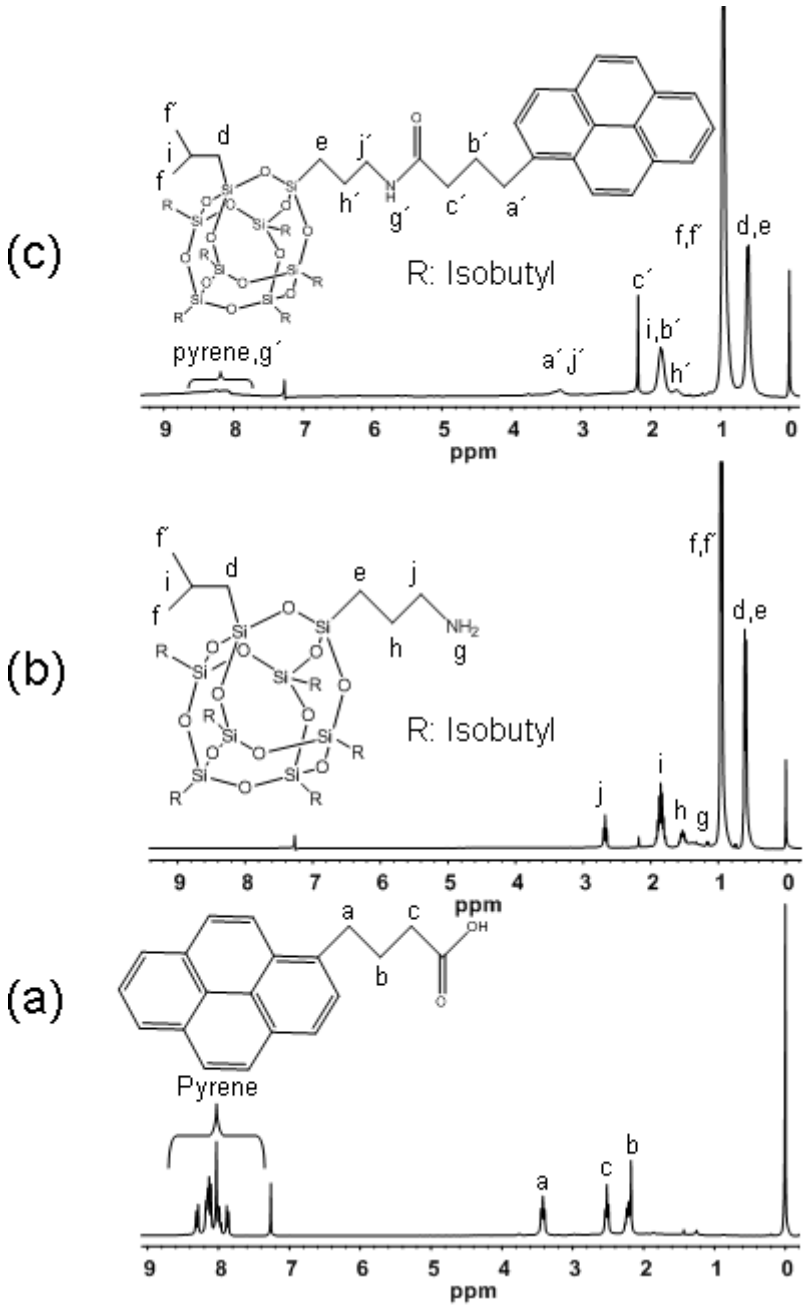


Figure 4.1: Proton NMR measured in $CDCl_3$ (a) PBA, (b) AP*i*B-POSS and (c) PPy.

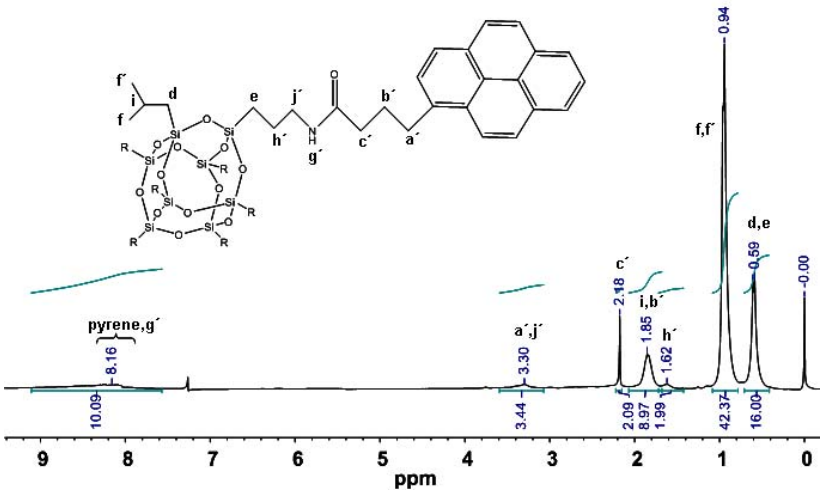


Figure 4.2: Integration of proton NMR spectrum of PPy.

The FTIR study also confirms the successful synthesis of PPy (Fig. 4.3). The spectrum of PBA shows the characteristic carbonyl peak at 1690 $cm^{-1}$. After amidation reaction this peak shifted to 1660 $cm^{-1}$ which is characteristic for the carbonyl peak of amide groups. The appearance of a peak at 1524 $cm^{-1}$ confirms the N-H bending of the amide group [19]. The -OH stretching peak of PBA at 3035 $cm^{-1}$ disappeared in the case of PPy. The carboxylic acid group (-COOH) out of plane deformation vibration peak (~915 $cm^{-1}$) [20] was completely disappeared in case of PPy. The disappearance of peaks related to –COOH indicate their complete conversion into amide groups. The typical Si-O-Si peak was observed in both AP*i*B-POSS and PPy at 1085 $cm^{-1}$.

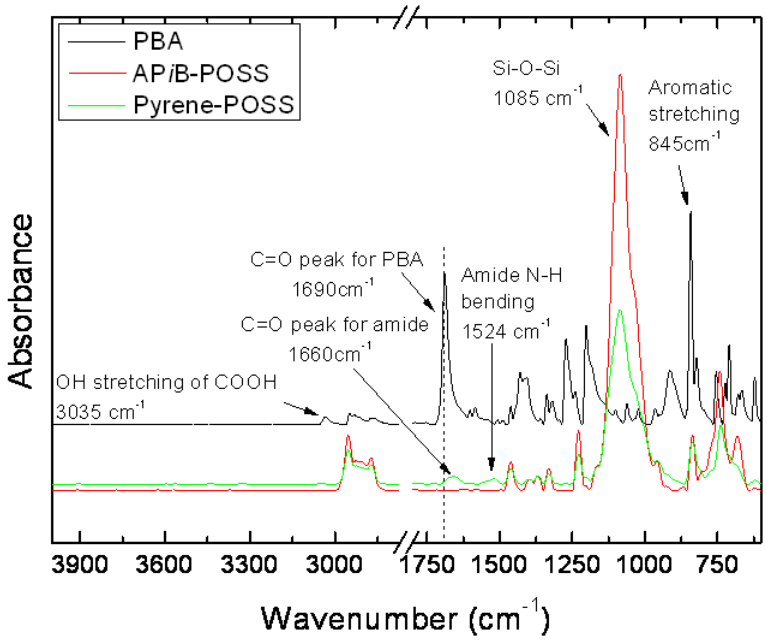


Figure 4.3: FTIR analysis of PBA, AP*i*B-POSS, and PPy.

Successful synthesis of PPy could be confirmed by the analysis of MWCNTs dispersion stability in organic solvents. Dispersion analysis was carried out by dispersing purified MWCNTs (MWCNTs-P) in THF, toluene, and *n*-hexane. For the preparation of the dispersions, 5 mg of PPy was dissolved in 25 mL of each solvent followed by the addition of MWCNTs leading to 1:1 weight ratio of MWCNTs and PPy. Then, the resultant mixture was subjected to tip sonication (Sonoplus, Bandelin Electronic GmbH & Co. KG, Berlin, Germany) operated at 55 W for 15 min. The homogeneous dispersion of MWCNTs could be observed in all three investigated solvents which remained stable after storage for one week (Fig. 4.4). However, the dispersions prepared in the absence of PPy were unstable and showed a rapid sedimentation within 10 min. The sediments of MWCNTs in *n*-hexane and toluene can be observed easily, but MWCNTs sediments in THF were observed along with suspended MWCNTs in THF (Fig. 4.4). In addition, the MWCNTs also underwent sedimentation when being dispersed in organic solvents in the presence of PBA and AP*i*B-POSS, which are educts for the PPy synthesis. This is a further strong indication of the dispersing property of this PPy hybrid.

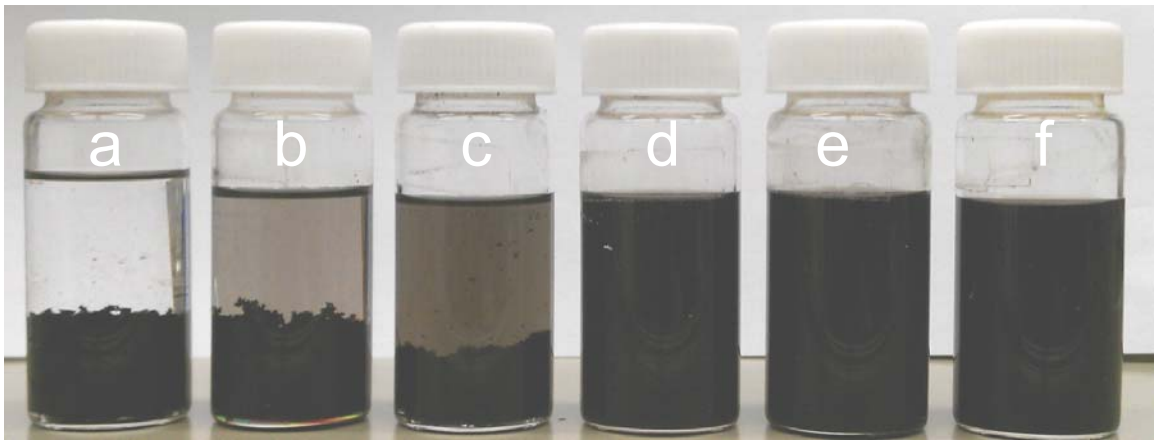


Figure 4.4: MWCNTs dispersions prepared without PPy in (a) *n*-hexane, (b) toluene, and (c) THF, and MWCNTs dispersions prepared with PPy in (d) *n*-hexane, (e) toluene and (f) THF.

Ji et al. functionalized CNTs (SWCNTs and MWCNTs) by pyrene modified poly(dimethylsiloxane) (PDMS) chains which resulted in a stable CNTs dispersion in non-polar solvents like petrol ether [9]. The stable dispersions were related to the pyrene-PDMS surfactant which interacts with CNTs by π-π interactions on pyrene end and PDMS chains being soluble in petrol ether led to stable dispersion of CNTs. CNTs dispersion were only possible in the presence of pyrene-PDMS surfactant, however, educts (PDMS and PBA) also led to the unstable dispersions.

TGA was used to confirm the physical adsorption of PPy on MWCNTs via π–π stacking. Fig. 4.5 shows the TGA of PPy, MWCNTs-P, and MWCNTs-PPy. MWCNTs-P did not show any mass loss until 700 °C. The decomposition of PPy took place between 250 °C and 570 °C. The TGA of the samples with different ratios between MWCNTs and PPy showed that the ratio has no significant influence on the adsorption degree of PPy on the MWCNTs above weight ratio of 1:0.6. From theoretical calculations, it is evident that the surface of MWCNTs can be saturated with pyrene units at 1:1 weight ratio. However, upon the investigated compositions, the 1:3 ratio between MWCNTs and PPy showed the highest mass loss which may indicate the presence of free or weakly adsorbed PPy (Table 4.1).

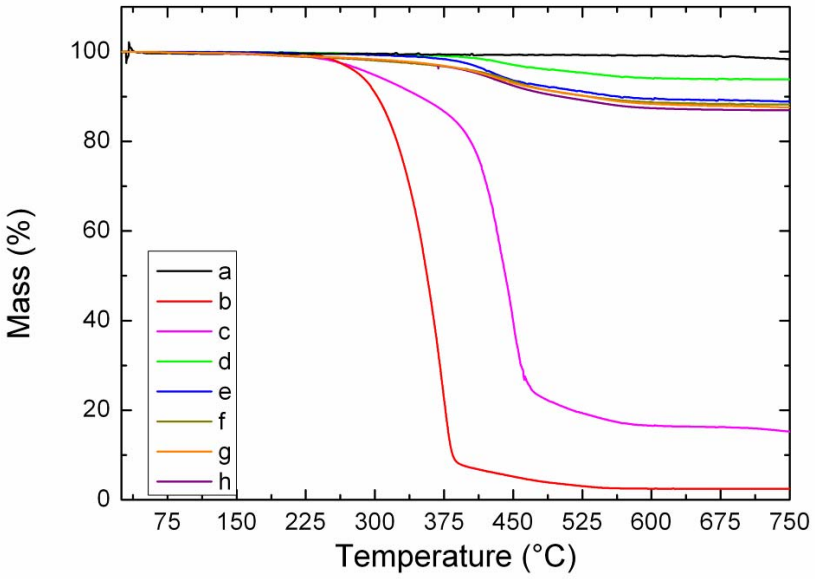


Figure 4.5: TGA thermograms of (a) MWCNTs-P (b) A*i*BP-POSS (c) PPy, and different ratios between MWCNTs and PPy respectively, (d) 1:0.2, (e) 1:0.6, (f) 1:1, (g) 1:2 and (h) 1:3.

The theoretical calculation of PPy adsorption on the surface of MWCNTs (250 $m^2/g$) was carried out by molecular modeling through measuring the surface area of pyrene and PPy. The surface area of 60 $Å^2$ as the projection of pyrene aligned to a graphene sheet was calculated using AMBER molecular mechanic approach implemented in HyperChem version 8.0.3 molecular modeling software (Hypercube Inc., Gainesville, FL, USA) (Fig. 4.6 (a)). The projection area of two possible conformations of PPy aligned to the same graphene surface was also calculated. One possible conformation can be represented as a PPy molecule laying flat on a graphene sheet (Fig. 4.6 (b)) and gives the projection area of 310 $Å^2$. Another considered conformation represents an “L-shaped” PPy molecule (Fig. 4.6 (c)) formed by bending of the flexible chain connecting the pyrene and POSS moieties. The surface area of the projection of the “L-shaped” molecule to the graphene is 227 $Å^2$. The graphene sheet consisting of 400 aromatic rings was created using HyperChem and was used for the surface area calculation, since the MWCNTs used in the current study have an average diameter of at least 12 nm which is at least six times larger than the biggest dimension of the

PPy molecule and can be approximated as a flat surface in comparison to the adsorbed molecules.

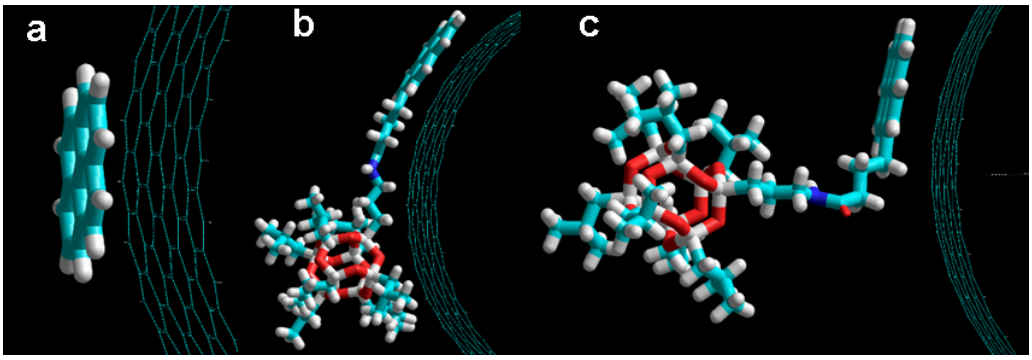


Figure 4.6: Possible confirmation of compounds immobilized on MWCNTs (a) pyrene and PPy in (b) flat and (c) “L-shaped” conformations.

The part of the MWCNTs covered by each of the modeled molecules depending on the MWCNTs/PPy ratio used for modification is presented in Table 4.1.

Table 4.1: TGA data for different ratios of MWCNTs and PPy

| MWCNTs: PPy | Mass loss (wt. %)[a)] | PPy content (mmol $g^{-1}$)[b)] | Pyrene coverage (%)[c)] | Flat PPy coverage (%) [c)] | “L-shaped” PPy coverage (%) [c)] |
|---|---|---|---|---|---|
| 1:0.2 | 5.9 | 0.066 | 9.5 | 49 | 36 |
| 1:0.6 | 10.5 | 0.125 | 18 | 93 | 68 |
| 1:1 | 11.2 | 0.134 | 19 | 100 | 73 |
| 1:2 | 11.6 | 0.140 | 20 | 105 | 76 |
| 1:3 | 12.6 | 0.154 | 22 | 115 | 84 |

a) Mass loss of PPy modified MWCNT according to TGA analysis (at 600°C).
b) Quantity of PPy immobilized on the 1g of pristine MWCNT.
c) Part of the MWCNT surface covered by immobilized compound depending on conformation.

It can be seen that the calculations done for all three molecules give very reasonable results. The most probable “L-shaped” conformation never exceeds 100 % of the covered surface and thus seems as the most probable shape of the PPy molecule adsorbed on the MWCNTs surface. The modeling results are in good agreement with the transmission electron microscopy results, distinctively showing PPy adsorbed on the surface of the MWCNTs. The adsorbed PPy

molecules on MWCNTs are highlighted by silicon mapping where white spots represent places with the highest Si concentration (Fig. 4.7 (c)).

Liu et al. functionalized MWCNTs by pyrene-PEG in water and measured the surface coverage of MWCNTs by pyrene units [21]. They analyzed the MWCNTs dispersion obtained after different cycles of dialysis by UV. After seven cycles of dialysis, the pyrene coverage value found was ~20 % which is in accordance with the value obtained for the samples functionalized at 1:1 ratio of MWCNTs and PPy respectively.

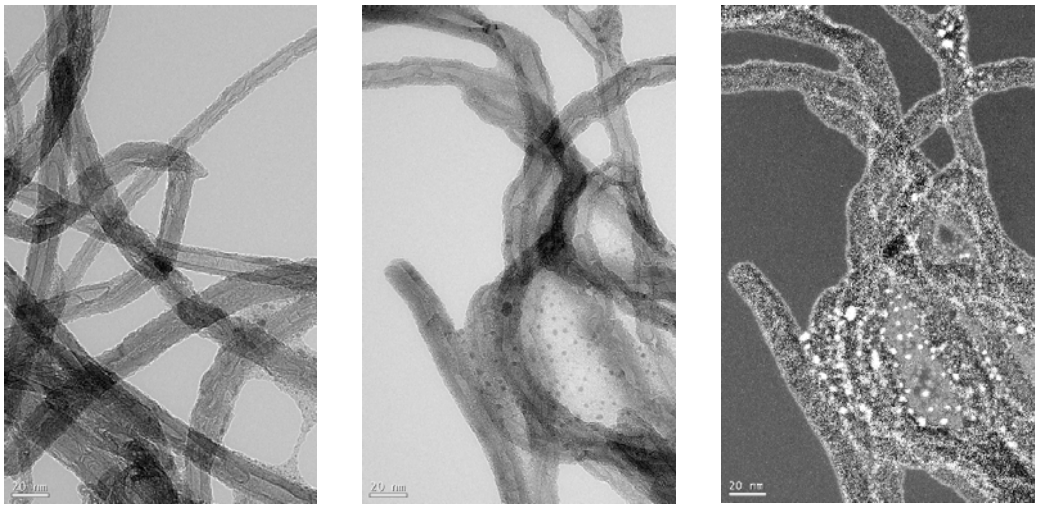


(a) (b) (c)

Figure 4.7: TEM images of (a) pristine MWCNTs, (b) PPy modified MWCNTs, (c) Silicon maping of PPy modified. White spots on (c) represent places with highest Si concentration.

### 4.2.2 Covalent Functionalization of MWCNTs

#### 4.2.2.1 Initiator Immobilization on MWCNTs

Initiator moieties were immobilized on MWCNTs-$NH_2$ by amidation reaction. Table 4.2 shows the results of initiator anchoring. An excess amount of 2-BriB was used for amidation reaction, which is much higher compared to the concentration of amine functional groups on MWCNTs-$NH_2$. The concentration of initiator (denoted by [Br] in Table 4.2) was measured by TGA where an increased

percentage mass loss was found for initiator modified MWCNTs (MWCNTs-Br) compared to MWCNTs-$NH_2$ (mass losses are summarized in Table 4.2). It is very important to clean extensively MWCNTs-Br after the reaction because the impurities or quarternary ammonium salt (a side product) may contribute to the mass loss in MWCNTs-Br measured by TGA. The reaction carried out at 300 mg (Ent. 1 and 2) scale showed nearly the same amount of initiator as on 1.2 g (Ent. 3) which shows the conversion of amine groups to amide was efficient at large scale. A fluctuation in amine group concentration was observed for MWCNTs-$NH_2$ from different batches. This fluctuation occurred due to the change in production scale, as explained by the supplier. The concentration of initiator moieties was higher in case of MWCNTs-$NH_2$ having less amine groups compared to MWCNTs-$NH_2$ containing higher concentration of amine groups. However, the initiator concentration was reproducible for MWCNTs-$NH_2$ belonging to one specific batch.

Table 4.2: Initiator immobilization reaction data.

| Ent. | Code | [$NH_2$] mmol/g | Scale (mg) | [2-BriB] mmol | [Br]* mmol/g |
|---|---|---|---|---|---|
| 1 | MWCNTsAm1 | 1.3 | 300 | 8.09 | 0.21 |
| 2 | MWCNTsAm2 | 1.3 | 300 | 8.09 | 0.21 |
| 3 | MWCNTsAm3 | 1.3 | 1200 | 32.36 | 0.19 |
| 4 | MWCNTsAm4 | 0.55 | 1200 | 32.36 | 0.48 |
| 5 | MWCNTsAm5 | 0.55 | 1200 | 32.36 | 0.46 |

* measured by TGA

Although TGA indicates the initiator immobilization on MWCNTs, however, its confirmation was done by FTIR spectroscopy. Fig. 4.8 presents the FTIR spectra of amine and initiator functionalized MWCNTs. The amine N-H bending at 1640 $cm^{-1}$ shifted to 1660 $cm^{-1}$ after the reaction which indicates the presence of amide bond. A new peak at 1760 $cm^{-1}$ indicates the carbonyl group of attached 2-BriB. The resultant initiator immobilized MWCNTs were used for grafting of polystyrene and poly(methyl methacrylate) from MWCNTs-Br via ATRP.

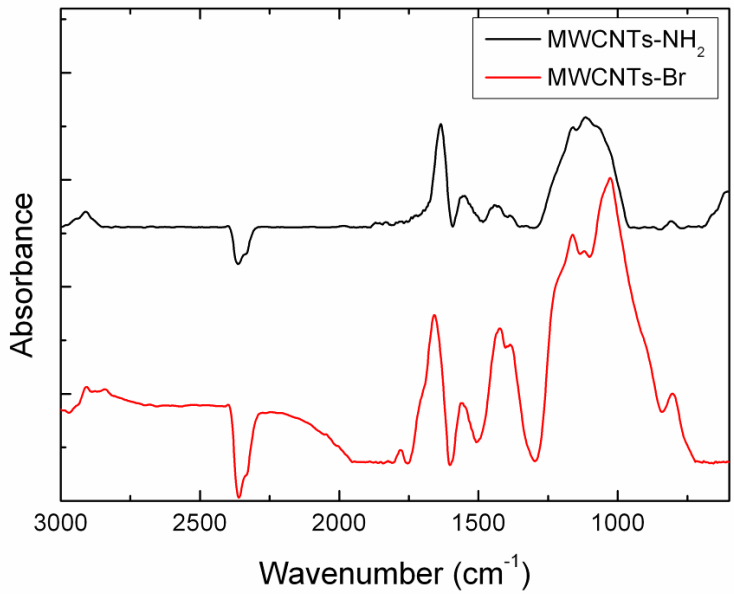


Figure 4.8: FTIR spectra of MWCNTs-$NH_2$ and MWCNTs-Br.

#### 4.2.2.2 Grafting of PMMA from MWCNTs-Br

The grafting of PMMA was carried out in the presence and absence of sacrificial initiator. The grafting reaction was carried out as a function of temperature. The polymer grafting content increased with temperature which indicates that the rate of ATRP increased with an increase in temperature (Ent. 1, Ent. 2, and Ent. 3 in Table 4.3). The temperature at 60 °C was found optimum as at 90 °C or higher temperatures the increased conversion might lead to side reactions. The reaction for the temperature studies were carried out at 100 mg scale. The polymer content decreased as the scale of the reaction was raised 5 times to the initial scale (Ent. 4). The content of polymer grafting can be increased by increasing the reaction time (Ent. 5). The polymer grafting carried out in the presence of sacrificial initiator give rise to free polymer chains in the reaction mixture. The molecular weight of free polymer is considered the same as of grafted chains. The polymer chains with narrow polydispersity were possible and it is the characteristic feature of ATRP (Ent. 6 and Ent. 7). The lower molecular weight in the case of Ent. 6 can be related to the increased initiator amount taken compared to Ent. 7. The initiator molecules might have started the growth of

more chains in case of Ent. 6 leading to the fast consumption of MMA and thus resulting in lower molecular weight of the chains. The molecular weight of polymer chains and their content on MWCNTs can be optimized varying the reaction time and [M]/[I] ratio.

Table 4.3: ATRP reaction data for PMMA grafting from MWCNTs-Br.

| Ent. | [M]/[I] | Scale (mg) | Time (h) | Temp. °C | $M_n$ Kg/mol | $M_w$ Kg/mol | PDI | Grafting (wt. %)* |
|---|---|---|---|---|---|---|---|---|
| 1 | 2700 | 100 | 1 | 40 | - | - | - | 80 |
| 2 | 2700 | 100 | 1 | 60 | - | - | - | 90 |
| 3 | 2700 | 100 | 1 | 90 | - | - | - | 94 |
| 4 | 2700 | 500 | 1 | 60 | - | - | - | 73 |
| 5 | 2700 | 500 | 2 | 60 | - | - | - | 83 |
| 6 | 500 | 1000 | 0.5 | 60 | 25.3 | 29.1 | 1.15 | 65 |
| 7 | 1000 | 1000 | 0.5 | 60 | 36.7 | 38.3 | 1.04 | 68 |

* measured by TGA

The grafting of polymer chains can be observed by FTIR spectra of the MWCNTs (Fig. 4.9). FTIR spectrum of PMMA shows C–O–C stretching at 1146 $cm^{-1}$, $–CH_3$ stretching vibration at 1440 $cm^{-1}$, C=O stretching at 1722 $cm^{-1}$, and CH stretching vibration at 2955 $cm^{-1}$. All these mentioned peaks were also observed in PMMA grafted MWCNTs which indicates the successful grafting of PMMA from MWCNTs-Br. The TEM image of MWCNTs after PMMA grafting shows a layer of polymer chains grafted from MWCNTs (Fig. 4.10 b). MWCNTs-*gf*-PMMA lead to stable dispersions in *N,N*-dimethylacetamide (DMAc), THF, and chloroform which also indicates the presence of PMMA on the MWCNTs walls. PMMA modified MWCNTs were used for PVDF MMMs, fabricated by using DMAc as solvent (Chapter 5).

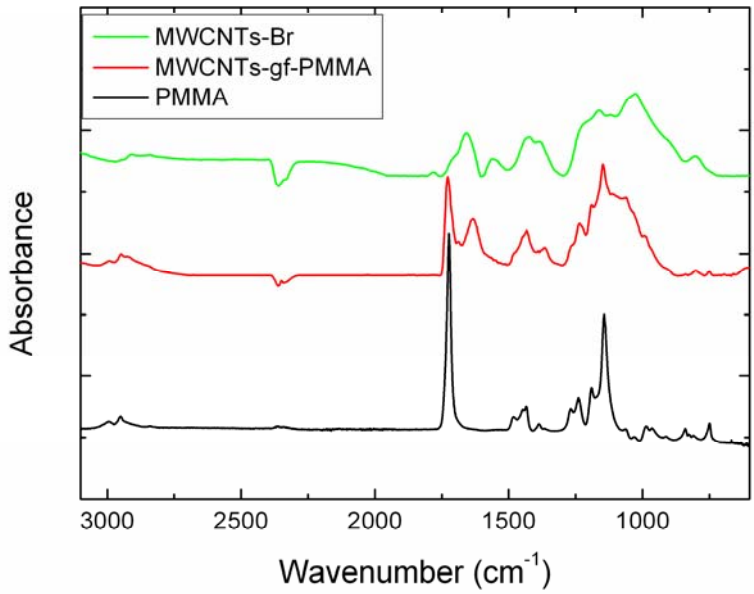


Figure 4.9: FTIR spectra of MWCNTs-Br, MWCNTs-*gf*-PMMA, and PMMA.

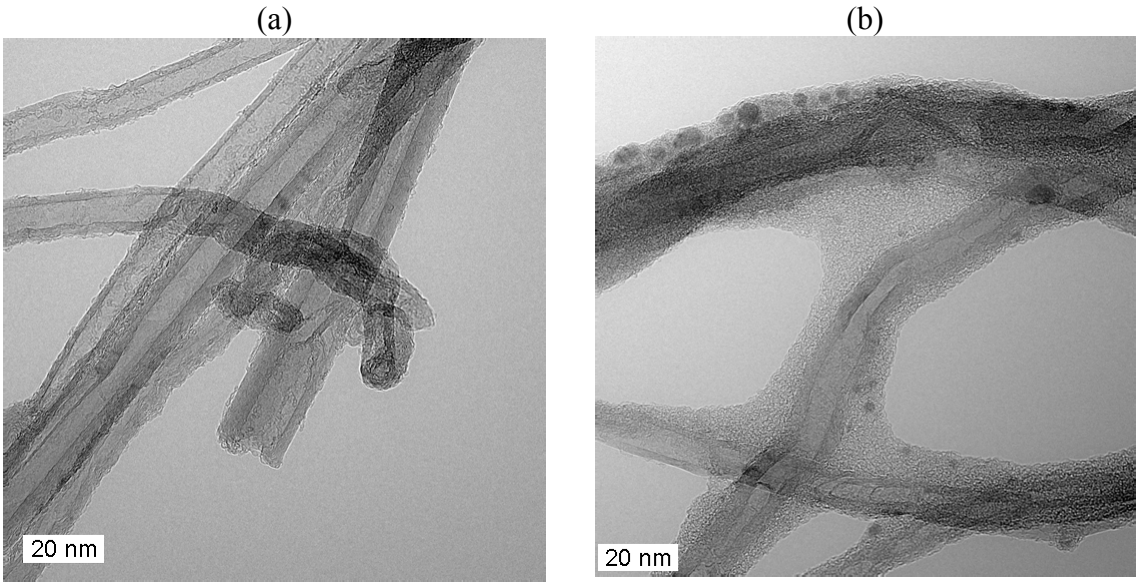


Figure 4.10: MWCNTs (a) before and (b) after PMMA grafting (PMMA content 65 wt. %).

#### 4.2.2.3 Grafting of Polystyrene from MWCNTs-Br

PS chains were grafted from MWCNTs-Br in the absence of sacrificial initiator. Two different examples of PS grafted MWCNTs are shown in Table 4.4 where

the reaction conditions were kept the same except the reaction time. The conditions of grafting reaction were followed from the optimized condition for PS [22]. The increase in polymer content was observed as a function of time which indicates that the monomer conversion increased with time. The content of PS on MWCNTs was measured by TGA where increased percentage mass loss was observed for PS grafted MWCNTs. FTIR analysis also indicates the presence of PS chains on MWCNTs (Fig. 4.11). MWCNTs-*gf*-PS showed the signal relating PS at 3019 $cm^{-1}$ for =C–H stretching vibration, at 2911 $cm^{-1}$ for $–CH_2–$ stretching vibration, at 1590 $cm^{-1}$ for C=C stretching vibration of aromatic carbons, at 747 $cm^{-1}$ for –C–H out of plane deformation vibration, and at 691$cm^{-1}$ for ring out of plane deformation vibration. At low grafting of PS the signals related to PS were not clearly identified but at higher grafting content the PS signals were very prominent. The grafting of PS on MWCNTs at low grafting content can be observed in Fig. 4.12 after ATRP. The layer of polymer chains on MWCNT-PS indicates the successful grafting of polymer chains. PS modification of MWCNTs led to their stable dispersion in chloroform, THF, and toluene. In the present study MWCNTs-*gf*-PS were prepared for poly(dimethylsiloxane) (PDMS) mixed matrix composite membranes (MMCMs), fabricated using toluene as solvent, by solvent evaporation method. Stable dispersion of MWCNTs-*gf*-PS in toluene has an influence on the final dispersion of MWCNTs in PDMS MMCMs which is discussed in chapter 7.

Table 4.4: Data of PS grafting from MWCNTs-Br

| Ent. | [M]/[I] | Scale (g) | Time (h) | Temp. (°C) | Grafting (wt. %)* |
|---|---|---|---|---|---|
| 1 | 3000 | 1 | 2 | 90 | 40 |
| 2 | 3000 | 1 | 24 | 90 | 90 |

* measured by TGA

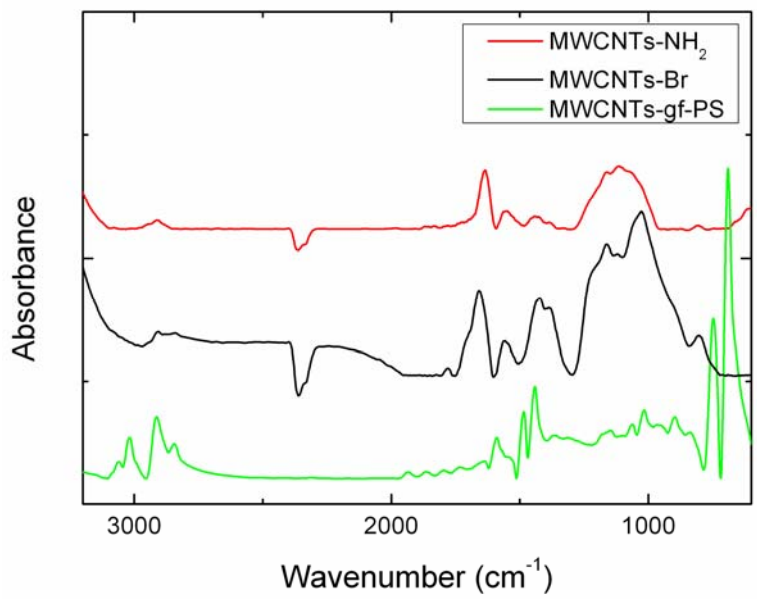


Figure 4.11: FTIR spectra of MWCNTs-$NH_2$, MWCNTs-Br, and MWCNTs-*gf*-PS.

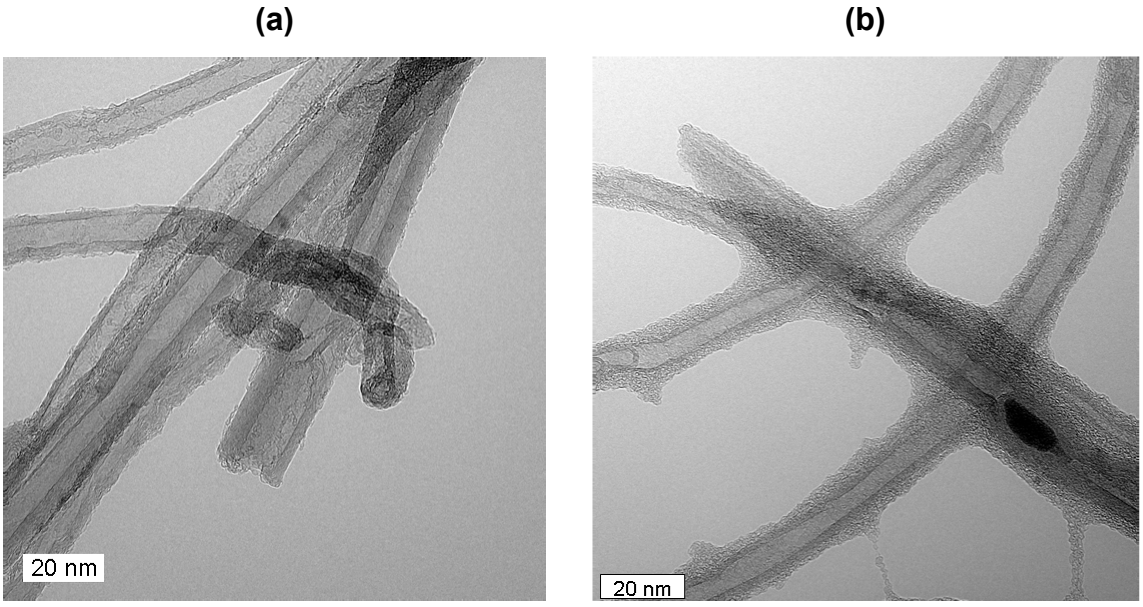


Figure 4.12: TEM images (a) before PS grafting and (b) after PS grafting (PS content 40 wt. %).

### 4.2.3 Functionalization of MWCNTs via "Grafting Onto" Method

The alkoxyamine end capped PMMA (PMMA-$ONR_2$) was prepared by nitroxide mediated polymerization (NMP). PMMA-$ONR_2$ generated PMMA macroradicals

through cleavage of C-O bond of alkoxyamine upon heating at 50 °C in the reaction mixture containing MWCNTs. The number average molecular weight of PMMA-$ONR_2$ was 26 Kg/mol and a polydispersity of 1.3. The successful grafting of PMMA onto MWCNTs was revealed by TGA where an increased percentage mass loss was observed in the case of PMMA grafted MWCNTs. The content of PMMA grafted onto MWCNTs was 7 wt. %.

## 4.3 Conclusions

Surface functionalization of MWCNTs was carried out by covalent and non-covalent means. Pyrene-POSS (PPy) was used as dispersant for non-covalent functionalization of MWCNTs. PPy was prepared by amidation reaction between aminopropylisobutyl POSS and 1-pyrenebutyric acid. Proton NMR and FTIR spectroscopy indicated successful synthesis of PPy. It proved to be a very good dispersant molecule as it gave rise to the stable dispersion of MWCNTs in solvents of different polarities i.e., THF, *n*-hexane, toluene, and chloroform. The stable dispersion of MWCNTs in these solvents also indicates the successful synthesis of PPy because the educts of the reaction led to an unstably dispersed system. TGA was used to determine the degree of adsorption of PPy. Analysis of adsorbed conformations of PPy was performed combining TGA and modeling results. The L-shaped conformation seemed to be the reasonable conformation adsorbed on the MWCNTs surface. TEM images of modified MWCNTs also indicated the adsorption of PPy where the silicone mapping showed the presence of PPy.

The covalent functionalization was carried out by incorporating polymer chains via “grafting from” and “grafting onto” techniques. An amidation reaction was used to immobilize ATRP initiator on amine functionalized MWCNTs. PMMA and PS were grafted from the initiator moieties present on MWCNTs. The successful grafting of PS and PMMA was evident from TGA, FTIR, and TEM analyses. Modification of MWCNTs by PMMA via “grafting onto” technique was confirmed

by TGA analysis and polymer chain length was measured by gel permeation chromatography (GPC).

## 4.4 References

[1] T. Ebbesen, H. Lezec, H. Hiura, J. Bennett, H. Ghaemi, T. Thio, Nature, 382 (1996) 54-56.
[2] J. P. Salvetat, A. J. Kulik, J. M. Bonard, G. a. D. Briggs, T. Stöckli, K. Méténier, S. Bonnamy, F. Béguin, N. A. Burnham, L. Forró, Adv. Mater., 11 (1999) 161-165.
[3] A. A. Balandin, Nature Mat., 10 (2011) 569-581.
[4] M. Moniruzzaman, K. I. Winey, Macromolecules, 39 (2006) 5194-5205.
[5] P. Pötschke, S. Pegel, M. Claes, D. Bonduel, Macromol. Rap. Commun., 29 (2008) 244-251.
[6] J. N. Coleman, U. Khan, Y. K. Gun'ko, Adv. Mater., 18 (2006) 689-706.
[7] T. Morishita, M. Matsushita, Y. Katagiri, K. Fukumori, Carbon, 47 (2009) 2716-2726.
[8] J. Hwang, J. Jang, K. Hong, K. N. Kim, J. H. Han, K. Shin, C. E. Park, Carbon, 49 (2011) 106-110.
[9] Y. Ji, Y. Y. Huang, A. R. Tajbakhsh, E. M. Terentjev, Langmuir, 25 (2009) 12325-12331.
[10] T. Morishita, M. Matsushita, Y. Katagiri, K. Fukumori, Carbon, 48 (2010) 2308-2316.
[11] D. Tasis, N. Tagmatarchis, A. Bianco, M. Prato, Chem. Rev., 106 (2006) 1105-1136.
[12] T. Fujigaya, N. Nakashima, Polym. J., 40 (2008) 577-589.
[13] J. Zou, L. Liu, H. Chen, S. I. Khondaker, R. D. Mccullough, Q. Huo, L. Zhai, Adv. Mater., 20 (2008) 2055-2060.
[14] J. Zou, S. I. Khondaker, Q. Huo, L. Zhai, Adv. Funct. Mater., 19 (2009) 479-483.
[15] S. W. Kim, T. Kim, Y. S. Kim, H. S. Choi, H. J. Lim, S. J. Yang, C. R. Park, Carbon, 50 (2012) 3-33.
[16] D. Neumann, M. Fisher, L. Tran, J. G. Matisons, J. Am. Chem. Soc., 124 (2002) 13998-13999.
[17] G. Li, L. Wang, H. Ni, C. U. Pittman, J. Inorg. Organometallic Polym., 11 (2001) 123-154.
[18] B. Zhang, Y. Chen, J. Wang, W. J. Blau, X. Zhuang, N. He, Carbon, 48 (2010) 1738-1742.
[19] P. B. Erno Pretsch, Martin Badertscher, Structural Determination of Organic Compounds. Fourth Edition: Springer 2009.
[20] http://www.Science-and-Fun.De/Tools/.
[21] J. Liu, O. Bibari, P. Mailley, J. Dijon, E. Rouvière, F. Sauter-Starace, P. Caillat, F. Vinet, G. Marchand, New J. Chem., 33 (2009) 1017-1024.
[22] J. Albuerne, A. Boschetti-de-Fierro, V. Abetz, J. Polym. Sci. Part B: Polym. Phy., 48 (2010) 1035-1046.

# Chapter 5. Poly(vinylidene fluoride) (PVDF) Mixed Matrix Membranes (MMMs)

## 5.1 Introduction

Porous polymer membranes are important class of membranes used in microfiltration, ultrafiltration, dialysis, reverse osmosis, and gas separation etc. [1-3]. They are prepared by different processes like cintering, track etching, stretching, template leaching, and phase inversion etc. [4]. However, the phase inversion process is the most commonly used method for the fabrication of porous membranes. Porous membranes for gas separation and reverse osmosis have also been reported by the phase inversion method where a thin layer, integrated with a porous support, involves in filtration or separation [5, 6]. Porous membranes have also been widely used as the porous support for the composite membranes where a thin dense selective layer is cast on a porous membrane support [7-9]. The porous membrane support provides the mechanical stability to the thin selective layer. The mechanical stability of the porous membranes is of prime importance for a better separation performance of the composite membranes. At high transmembrane pressures the porous structure of the membranes undergoes compaction leading to decline in flux of the membranes [10].

A very promising approach to improve the mechanical stability of the porous membranes is to use the organic-inorganic blends for the fabrication of membranes. Introduction of an inorganic phase in the form of nanofillers increases the mechanical stability where interactions between polymer and inorganic phase improve the mechanical stability of the membranes by transferring the load from polymer matrix to the filler. This class of membranes with nano sized fillers has been termed as the mixed matrix membranes (MMMs) [11]. Ebert et al. blended $TiO_2$ nanoparticles in PVDF to prepare the MMMs by a phase inversion process. The porous membranes were tested for high pressure

applications. Membranes loaded with 40 wt. % $TiO_2$ nanoparticles showed better mechanical stability compared to pure PVDF membranes [12].

Carbon nanotubes (CNTs) possess extraordinary mechanical and electrical properties [13, 14]. During past years, they have been extensively researched as fillers for composite materials. Owing to their excellent flux properties, they were used by various research groups in porous polymeric membranes [15]. Wu and Qiu et al. reported the improved separation performance of the porous membranes by incorporating CNTs in membrane materials [16, 17]. In this study, multi-walled carbon nanotubes (MWCNTs) were blended with PVDF to fabricate ultrafiltration MMMs by a phase inversion process. The aim to introduce MWCNTs in PVDF matrix system was to improve separation performance, electrical conductivity, and mechanical stability of the conventional membranes. Pure and surface functionalized MWCNTs were used for the fabrication of the membranes. The functionalized MWCNTs include hydroxyl (-OH) and poly(methyl methacrylate) (PMMA) modified tubes. MWCNTs were modified with PMMA by “grafting from” (MWCNTs-*gf*-PMMA) and “grafting to” (MWCNTs-*gt*-PMMA) techniques. PMMA modified MWCNTs were selected because of the miscibility of PVDF with PMMA [18]. The improved miscibility of the filler in the polymer matrix might improve the mechanical stability of the membranes.

## 5.2 Results and Discussion

Purified (MWCNT-P), hydroxyl (MWCNTs-OH), and PMMA modified (MWCNTs-*gf*-PMMA and MWCNTs-*gt*-PMMA) MWCNTs were used for the fabrication of MMMs. MWCNTs-OH contained 0.77 mmol/g of –OH groups, MWCNTs-*gf*-PMMA contained 65 wt. % PMMA with $M_n$ of 25.3 Kg/mol and PDI of 1.15, and MWCNTs-*gt*-PMMA contained 7 wt. % of PMMA chains with $M_n$ of 26 Kg/mol and PDI value of 1.3.

### 5.2.1 Viscosity of the Polymer Solutions

The PVDF MMMs, prepared in this study, contained effective loading of 2 wt. % MWCNTs. The membranes loaded with MWCNTs-P, MWCNTs-OH, MWCNTs-*gt*-PMMA, and MWCNTs-*gf*-PMMA are denoted by PVDF-P, PVDF-OH, PVDF-PMMAGTO, and PVDF-PMMAGF, respectively. The viscosity measurements were carried out at a shear rate of 500 $s^{-1}$. The viscosity of the PVDF solution increased with the inclusion of MWCNTs (Table 5.1). MWCNTs-P, MWCNTs-OH, and MWCNTs-*gt*-PMMA showed the solution viscosity of nearly same magnitude. The increase in polymer solution viscosity with the addition of MWCNTs has been related with good interaction of MWCNTs with polymer chains [19, 20]. The interactions between MWCNTs and polymer chains become prominent compared to MWCNTs-MWCNTs interactions. In the case of solutions containing MWCNTs-*gf*-PMMA, the viscosity of the solution decreased. The decrease in polymer solution viscosity in MWCNTs-*gf*-PMMA solution compared to solutions containing MWCNTs-P, MWCNTs-OH, and MWCNTs-*gt*-PMMA can be related to the presence of big agglomerates or particulates of MWCNTs. The bundles of MWCNTs-*gf*-PMMA, visible in optical micrographs (Fig. 5.1 (d)), might arise by polymerization taken place on agglomerates leading to tight bundles of MWCNTs. Exfoliated or loose bundles of MWCNTs are quite visible in the case of MWCNTs-P, MWCNTs-OH, and MWCNTs-*gt*-PMMA incorporated PVDF membranes (Fig. 5.1 (a-c)). A depression in viscosity of the reaction mixture of MWCNTs and poly(ethylene glycol) has been reported in literature where the decrease in viscosity of the mixture was related to the reaction taken place on MWCNTs bundles rather than on individual tubes [21]. Since MWCNTs-OH were produced by a special air oxidation method and MWCNTs-*gt*-PMMA were prepared by PMMA radical addition to MWCNTs, hence MWCNTs might have functionalities only on tubes rather than on bundles. This hypothesis explains the presence of exfoliated or loose aggregates of MWCNTs in these cases. The viscosity of polymer solution plays an important role in membranes prepared by the phase inversion method. The increase in viscosity of the polymer solution

slows down the phase inversion phenomenon and leads to a membrane with low porosity.

Table 5.1: Viscosity data of PVDF solutions loaded with 2 wt. % of MWCNTs with different functional groups

| Code | Viscosity (Pa.s) |
|---|---|
| PVDF | 2.43 |
| PVDF-P | 3.0 |
| PVDF-OH | 2.93 |
| PVDF-PMMAGTO | 2.90 |
| PVDF-PMMAGF | 2.46 |

### 5.2.2 Optical Microscope Characterization

The state of dispersion of MWCNTs with different functional groups can be observed in Fig 5.1. MWCNTs showed better dispersion in PVDF-OH and PVDF-PMMAGTO membranes compared to PVDF-P and PVDF-PMMAGF. PVDF-P membranes showed the presence of MWCNTs particulates or aggregates. MWCNTs-P are held together by van-der-Waals and $\pi$-$\pi$ stacking interactions leading to the formation of aggregates. Surface functionalization of MWCNTs reduces the extent of these interactions resulting in better dispersed MWCNTs compared to MWCNTs-P [22]. The functional groups like OH and PMMA might have reduced the intertube interaction and thus lead to a better dispersed system where no or less particulate structures are visible. Although the effective loading of MWCNTs is 2 wt. % in the shown optical images, but the color of the resulting PVDF membrane was the darkest in the case of PVDF-P membranes. The same trend was observed by visual observation of the membranes. The reason for the light color could be the better miscibility of functionalized MWCNTs in the PVDF matrix. In the case of PVDF-PMMAGF membranes, big MWCNTs agglomerates can be observed from the optical images (Fig. 5.1 (d)). In these membranes the presence of these particulates can be related to the polymer grafting reaction. During the functionalization of MWCNTs by the *grafting from* method, the ATRP reaction might have started from the MWCNTs aggregates present in the

reaction mixture leading to tighter MWCNTs bundle coated with polymer. These kinds of MWCNTs were still present even after the vigorous sonication process. One possibility to get rid of these aggregates during solution preparation is the slight centrifugation which may settle the big particulates at the bottom of the centrifuge tube. The drawback of this technique is that the separated aggregates will reduce the effective loading of MWCNTs in the resultant MMMs.

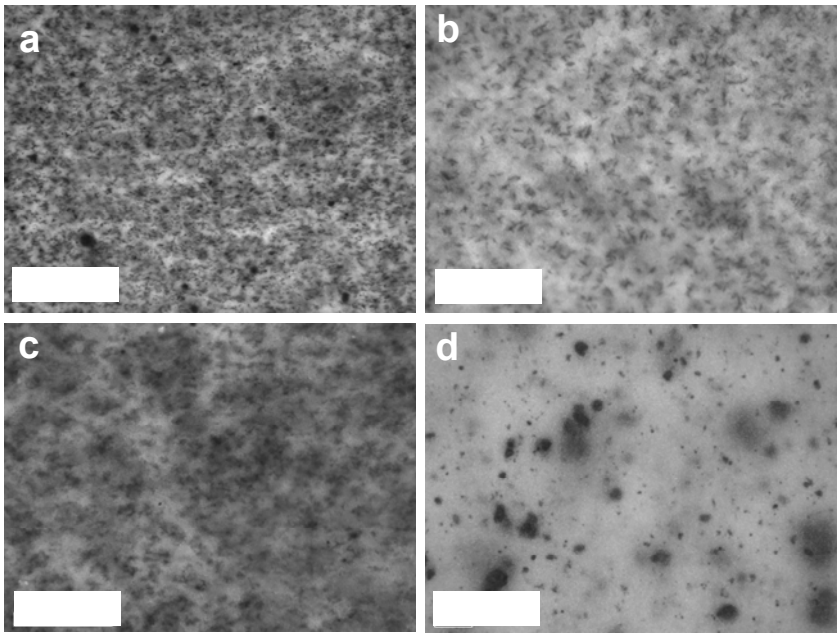


Figure 5.1: Optical micrographs of PVDF MMMs (a) PVDF-P, (b) PVDF-OH, (c) PVDF-PMMAGTO, and (d) PVDF-PMMAGF. Scale bar 50 μm.

The method of preparation of polymer solution played an important role in MWCNTs dispersibility in the membranes. Initially, the solutions were prepared by dispersing MWCNTs in *N,N*-dimethylacetamide (DMAc) using sonication followed by addition of polymer to the mixture and stirring with magnetic stirrer to dissolve the polymer. The membranes prepared by this way showed big MWCNTs agglomerates in all types of studied MWCNTs. Fig. 5.2 (a) shows an example of PVDF-P prepared by this method. Calendaring is another way to process the polymer solution for exfoliating or demolishing MWCNTs aggregates. During calendaring solvent evaporation took place resulting in a paste-like material. The loss of polymer solution composition and possibility of initiation of phase separation phenomenon, as the solution was processed in open

environment, were big hurdles to handle the polymer solution by calendaring. The most effective preparation of the polymer solution, with well dispersed MWCNTs, was carried out by simultaneous sonication and mechanically stirring the solution. The improvement in dispersion of MWCNTs was observed by SEM images where the presence of bigger MWCNTs agglomerates was not found (Fig. 5.2 (b-c)). MWCNTs-*gt*-PMMA showed better dispersion compared to MWCNTs-P where homogenously dispersed MWCNTs in PVDF-PMMAGTO indicate the effectivity of functionalization of MWCNTs. Fig. 5.2 (d) shows the PVDF-PMMAGF after following the simultaneous stirring and sonication procedure. The presence of MWCNTs agglomerates were observed even after vigorous solution preparation which indicates their rigidity.

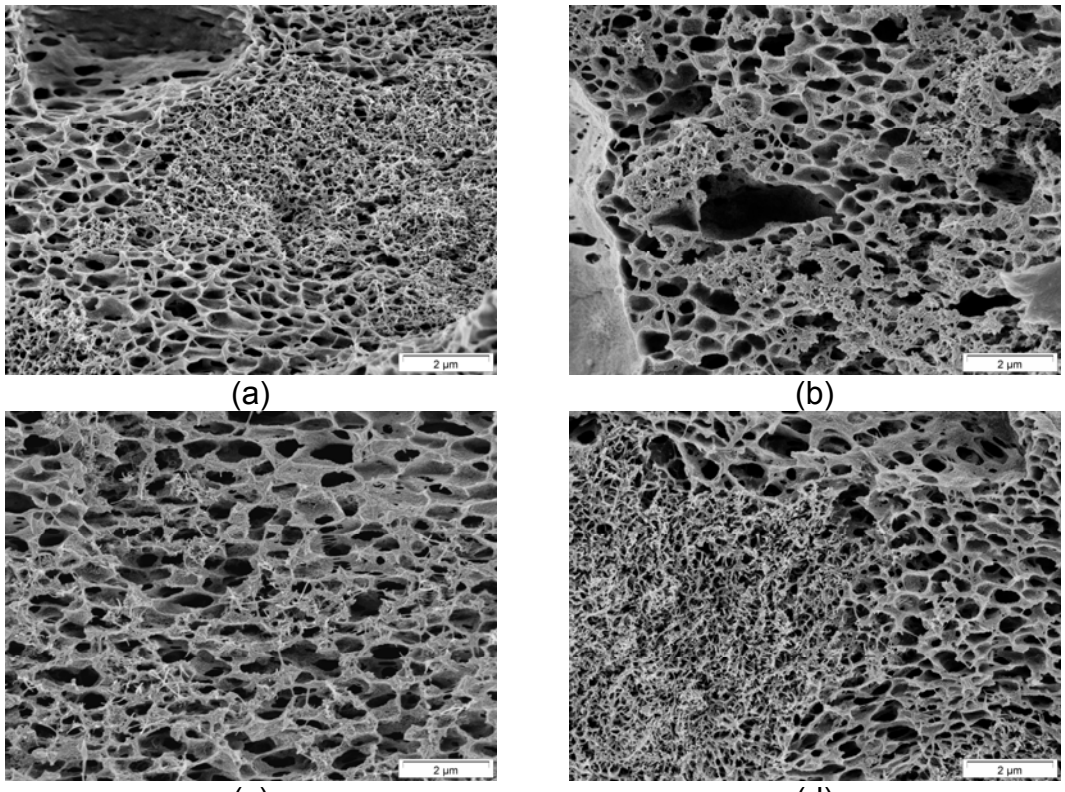


Figure 5.2: SEM cross-section images of PVDF MMMs containing 2 wt. % MWCNTs (a) PVDF-P, (b) PVDF-P, (c) PVDF-PMMAGTO, and (d) PVDF-PMMAGF. In membrane (a) MWCNTs were dispersed by bath sonication and simple magnetic stirring. In membranes (b-d) the dispersion of MWCNTs was carried out by combined sonication and mechanical stirring.

### 5.2.3 Elelctrical Sheet Resistance

The electrical sheet resistance of PVDF MMMs is shown in Fig. 5.3. The electrical sheet resistance of PVDF-P is least indicating its highest electrical surface conductivity. The intrinsic properties of tubular structure of MWCNTs-P seem to be well maintained which could be the reason for the lowest resistivity values compared to functionalized MWCNTs at the same loading i.e., 2 wt. %. For PVDF-OH, the sheet resistance is higher compared to PVDF-P. The increase in sheet resistance may be attributed to the introduction of side wall defects on MWCNTs. During the covalent functionalization of MWCNTs the hybridization of carbon atoms changes from $sp^2$ to $sp^3$ which might be the reason of higher resistivity for the case of PVDF-OH [22]. The state of dispersion of MWCNTs in PVDF-OH was better compared to PVDF-P (Fig. 5.1) and for better state of dispersion of MWCNTs, lower amount of MWCNTs are required to reach the percolation threshold. However, at an equal loading of 2 wt. %, PVDF-OH showed higher resistivity compared to PVDF-P which is purely due to the side wall structural defects of MWCNTs. Sulong et al. reported the effect of functionalization on the electrical conductivity of the epoxy nanocomposites [23]. They showed that the nanocomposites containing purified MWCNTs exhibited higher electrical conductivity values compared to nanocomposites containing chemically functionalized MWCNTs. The state of dispersion of functionalized MWCNTs in epoxy matrix was better than purified MWCNTs, however, the decrease in electrical conductivity was linked to the introduction of MWCNTs defects during the harsh reaction conditions.

Figure 5.3 also presents the sheet resistance of PVDF-PMMAGF and PVDF-PMMAGTO membranes. PVDF-PMMAGF membranes did not show electrical conductivity as they had electrical sheet resistance which was not in the instrument measurement range and indicates their insulation behavior. The absence of surface electrical conductivity can be related to the insulating effect of polymer chains grafted from MWCNTs (Fig. 4.10 (b), chapter 4). Surface of MWCNTs is shielded with PMMA and hence results in a non-conductive system.

The aggregation of MWCNTs in PVDF-PMMAGF leads to a system where MWCNTs lack the sufficient contact points which results in a non-conductive system. PVDF-PMMAGTO showed higher surface electrical conductivity compared to PVDF-PMMAGF which is due to the low content and grafting density of PMMA on MWCNTs-*gt*-PMMA compared to MWCNTs-*gf*-PMMA. In the case of PVDF-PMMAGTO, the sheet resistance was higher compared to PVDF-OH. The higher surface resistivity in case of PVDF-PMMAGTO compared to PVDF-OH and PVDF-P is because of the combination of shielding effect of PMMA chains and surface defects on MWCNTs generated during the functionalization.

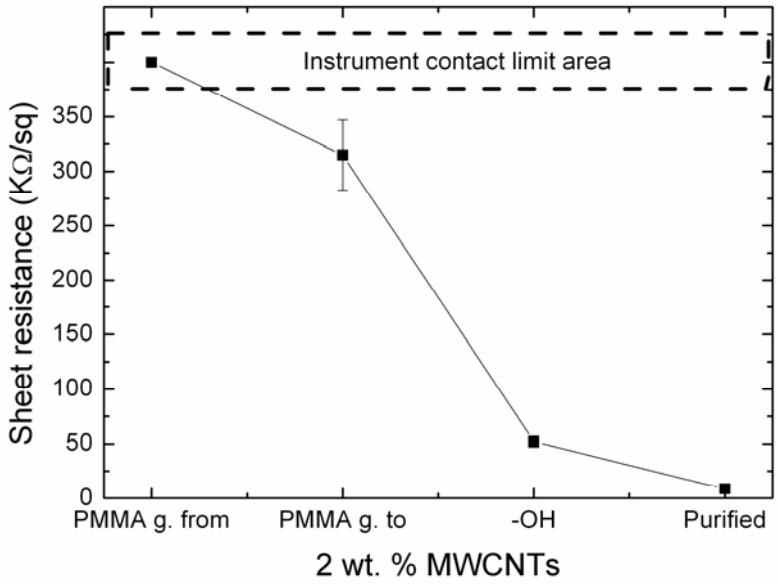


Figure 5.3: Electrical sheet resistance of PVDF MMMs at 2 wt. % loading of MWCNTs bearing different functional groups.

### 5.2.4 Membrane Morphology

Fig. 5.4 shows the surface morphology of the PVDF MMMs. The surface pore size seems to increase with the addition of MWCNTs. In PVDF-P membranes (Fig. 5.4 (b)), the number of relatively larger surface pores increased but overall pore density decreased compared to pure PVDF membranes (Fig. 5.4 (a)). In PVDF-OH membranes (Fig. 5.4 (c)), more interconnected pores were found and pore density was higher compared to PVDF-P membranes (Fig. 5.4 (b)). PVDF-

PMMAGTO and PVDF-PMMAGF membranes (Fig. 5.4 (d-e)) showed biggest surface pores especially PVDF-PMMAGTO membranes. The prominent increase in surface pore size in the case of functionalized MWCNTs incorporated membranes might be due to the presence of functional polymer (PMMA) and hydroxyl groups. Choi et al. blended carboxyl functionalized MWCNTs (MWCNTs-COOH) with polysulfone to prepare the membranes by phase inversion process [19]. They observed an increase in surface pore size with increase in MWCNTs-COOH loading upto 1.5 wt. % compared to pure membranes. The viscosity of the polymer solutions increased with MWCNTs-COOH addition and above 1.5 wt. % loading of MWCNTs-COOH, the decrease in surface pore size was related to slow phase separation. In spite of increasing the viscosity of the solution, the increase in surface pore size was related to increased phase inversion due to the presence of functional groups on MWCNTs by Celik et al. [24].

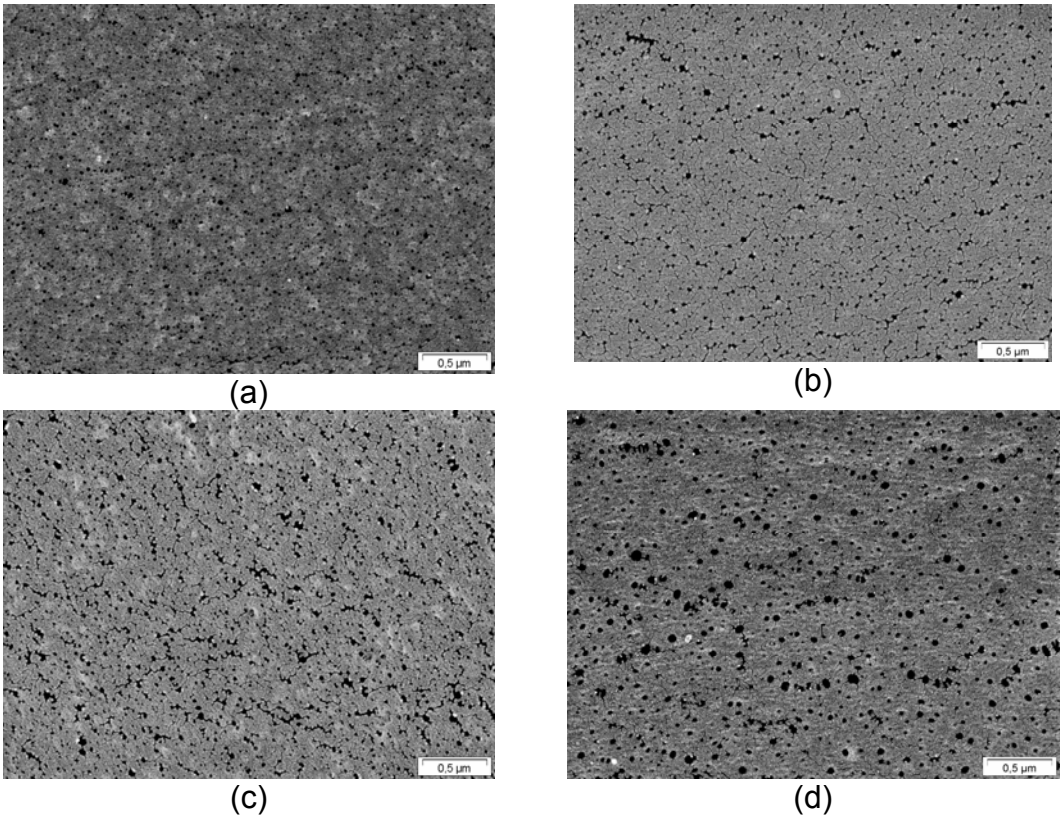


*Figure 5.4 continued*

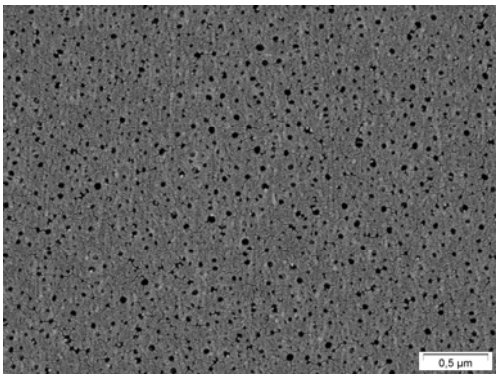


(e)

Figure 5.4: SEM surface images of PVDF MMMs containing 2 wt. % MWCNTs (a) pure PVDF (b) PVDF-P, (c) PVDF-OH, (d) PVDF-PMMAGTO, and (e) PVDF-PMMAGF.

The cross-section morphology of PVDF MMMs can be observed in Figure 5.5. The long range macrovoidic cavities were observed in the case of pure PVDF membranes (Fig. 5.5 (a)). The macrovoids represent the part of the polymer solution which is relatively poor in polymer or rich in solvent [4]. The decrease in the population of macrovoids was observed with the addition of MWCNTs especially in a region of 5 µm from the top. With the addition of MWCNTs the thin long ranged macrovoidic structures turned into relatively broader and shorter ranged macrovoids (Fig. 5.5 (b-d)). The decrease in the macropores is due to an increase in the viscosity of the polymer solution which delays phase inversion phenomenon [24]. The difference in thickness of samples shown in Fig. 5.5 might result from the penetration of the solution into nonwoven polyester. PVDF-PMMAGF (Fig. 5.5 (e)) showed long range macrovoids like pure PVDF membranes, which is due to low viscosity of the polymer solution compared to MWCNTs-P, MWCNTs-OH and MWCNTs-*gt*-PMMA containing solutions.

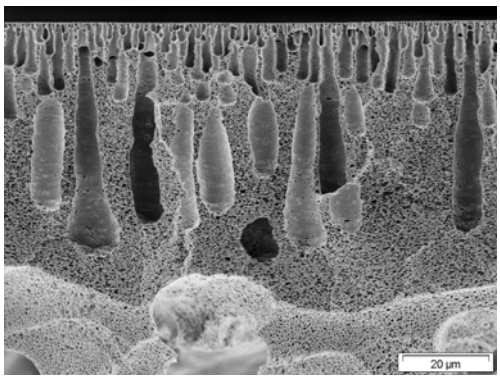


(a)

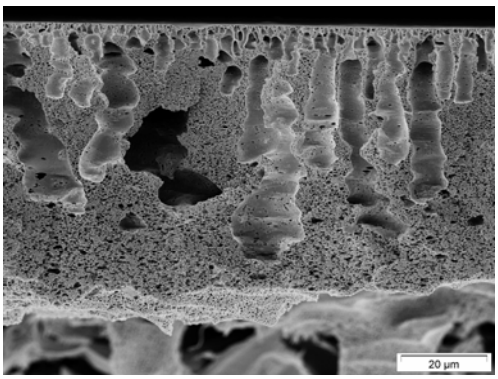


(b)

*Figure 5.5 continued*

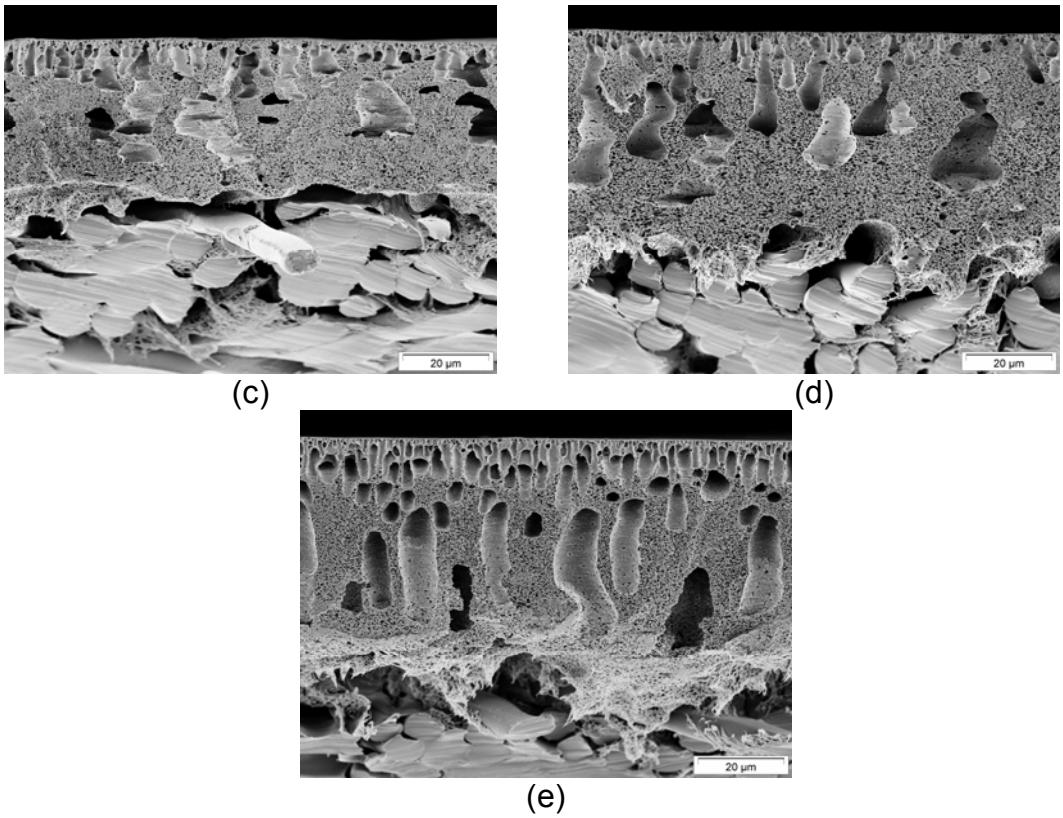


(c) (d)

(e)

Figure 5.5: SEM cross-section images of PVDF MMMs containing 2 wt. % MWCNTs (a) pure PVDF (b) PVDF-P, (c) PVDF-OH, (d) PVDF-PMMAGTO, and (e) PVDF-PMMAGF.

### 5.2.5 Surface Pore Size Analysis

The surface pore size analysis was carried out by capillary pore flow meter. The membrane stamps were cut into a diameter of 2.5 cm followed by dipping the stamp in a special liquid of known surface tension (Porewick). Nitrogen gas was kept flowing with gradually increased pressure. The pressure at which the liquid comes out of the first membrane pore is known as the bubble point. The pore diameter can be calculated by eq. 5.1 [4, 5]:

$$D = \frac{4\sigma \cos\theta}{p} \qquad 5.1$$

where ‘D’ is the pore diameter, ‘σ’ is the surface tension of the liquid used, ‘θ’ is the contact angle of the liquid, and ‘p’ is the applied pressure. One advantage of

using this method over SEM analysis is that it gives overall information of the membrane surface pores present in a range of effective 2 cm diameter. Capillary pore meter results, summarized in Table 5.2, also indicated the increased surface pore size with the addition of MWCNTs in PVDF. The bubble point increased with MWCNTs addition, especially prominent in case of PVDF-P and PVDF-PMMAGTO membranes. The mean pore size also increased in case of MMMs where the highest mean pore size was found in PVDF-PMMAGTO membranes. The trend of pore size measurement by poremeter is in agreement with SEM images.

Table 5.2: pore size and contact angle measurement data of PVDF MMMs.

| Code | Bubble point (μm) | Mean pore diameter (μm) | Contact angle (°) |
|---|---|---|---|
| Pure PVDF | 0.150 (±0.03) | 0.067 (±0.005) | 76 (±6) |
| PVDF-P | 0.29 (±0.07) | 0.088 (±0.008) | 75 (±8) |
| PVDF-OH | 0.22 (±0.05) | 0.087 (±0.007) | 73 (±5) |
| PVDF-PMMAGF | 0.19 (±0.07) | 0.091 (±0.008) | 71 (±6) |
| PVDF-PMMAGTO | 0.26 (±0.09) | 0.093 (±0.008) | 74 (±5) |

### 5.2.6 Membrane Separation Performance

The trend of water permeance of PVDF MMMs, as a function of time, can be observed in Fig. 5.6. At the start of filtration, the water permeance of PVDF-PMMAGF membranes were the highest followed by PVDF-PMMAGTO membranes. As the contact angle of the membranes did not change significantly after the addition of MWCNTs (Table 5.2), the bigger surface pores were mainly responsible for higher water permeance at the start of the filtration in MMMs compared to pure PVDF membranes. After 3 hours of water permeance through the PVDF membranes it can be seen that there was a slight improvement in the water permenace values of the membranes containing MWCNTs with different chemical functional groups. The decrease in water permeance with time took place due to two main factors. The first factor is the conditioning agent which loses its impact on porous membranes with time. Isopropanol/water mixture (1:1 by v/v) was used as conditioning agent. The membrane stamps were dipped in

this mixture for one minute to open the membrane pores. Without using this conditioning agent, no or very low flux was observed in PVDF membranes. The compaction of the membrane porous structure can be the second factor influencing the decrease of water permeance with time. At a fixed transmembrane pressure of 2 bars the porous structure might have compacted gradually with time. After 3 hours of filtration the water permeance became constant. After the measurement of water permeance, the membranes were taken out of the membrane cell and were put again into the cell for measurement. The values of water permeance were higher compared to the values measured just before the relaxation of the membrane. The initial values of the membranes were recovered by dipping the membranes in water/isopropanol mixture. This trend indicates that the decrease in water permeance with time is due to the combined effect of lost conditioning agent and residual stresses which lead to the compaction of the membranes. However, this can be regarded as the reversible compaction as the initial water permeance values were obtained by relaxing and conditioning the PVDF membranes.

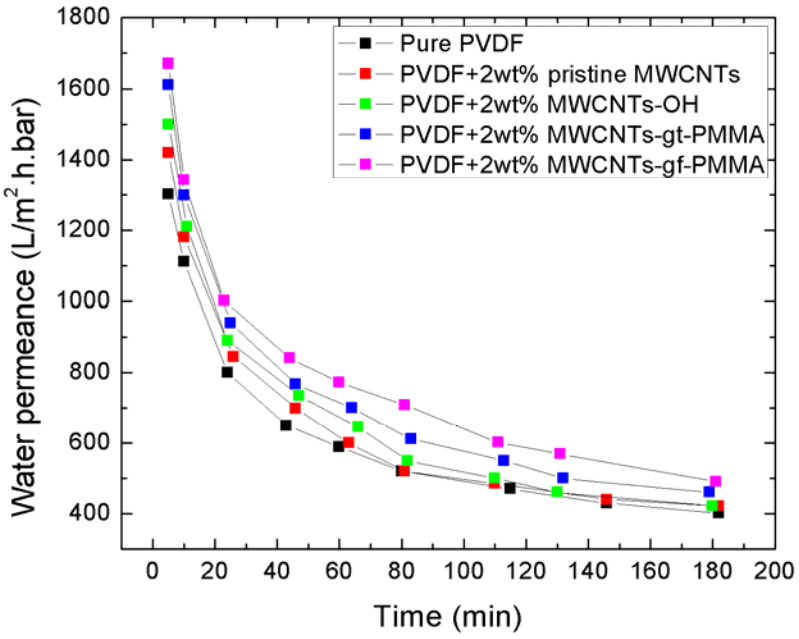


Figure 5.6: Water permeance of PVDF MMMs as a function of time.

Dextrans (MW: 350-550 Kg/mol), globular proteins (bovine serum albumin (BSA), MW: 66 Kg/mol), and polystyrene nanoparticles (mean size 50 nm) were used for separation characterization of the membranes. Very low retention (<10 %) of dextrans and bovine serum albumin was observed in the studied MMMs with no specific trend with respect to the type of MWCNTs. The lower retention of BSA and dextran might be due to their smaller size or smaller radius of gyration of the chains compared to membrane surface pores, making the possibility of their permeance through the membranes. PS nanoparticles were rejected 100 % by all the membranes. The turbid PS nanoparticle suspension was filtered through the membranes giving rise to the transparent solvent (water). The transparent liquid was analyzed by particle size analyzer where no PS particles were found.

### 5.2.7 Compaction Study of PVDF Membranes

Compaction study of PVDF membranes have been reported by Ebert et al. [12]. They studied PVDF membranes of similar polymer composition as here in this study except nanofiller. $TiO_2$ nanoparticles were used for the fabrication of the membranes where the loading of the particles was 40 wt. % with respect to polymer. Membranes top surface were covered by aluminum foil and subsequently pressurized at a pressure of 30 bars. The flow of $N_2$ was measured at different time intervals at 0.2 bar feed pressure by taking aside the aluminum foil and then covering and pressurizing the membrane again. High pressure compacted the membranes and as a result $N_2$ flow decreased with time. It was found out that $N_2$ permeance of pure PVDF membranes decreased significantly compared to the MMMs indicating significantly improved ability of the membranes against compaction.

In present study it was found out that $N_2$ permeance of PVDF MMMs was higher compared to pure PVDF membranes before compression of the membrane at 30 bars (Fig. 5.7). Higher $N_2$ permeance of the MMMs before compression can be

related to their larger pores compared to pure PVDF membranes. After compression, $N_2$ permeance of MMMs indicated the same trend as pure PVDF membranes indicating that there was no significant improvement in membrane's resistance against compaction. Here it can be argued that MWCNTs loading was 2 wt. % which might not be sufficient for the mechanical stability of the membranes. PVDF MMMs with 5 wt. % MWCNTs-OH were also fabricated and tested by this method. At 5 wt. % MWCNTs-OH, again there was no improvement found in compaction property of the membranes. 5 wt. % loading of MWCNTs was the maximum possible loading as above 5 wt. % of MWCNTs a heterogeneous system was observed which hinders the formation of defect free membranes. In Fig. 5.8, the cross section of PVDF membranes, containing 5 wt. % MWCNTs-OH, before and after the pressure treatment is shown. The compaction of membrane can be well observed by reduction of the thickness of the membrane and collapsed macrovoid structures (Fig. 5.8 (b)). The decrease in $N_2$ permeance after compression is due the compaction of the porous structure of membranes.

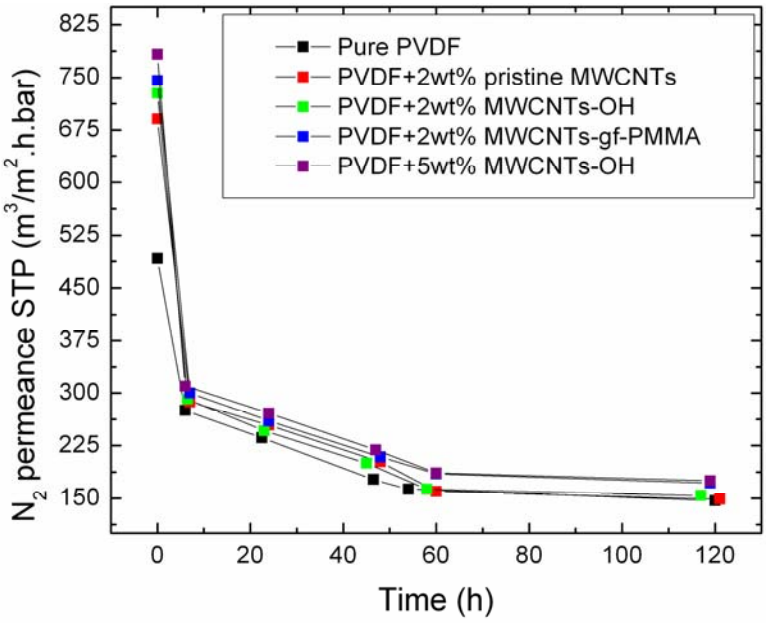


Figure 5.7: $N_2$ permeance of PVDF MMMs during the compression test.

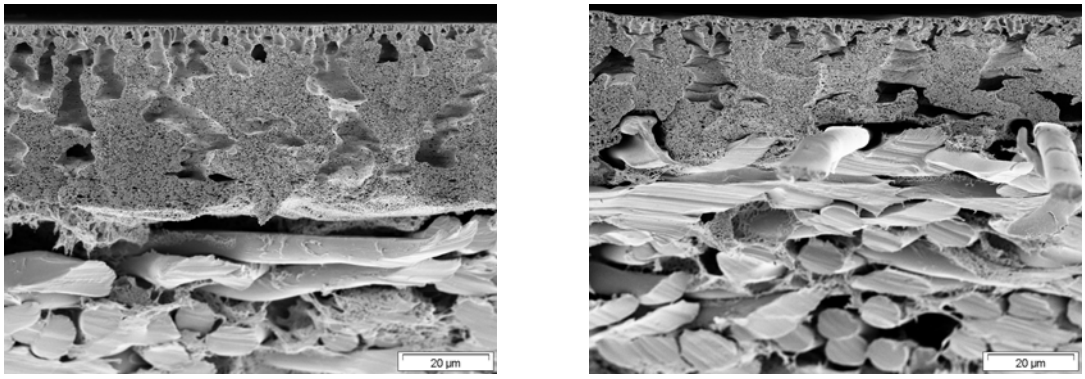


(a) (b)

Figure 5.8: SEM images of PVDF membranes loaded with 5 wt. % MWCNTs-OH (a) before and (b) after compression.

### 5.2.8 PVDF MMMs Containing MWCNTs-OH

PVDF membranes with different loading of MWCNTs-OH were also prepared to study the influence of different loading of MWCNTs-OH on the membrane properties. PVDF membranes with loading of 1, 3, and 5 wt. % of MWCNTs-OH were prepared and termed as PVDF1, PVDF3, and PVDF5 with respect to MWCNTs-OH loading.

The viscosity of the polymer solutions increased with MWCNTs-OH loading (Fig. 5.9). The increase in polymer solution viscosity with the addition of MWCNTs was also observed by different research groups. The increased viscosity of the polymer solution slows down the phase inversion process leading to relatively less porous membranes compared to pure polymer solution. It can be well observed in the cross-section morphology of the membranes where the reduced numbers of macrovoids for PVDF5 membranes (Fig. 5.8 (a)) were observed compared to pure PVDF membranes (Fig. 5.5 (a)).

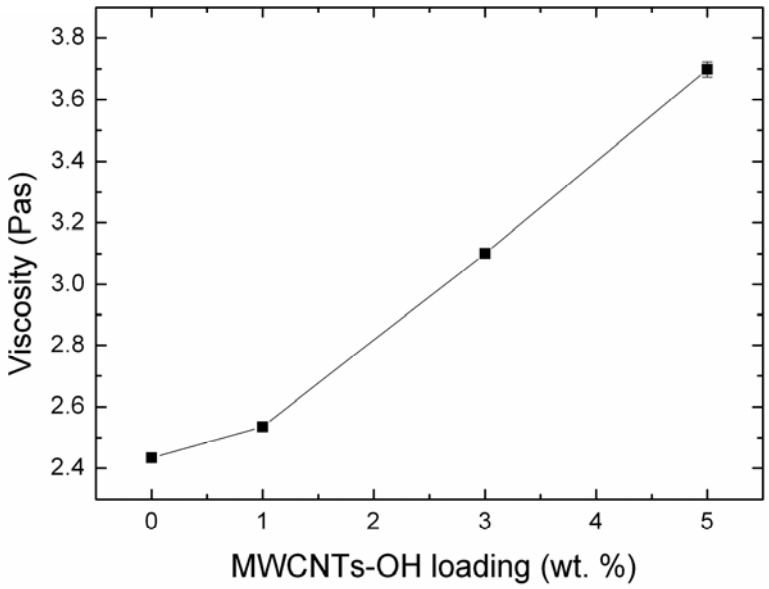


Figure 5.9: Viscosity of the PVDF solution as a function of MWCNTs-OH loading.

The pore size analysis of the PVDF MMMs with different loading of MWCNTs-OH can be observed in Fig. 5.10. The mean pore size increased with the loading of MWCNTs up to 3 wt. % and then it decreased. The increasing order of pore size was PVDF0<PVDF5<PVDF1<PVDF3. The highest mean pore size was observed for PVDF3 membranes, which indicates that the further addition of MWCNTs-OH above 3 wt. % reduces the pore size of the membranes. Choi et al. observed an increase in pore size of polysulfone membranes with gradual addition of MWCNTs up to 1.5 wt. % and addition of MWCNTs above 1.5 wt. % reduced the surface pore size [19].

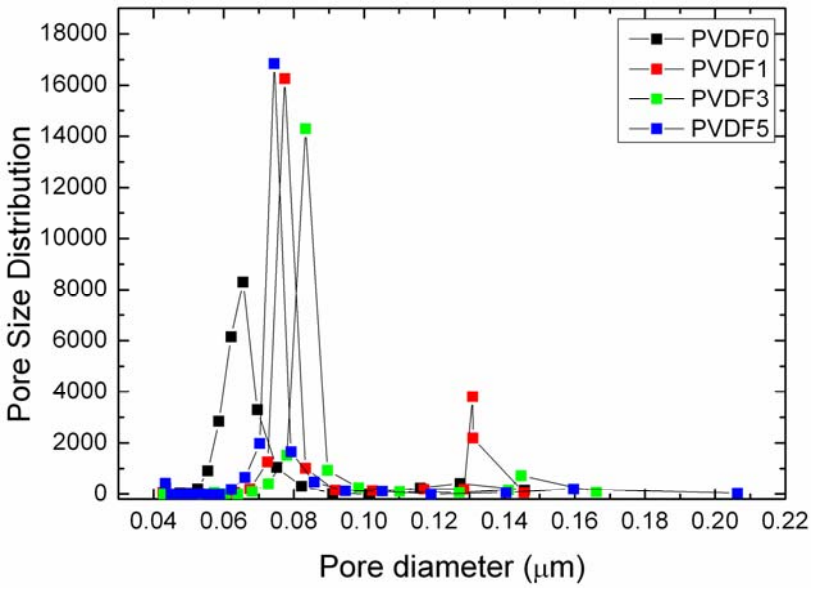


Figure 5.10: Surface pore size distribution of PVDF membranes with different MWCNTs-OH loading.

Water permeance of the PVDF MMMs was measured as a function of time and final measurement was taken after 3 hours. The water permeance showed the similar decaying trend as shown in Fig. 5.6. Average values of water permeance of PVDF membranes measured after 3 hours as a function of MWCNTs-OH loading are shown in Fig. 5.11. The permeance decreased at 1 wt. % loading and then increased at 3 and 5 wt. %. However, there was no significant improvement in water permeance of the MMMs compared to pure PVDF membranes. 100 % rejection of PS nanoparticles was observed in all the membranes.

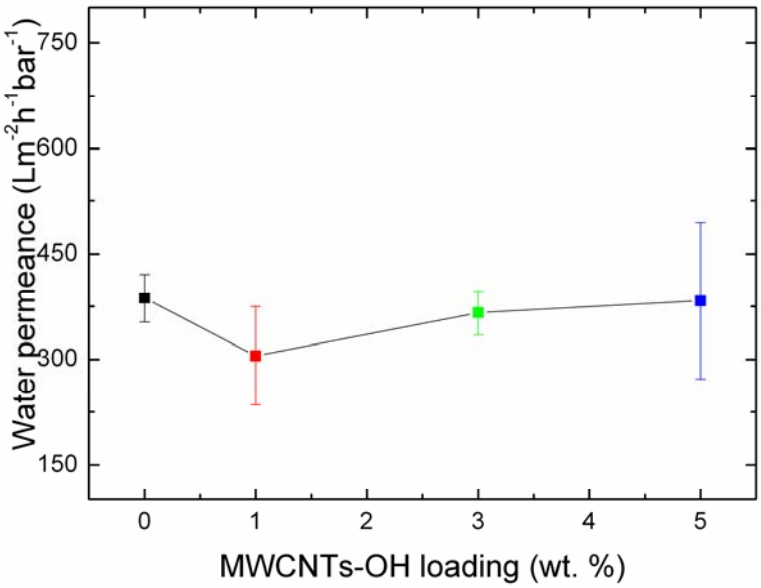


Figure 5.11: Water permeance of PVDF membranes as a function of MWCNTs-OH.

Fig. 5.12 presents the electrical sheet resistance values of PVDF MMMs as a function of MWCNTs loading. As expected, the sheet resistance decreased with the increase in MWCNTs loading. The addition of conductive nanofillers in polymer matrices provides the opportunity to develop conductive polymer nanocomposite materials which can be used for electrostatic discharge applications. Electrically conductive porous PVDF MMMs can be used as the porous support for casting thin selective dense layered composite membranes for gas separation. The conductive membranes can be used in plastic housed spiral wound membrane modules. The membrane surface having certain electrical conductivity can neutralize the static charges which may ignite the gas / $O_2$ or gas/air mixtures.

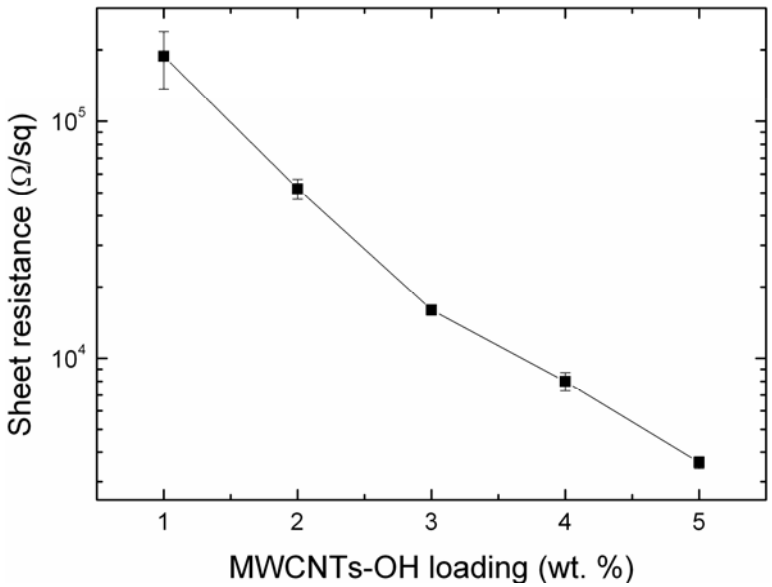


Figure 5.12: Electrical sheet resistance of PVDF MMMs as a function of hydroxyl functionalized MWCNTs.

## 5.3 Conclusions

MWCNTs were blended with PVDF and membranes were prepared by phase inversion process. The viscosity of polymer solutions containing 2 wt. % MWCNTs increased significantly. The increase in viscosity of the polymer solution led to lesser and relatively broader macrovoids especially observed in a region of upper 5 μm of the membrane cross section. PVDF membranes incorporated with MWCNTs-*gf*-PMMA showed the same cross-section morphology as pure PVDF membranes. The SEM surface images of MMMs showed increased surface pore size compared to pure PVDF membranes. The similar trend was found by pore size analysis by capillary poremeter. Hydroxyl and PMMA modified MWCNTs (MWCNT-*gt*-PMMA) showed better dispersions in the membranes compared to MWCNTs-P and MWCNTs-*gf*-PMMA. The presence of agglomerates in MWCNTs-*gf*-PMMA incorporated membrane was due to the possibility of the polymerization reaction taken place MWCNTs aggregates. MWCNTs-P incorporated membranes showed the highest electrical conductivity followed by membranes containing MWCNTs-OH and MWCNTs-*gt*-PMMA respectively. The lower conductivity in functionalized MWCNTs was due

to side wall defects and insulation of the tubes by grafted polymer chains. At the start of the measurement, the water permeance values of MMMs were higher compared to pure PVDF membranes. Decay in water permeance as a function of time was observed which was due to the lost impact of the conditioning agent and membrane compaction. After 3 hours of measurement there was no significant improvement in water permeance of the MMMs compared to pure PVDF membranes. The membranes also did not show significant improvement in their resistance against compaction carried out at higher transmembrane pressure. The different loading of MWCNTs-OH in PVDF did not lead to an improved system compared to pure. However, an increased electrical conductivity as a function of MWCNTs was observed. The electrically conductive membranes with better dispersed MWCNTs can be used for electrostatic discharge (ESD) application and in microelectronics.

## 5.4 References

[1] N. Scharnagl, H. Buschatz, Desalination, 139 (2001) 191-198.
[2] J. Ma, Z. Wang, M. Pan, Y. Guo, J. Membr. Sci., 341 (2009) 214-224.
[3] D. J. Lin, C. L. Chang, F. M. Huang, L. P. Cheng, Polym., 44 (2003) 413-422.
[4] M. Mulder, Basic principles of membrane technology: Kluwar Publishers 1996.
[5] S. Sanip, A. Ismail, P. Goh, T. Soga, M. Tanemura, H. Yasuhiko, Sep. Purif. Techn., (2011).
[6] S. Loeb, S. Sourirajan, Sea Water Demineralization by Means of an Osmotic Membrane: ACS Publications 1962.
[7] I. Pinnau, J. Wijmans, I. Blume, T. Kuroda, K. Peinemann, J. Membr. Sci., 37 (1988) 81-88.
[8] K. V. Peinemann, K. Ebert, H. G. Hicke, N. Scharnagl, Env. Prog., 20 (2001) 17-22.
[9] W. Yave, A. Car, J. Wind, K. V. Peinemann, Nanotechn., 21 (2010) 395301.
[10] S. P. Nunes, K. V. Peinemann, Membrane Technology in the Chemical Industry, 2nd edi., Wiley-VCH, 2006.
[11] A. Ismail, P. S. Goh, S. Sanip, M. Aziz, Sep. Purif. Techn., 70 (2009) 12-26.
[12] K. Ebert, D. Fritsch, J. Koll, C. Tjahjawiguna, J. Membr. Sci., 233 (2004) 71-78.

[13] T. Ebbesen, H. Lezec, H. Hiura, J. Bennett, H. Ghaemi, T. Thio, Nature, 382 (1996) 54-56.
[14] J. P. Salvetat, J. M. Bonard, N. Thomson, A. Kulik, L. Forro, W. Benoit, L. Zuppiroli, App. Phy. A: Mater. Sci. & Processing, 69 (1999) 255-260.
[15] M. Majumder, N. Chopra, R. Andrews, B. J. Hinds, Nature, 438 (2005) 44-44.
[16] H. Wu, B. Tang, P. Wu, J. Membr. Sci., 362 (2010) 374-383.
[17] S. Qiu, L. Wu, X. Pan, L. Zhang, H. Chen, C. Gao, J. Membr. Sci., 342 (2009) 165-172.
[18] D. Paul, J. Altamirano, Adv. Chem. Ser., 142 (1975) 371.
[19] J. H. Choi, J. Jegal, W. N. Kim, J. Membr. Sci., 284 (2006) 406-415.
[20] S. Majeed, D. Fierro, K. Buhr, J. Wind, B. Du, A. Boschetti-de-Fierro, V. Abetz, J. Membr. Sci., 403-404 (2012) 101-109.
[21] J. Albuerne, A. Boschetti-de-Fierro, V. Abetz, J. Polym. Sci. Part B: Polym. Phy., 48 (2010) 1035-1046.
[22] S. W. Kim, T. Kim, Y. S. Kim, H. S. Choi, H. J. Lim, S. J. Yang, C. R. Park, Carbon, 50 (2012) 3-33.
[23] A. B. Sulong, N. Muhamad, J. Sahari, R. Ramli, B. M. Deros, J. Park, Eur. J. Sci. Res., 29 (2009) 13-21.
[24] E. Celik, H. Park, H. Choi, Water res., 45 (2011) 274-282.

# Chapter 6. Polyacrylonitrile Mixed Matrix Membranes (MMMs)

## 6.1. Introduction

Polymer membranes are either porous or dense. Porous membranes are prepared mainly by a phase inversion process [1, 2]. They often show a reduction of the permeate flux at higher pressure. This decrease in permeate flux may result from the compaction of the originally porous structure to a more dense structure [3]. Tarnawski et al. reported the compaction of a GR60P ultrafiltration membrane (MWCO 25,000 D). They found a non-linear relationship between processing pressure and water flux for a pressure range varying from 0.8 to 30 bars. The compaction was considered to be the main reason for this behavior [4]. Persson et al. studied the compaction of polysulfone (PSf) and cellulose acetate (CA) membranes. They pointed out that PSf membranes undergo compaction because of their high porosity and more macrovoidic structures compared to CA membranes which have less porosity [5].

A promising way to improve mechanical stability and separation performance of the porous membranes is the utilization of nanofillers [3,6-8]. Addition of the fillers improves the mechanical stability and resistance against compaction as observed by Ebert et al. They prepared PVDF/$TiO_2$ blend membranes and tested them at a pressure of 30 bars. PVDF/$TiO_2$ membranes were clearly less susceptible to compaction compared to pure PVDF membranes [3].

Carbon nanotubes (CNTs) are also appealing membrane fillers and act as extraordinary mass transport channels as studied by various research groups [9-20]. Choi et al. blended carboxylated multi-walled carbon nanotubes (MWCNTs) with polysulfone and prepared the membranes by a phase inversion process [21]. The pure water flux increased by increasing MWCNTs content up to 1.5 wt. % and then decreased with further loading of MWCNTs. The higher flux was attributed to a hydrophilic surface and large surface pores, resulting from the addition of MWCNTs. Tang et al. used PEG6000 and MWCNTs for the

fabrication of chitosan porous membranes [8]. They observed that membranes with 10 wt. % MWCNTs loading showed 4.6 times higher water flux than pure chitosan membranes. The higher water flux was observed due to the formation of MWCNTs nanochannels in chitosan pores. Moreover, the tensile strength of the membranes increased with MWCNTs addition.

Polyacrylonitrile (PAN) micro and ultrafiltration membranes are widely used for water treatment as well as for recycling of industrial waste water e.g., in the pulp and paper industry. Kharul et al. reported an increase in transport properties of PAN ultrafiltration membranes by inorganic and organic base treatment [22]. Huang et al. observed an improvement of PAN membrane properties using $Fe_3O_4$ fillers [23]. In the present study, purified and hydroxyl functionalized MWCNTs were used as fillers in PAN ultrafiltration membranes to improve the membrane transport properties and their mechanical stability. The membrane morphology was studied by SEM analysis while the dispersion of MWCNTs was investigated by TEM. The influence of different loadings of MWCNTs on water flux, separation performance, and mechanical strength was studied. Additionally, the water flux at different feed pressures was measured to evaluate the membrane compaction which is a significant feature of this study.

## 6.2 Results and Discussion

Purified MWCNTs (MWCNTs-P) and hydroxyl functionalized MWCNTs (MWCNTs-OH) were blended with PAN and membranes were prepared by phase inversion process. The detailed procedure of membrane fabrication and characterization techniques is discussed in chapter 3. The loading of MWCNTs in PAN membranes was kept as 0.5, 1, and 2 wt. % for MWCNTs-P and MWCNTs-OH. The membranes obtained by blending MWCNTs-P were named as PAN0.5-P, PAN1.0-P, and PAN2.0-P with respect to MWCNTs loading. The membranes blended with MWCNTs-OH were named as PAN0.5-OH, PAN1.0-OH, and PAN2.0-OH.

### 6.2.1 Viscosity Measurements

The rheological properties of PAN nanocomposite solutions were studied at 20°C and a constant shear rate of 100 $s^{-1}$. An increase in solution viscosity was observed with the addition of MWCNTs-P and MWCNTs-OH (Fig. 6.1). A maximum value of the solution viscosity was observed with the highest loading of MWCNTs i.e. 2 wt. %. The increase in viscosity with MWCNTs addition indicates the occurrence of good interaction between MWCNTs and the polymer [24]. Khatua et al. found out that the addition of clay nanoparticles to polymer blends reduced the domain size of polymer blends [25]. They reported that the viscosity of the polymer blends increases with nanoparticles where nanoparticles act as physical barrier that slows down the coalescence of dispersed domains. An increase in the viscosity of the polymer solutions with MWCNTs addition was observed by Choi et al. and Tang et al. [8,21].

The viscosity of the polymer solution plays an important role to the morphology of the membranes prepared by a phase inversion process. Higher solution viscosities lead to a slower diffusion between the phase inversion components because of delayed exchange between solvent and non solvent [21,26]. The increase in viscosities of PAN solution with MWCNTs led to MMMs with reduced bulk porosities (Table 6.1). This can be explained by the delayed exchange between solvent and non solvent during the membrane formation. Celik et al. reported the decrease in surface porosity with the addition of carboxyl functionalized MWCNTs above 2 wt. % loading. The decreased porosity was related to the increase in the viscosity of the casting solution [9].

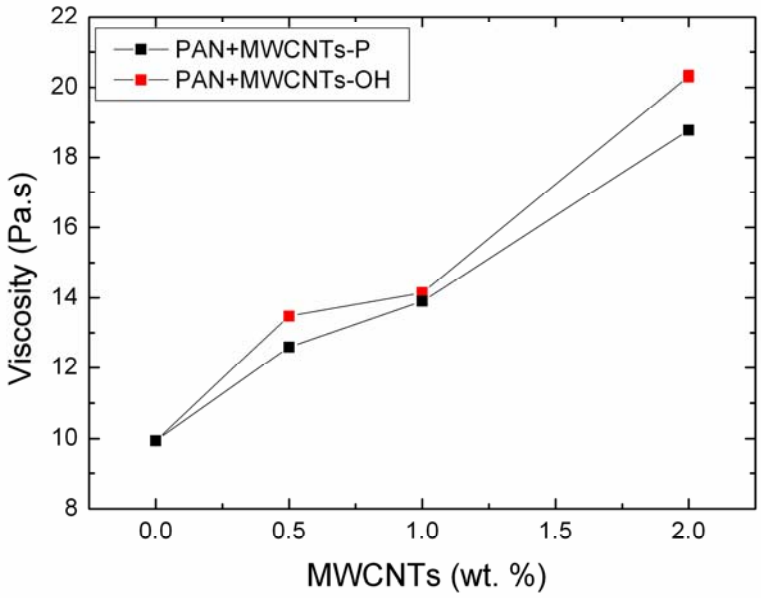


Figure 6.1: Viscosity of PAN solutions with different MWCNTs loading at a shear rate of 100 $s^{-1}$.

Table 6.1: Membrane porosity data

| Membrane | Porosity (%) |
|---|---|
| PAN0 | 67 |
| PAN0.5-P | 61 |
| PAN1.0-P | 58 |
| PAN2.0-P | 52 |
| PAN0.5-OH | 59 |
| PAN1.0-OH | 57 |
| PAN2.0-OH | 47 |

### 6.2.2 Transmission Electron Microscopy Analysis

The dispersion analysis of MWCNTs in PAN membranes was carried out by TEM. The samples for TEM analysis were prepared, on glass plate without using non-woven, via phase inversion method. Fig. 6.2 presents the TEM images of PAN membranes loaded with 2 wt. % MWCNTs-P and MWCNTs-OH. MWCNTs-P showed a bad dispersion in PAN membranes. Their agglomerates were observed in PAN matrix with very few individualized or free MWCNTs (Fig. 6.2 (a)). MWCNTs-P show a trend of agglomeration because of van-der-Waals and

$\pi-\pi$ stacking interactions among them. These interactions among MWCNTs lead to their poor dispersion in organic solvents and resulting polymer matrices. The presence of MWCNTs-P agglomerates indicates the dominance of these interactions. MWCNTs-OH showed a better dispersion in PAN membranes. From the TEM image (Fig. 6.2 (b)), it is evident that there exist small bundles of MWCNTs along with individual MWCNTs. The dispersion of individualised MWCNTs in some areas was quite homogenous but there were also some parts where also relatively bigger aggregates of MWCNTs were observed compared to the aggregates shown in Fig. 6.2. However, there were no areas without MWCNTs on the length scale of the PAN membranes. The better dispersion of MWCNTs-OH is due to their surface functionalization which dominates the non-covalent interactions among MWCNTs-OH.

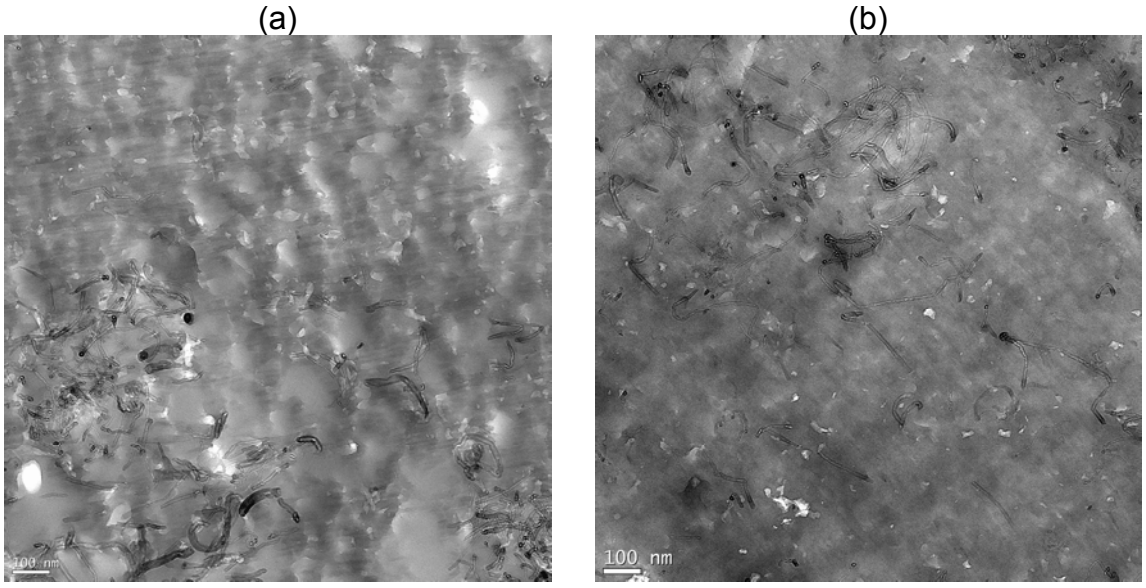


Figure 6.2: TEM images of (a) PAN2.0-P and (b) PAN2.0-OH, scale bar 100 nm.

### 6.2.3 Electrical Conductivity Measurements

PAN membranes incorporated with MWCNTs-P and MWCNTs-OH did not show surface electrical conductivity for a maximum loading of 2 wt. %. The values of resistivities were recorded by four-point measurement device. The values of

surface resistivities of MMMs were out of range of measuring device. The absence of electrical conductivity in the case of MMMs can be attributed to the insufficient contact points among MWCNTs-P and MWCNTs-OH and thus led to a non-conductive system.

### 6.2.4 Contact Angle Measurements

The surface hydrophilicity of the membranes was influenced by the addition of MWCNTs. Table 6.2 summarizes the contact angle data of pure PAN and MMMs. In case of PAN membranes incorporated with MWCNTs-P, a slight decrease in contact angle was observed compared to pure PAN membranes. The decrease in contact angle of PAN membranes incorporated with MWCNTs-OH was prominent compared to membranes incorporated with MWCNTs-P. The decrease in contact angle is related to increased surface hydrophilicity of the membranes. The pure PAN membrane presents a hydrophilic surface in the absence of MWCNTs. However, a further increase in hydrophilicity of the membrane surface can be observed by MWCNTs-OH addition. More hydrophilic surface in the case of PAN membranes incorporated with MWCNTs-OH might be due to –OH functional groups present on MWCNTs. The increase in hydrophilicity with the addition of carboxyl functionalized MWCNTs was observed by Choi et al. for polysulfone blend membranes and by Celik et al. for polyethersulfone membranes. The increased surface hydrophilicity of the membranes plays an important in water permeation and against fouling resistance [9,21].

Table 6.2: Contact angle data of PAN membranes

| Membrane | Contact angle (°) |
|---|---|
| Pure PAN | 50 (± 2) |
| PAN0.5-P | 48 (±3) |
| PAN1.0-P | 49 (± 2) |
| PAN2.0-P | 49 (± 2) |
| PAN0.5-OH | 43 (± 1.5) |
| PAN1.0-OH | 41 (± 1.5) |
| PAN2.0-OH | 42 (± 2) |

### 6.2.5 Membrane Permeation Characterization

The water fluxes of pure and PAN MMMs were measured at 2 bar transmembrane pressure. The influence of MWCNTs on water flux of the membranes is summarized in Table 6.3. The water flux of the PAN membranes increased with the addition of MWCNTs. In the case of PAN membranes incorporated with MWCNTs-P, the water flux increased by 83 % for PAN0.5-P compared to pure membranes. On further increase in MWCNTs-P content, the water flux increased ~100 % for PAN1.0-P and PAN2.0-P compared to pure PAN membranes. The increase in water flux is usually regarded with increase in surface pore size and increased hydrophilicity of the membranes. However, there was no significant increase in hydrophilicity found in membranes containing MWCNTs-P. Higher water flux of PAN MMMs might be due to increased surface pore size. The analysis of change in surface pore size can be performed by the retention of the solute molecules with different molecular weights. The membrane separation performance was evaluated for permeation of 330 ppm dextran solution composed of dextrans with different molecular weights (Table 3.1). From the analysis of feed, permeate, and retentate, a separation curve was obtained by applying eq. 6.1.

$$R = 1 - \frac{c_P}{(c_F + c_R)/2} \qquad 6.1$$

where '$c_P$', '$c_F$' and '$c_R$' are the concentrations of permeate feed and retentate solutions (g/l), respectively.

From the separation curve, the retentions at 6 Kg/mol and 50 Kg/mol are discussed in Table 6.3. The pure PAN membranes showed MWCO value of 50 Kg/mol (90 % retention). The retention of dextran with 6 Kg/mol was 57 %. The retention of dextran with 50 Kg/mol decreased with the addition of MWCNTs-P and it was ~73 % for MMMs. Also, the retention of 6 Kg/mol dextran decreased in case of PAN0.5-P (23 %), PAN1.0-P (24 %), and PAN2.0-P (29 %). The decrease in the retention of dextran for PAN membranes incorporated with MWCNTs-P indicates the increased surface pore size permitting the permeation of dextran and resulting in low retention compared to pure PAN membranes.

The water flux of PAN0.5-OH increased by 63 % compared to neat membranes. The flux decreased for membranes with loadings of MWCNTs-OH above 0.5 wt. %. For PAN1.0-OH and PAN2.0-OH membranes, the flux was still 28 % higher compared to the pure PAN membranes. A possible explanation for the increase in water flux values is the increase of hydrophilicity of the membrane surface by the addition of MWCNTs-OH (Table 6.2). Table 6.3 illustrates the separation performance of the membranes. PAN0.5-OH rejected 47 % of 6 Kg/mol dextran, which is lower compared to pure PAN (57 %), PAN1.0-OH (57 %) and PAN2.0-OH (56 %). As the MMMs did not present a significant difference in surface pore size when compared to the neat membranes (nearly similar MWCO), the rejection behaviour of 6 Kg/mol dextran in the MMMs might be explained by a combination of two opposite effects. First, the increment in hydrophilicity enhances the permeation of water through the membrane. This affects the rejection positively by increasing the total amount of water molecules that permeates through the membrane without enhancing the permeability of dextran.

Second, the higher water flux could affect negatively the retention values due to dragging of the solute (dextran) [27] which might happen in PAN0.5-OH where the low retention of dextran at 6 Kg/mol was observed. The low rejection of PAN0.5-OH might result from slightly larger pores or more interconnected pores compared to pure PAN, PAN1.0-OH, and PAN2.0-OH. Hence, increased water flux of PAN0.5-OH might also be supported by slightly larger or more interconnected surface pores in combination with increased hydrophilicity. The MWCO value of all the membranes, incorporated with MWCNTs-OH, is around 50 kg/mol or lower, as the retention of a dextran with the molecular weight of 50 Kg/mol was approximately 90 %. In the case of PAN membranes incorporated with MWCNTs-P, low retention of dextran might be due to the poor dispersion of nanotubes.

Table 6.3: Water flux and retention data of PAN MMMs.

| Membrane | Water flux ($Lm^{-2}h^{-1}$) | Dextran 6 Kg/mol | Dextran 50 Kg/mol |
|---|---|---|---|
| Pure PAN | 41 (± 3) | 57 % | 90 % |
| PAN0.5-P | 75 (± 5) | 23 % | 73 % |
| PAN1.0-P | 80 (± 15) | 24 % | 73 % |
| PAN2.0-P | 82(± 10) | 29 % | 72 % |
| PAN0.5-OH | 68 (± 2) | 47 % | 87 % |
| PAN1.0-OH | 53 (± 3) | 57 % | 88 % |
| PAN2.0-OH | 53 (± 2) | 56 % | 88 % |

### 6.2.6 Microscopic Characterization

The surface and cross sectional morphologies of the PAN membranes loaded with MWCNTs-OH are shown in Fig. 6.3 and 6.4, respectively. Identification of the surface pores is difficult due to irregular structure characteristics of the PAN membranes (Fig. 6.3). The average pore size was determined by measuring the diameter of a minimum of 150 pores from three different scanning electron

micrographs with 100k magnification. The surface morphology was not significantly affected by the addition of MWCNTs in terms of pore sizes and pore size density. The average pore sizes calculated from the SEM pictures are shown in Table 6.4, where the lack of influence of the nanofillers on the surface pore size is evident.

Table 6.4: Surface pore size data of PAN membranes with MWCNTs-OH

| Membrane | Pore Size (nm)* |
|---|---|
| PAN0 | 11 (±3) |
| PAN0.5-OH | 11 (±2) |
| PAN1.0-OH | 11 (±2) |
| PAN2.0-OH | 10 (±2) |

* measured by SEM

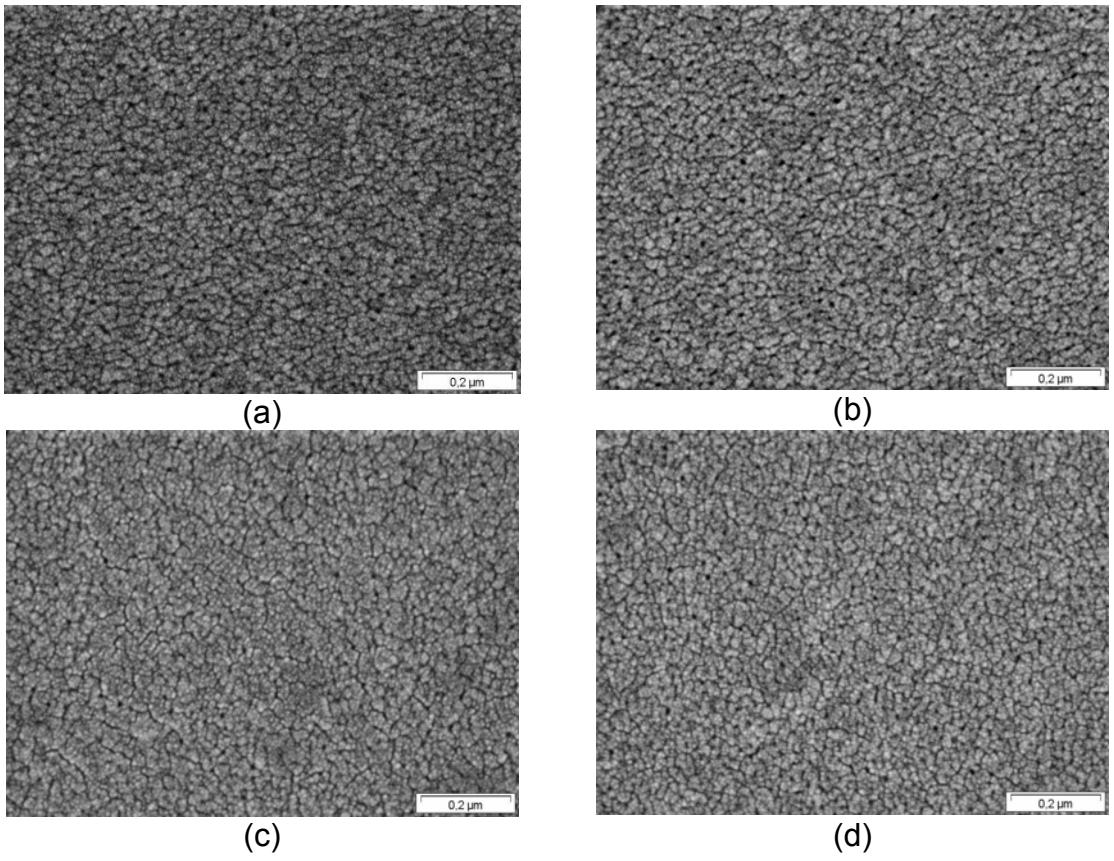


Figure 6.3:SEM surface images of PAN membranes (a) Pure PAN, (b) PAN0.5-OH, (c) PAN1.0-OH and (d) PAN2.0-OH (scale bar for a to d is 200 nm).

On the contrary, the cross sectional morphology (Fig. 6.4) was greatly influenced by the addition of MWCNTs. The number of macrovoids decreased with MWCNTs loading and in PAN2.0-OH least macrovoids were observed. However, the size of the macrovoids was observed to increase with the content of MWCNTs. In PAN MMMs, the enlarged macrovoids may result from the fusion of disappearing macrovoids as the solution viscosity increases. Celik et al. observed the reduction of macrovoids in polyethersulfone membranes upon addition of 2 wt. % MWCNTs [9]. They related this effect with the increase in viscosity of casting solutions where increased viscosities slow down the phase separation. An increase in the size of the macrovoids might create the possibility of less number of pores with big pore size in the cross-section of the membrane. The thickness of the thin separating layer on the top tends to increase with MWCNTs addition. SEM cross sectional pictures do not give any information about the dispersion state of MWCNTs. It is difficult to distinguish MWCNTs from cross sectional microstructures of the polymer (see for example a magnified area in Fig. 6.4 (e)). However, TEM characterization showed their good dispersion in PAN MMMs (Fig. 6.2 (b)).

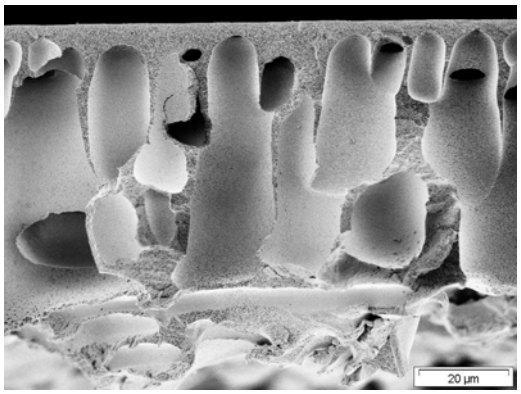


(a)

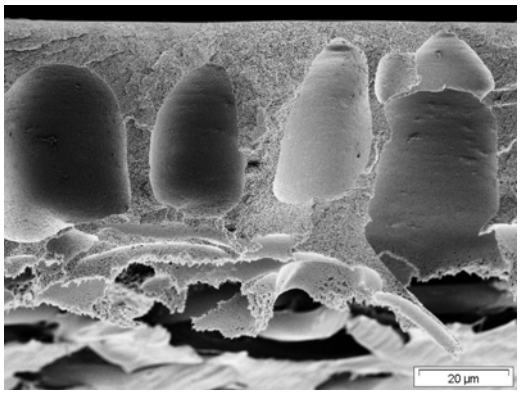


(b)

*Figure 6.4 continued*

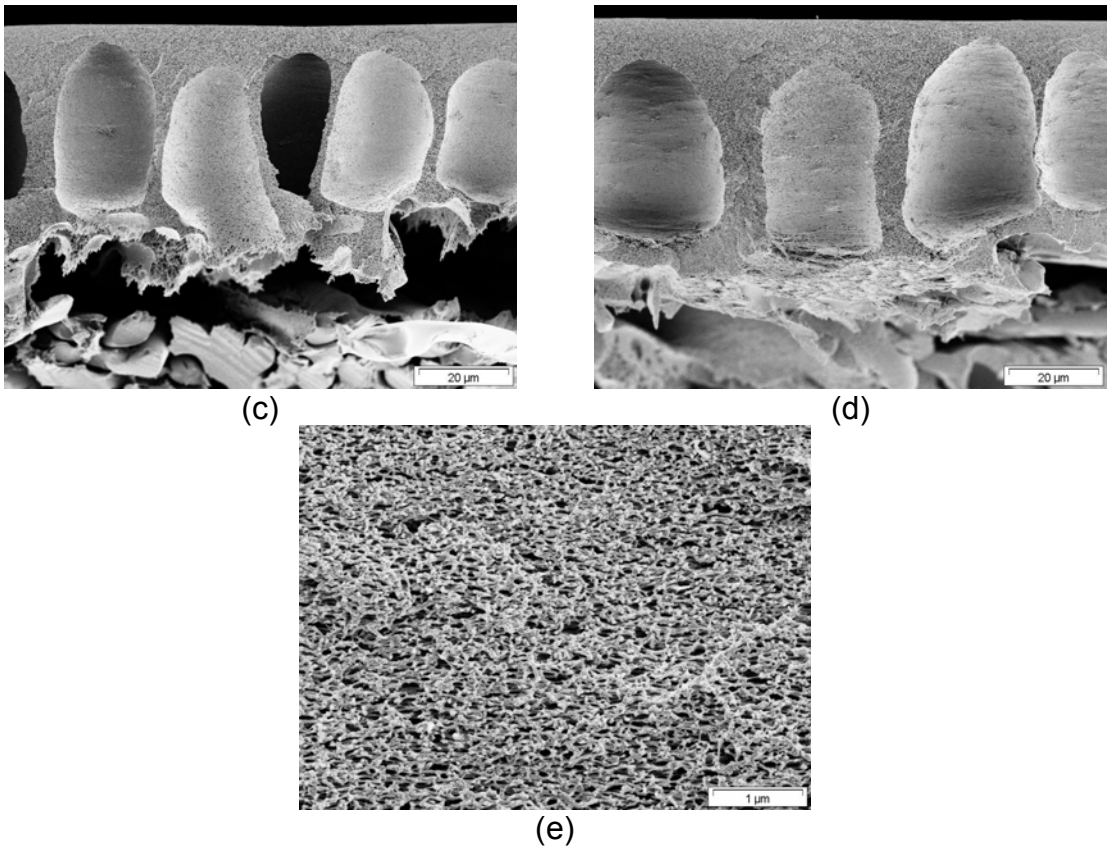


(c) (d)

(e)

Figure 6.4: SEM cross-section images of PAN membranes (a) PAN0, (b) PAN0.5-OH, (c) PAN1.0-OH, (d) PAN2.0-OH and (e) magnified PAN2.0-OH. Scale bar for images a to d is 20µm, and for e it is 1µm.

### 6.2.7 Membrane Compaction Study

Compaction studies were conducted to observe the response of the porous structure of the membranes at increased pressures and its impact on water flux during the filtration. The flux of a component 'i', '$J_i$', across a membrane often is a linear function of the transmembrane pressure (pressure drop) '$\Delta P$': [28]

$$J_i = L_i \cdot \Delta p \qquad 6.2$$

'$L_i$' denotes the permeability coefficient of component 'i' (permeance). Porous composite membranes may experience a reduction in flux under the effect of high pressure and this phenomenon can also be observed in the here studied

PAN membranes. The majority of composite membranes can undergo compaction during the filtration process. This reduces the pore sizes or free volume inside the membrane and thus reduces the permeability coefficient, which leads to a reduction of permeate flux. Machado et al. [28] reported the dropping behaviour of flux with the increase in transmembrane pressure for nanofiltration membranes, which can be expressed by eq. 6.3, where '$L°_i$' is the permeance under atmospheric pressure, and $\alpha$ is the compaction factor, respectively:

$$J_i = L_i° \cdot e^{-\alpha \cdot \Delta P} \cdot \Delta p \qquad 6.3$$

By comparing eq. 6.2 and 6.3 the transmembrane pressure dependence of the permeability coefificient is obtained:

$$L_i = L_i° \cdot e^{-\alpha \cdot \Delta p} \qquad 6.4$$

For compaction studies, water was permeated through the membranes for 40 minutes at a transmembrane pressure of 2 bar. After this treatment the water flux was measured at 2, 4, 6, 8 and 10 bar, where each pressure was maintained for 10 minutes prior to the flux measurement. Fig. 6.5 shows the mean flux as a function of pressure. The membrane compaction factor ($\alpha$) can be calculated by plotting ln(J/$\Delta$P) against the applied pressure drop $\Delta$P (as shown in Fig. 6.6), '$\alpha$' being the slope of the straight line. The values of '$\alpha$' are summarized in Table 6.5, where '$\alpha$' for PAN2.0-OH was 36 % lower compared to pure PAN. The compaction factor of PAN2.0-P was higher compared to PAN2.0-OH which might be due to better dispersion of MWCNTs-OH in PAN compared to MWCNTs-P. Returning from 10 to 2 bar, the flux never came back to its initial value. The flux reduction can be calculated from water flux values measured at 2 bars before and after the pressure treatment.

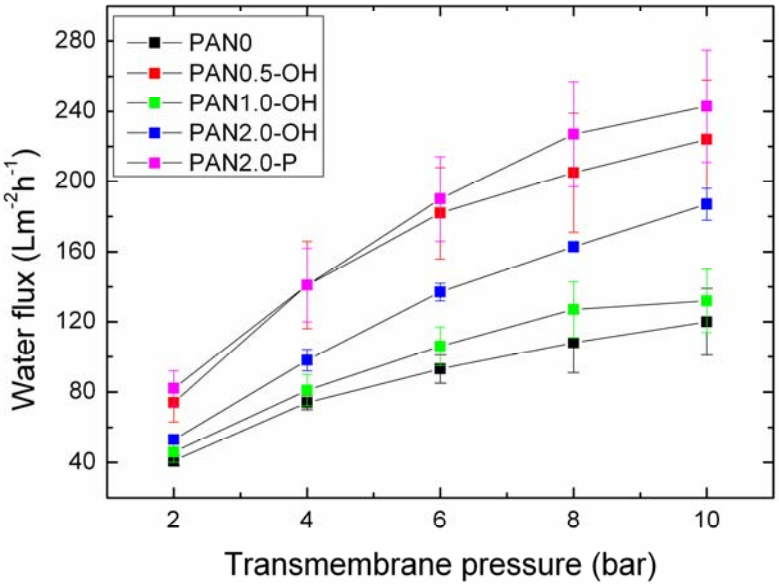


Figure 6.5: Water flux of PAN MMMs as function of transmembrane pressure ΔP.

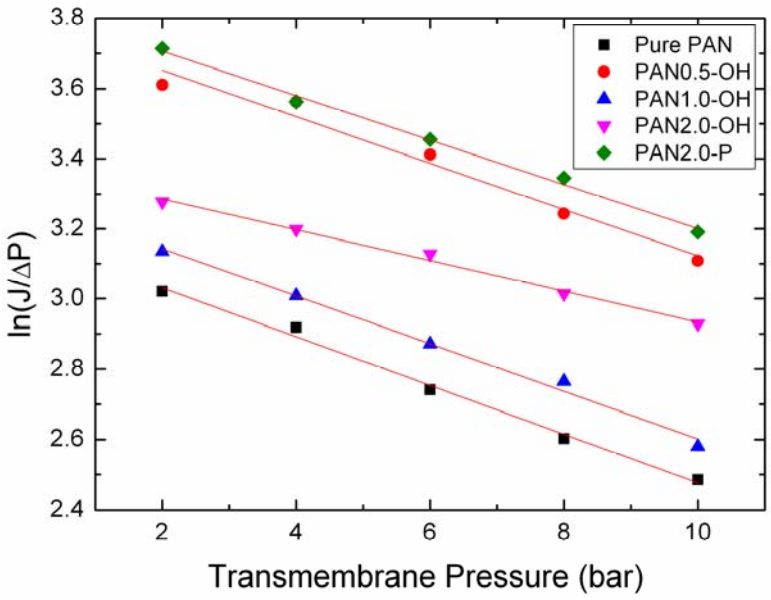


Figure 6.6: Plot of the ln(J/ΔP) as a function of the transmembrane pressure ΔP for compaction characterization.

Table 6.5: Compaction factor (α) ($bar^{-1}$) of PAN MMMs

| Membrane | Compaction factor (α) $bar^{-1}$ |
|---|---|
| PAN0 | 0.069 |
| PAN0.5-OH | 0.066 |
| PAN1.0-OH | 0.067 |
| PAN2.0-OH | 0.044 |
| PAN2.0-P | 0.063 |

For PAN2.0-OH, the flux reduction after pressure treatment was less compared to neat, PAN0.5-OH and PAN1.0-OH which shows that higher pressure application could be well sustained by PAN2.0-OH (Fig. 6.7). After the flux measurements, the membranes were placed into a mixture of water and isopropanol (1:1) for 10 minutes for the pore opening. The water flux was recovered again which indicates the reversible nature of compaction.

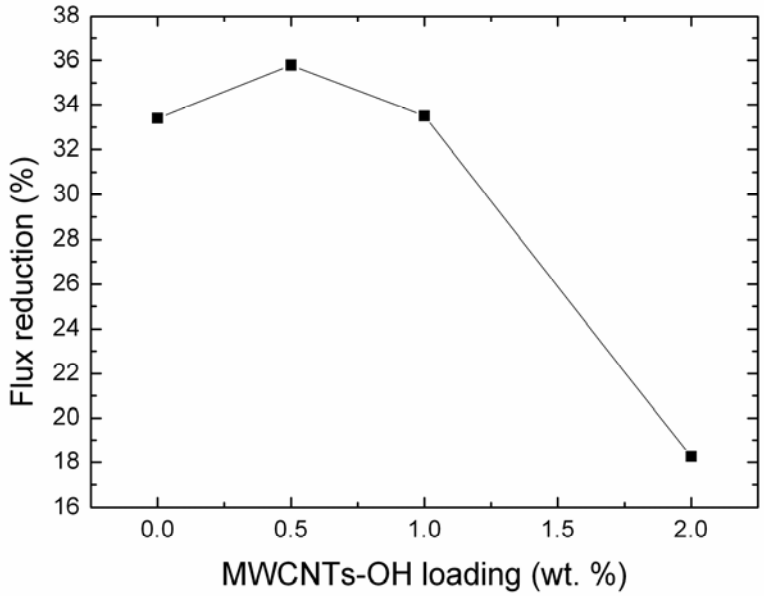


Figure 6.7: Water flux reduction before and after the variation of the transmembrane pressures from 2 to 10 bar as a function of MWCNTs content.

The improved compaction resistance of PAN2.0-OH might be due to reduced porosity and better interactions between tubes and PAN. To study the possible

interactions between MWCNTs-OH and PAN spectroscopic analysis was carried out which is given in the next section.

### 6.2.8 Spectroscopic Analysis

Fig. 6.8 depicts the FTIR absorption spectra of MWCNTs and MMMs. MWCNTs show the –OH stretching vibration at 3440 $cm^{-1}$ and a conjugation of C=O with C=C bonds at 1630 $cm^{-1}$. A very small peak at 1735 $cm^{-1}$ indicates the presence of carboxyl groups. Pure PAN membranes showed the typical nitrile (C≡N) peak at 2245 $cm^{-1}$, C-H stretching at 2933 $cm^{-1}$ and deformation at 1452 $cm^{-1}$, respectively. These PAN peaks were also observed in PAN MMMs (PAN2.0-OH). The appearance of a hump at 3440 $cm^{-1}$ in the PAN2.0-OH membrane can be related to –OH groups present on MWCNTs. Marie et al. observed the hydrogen bond interaction between C≡N and –OH functional groups by a shift of C≡N peak [29]. However, only a very slight shift (1.5 $cm^{-1}$) of the C≡N peak was observed in the MMMs (PAN2.0-OH), which is negligible to prove the hydrogen bonding between –OH and C≡N groups (inset of Fig. 6.8). –OH functional groups present on MWCNTs are very less compared to the C≡N groups in the MMMs which might be the reason of the negligible peak shift.

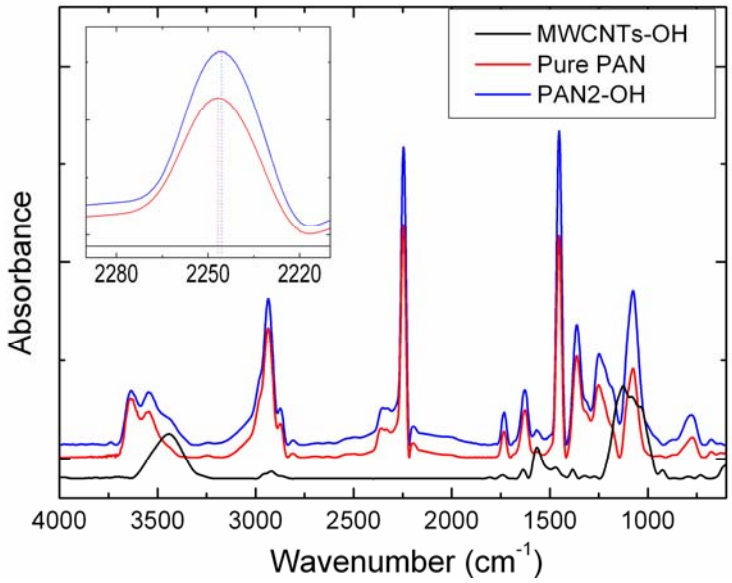


Figure 6.8: FTIR spectra of MWCNTs and PAN nanocomosite membranes.

In order to clarify the question of specific interactions between polymer matrix and MWCNTs-OH, further investigation was made by Raman spectroscopy. Peak shifts were observed for PAN1.0-OH and PAN2.0-OH MMMs in the tangential vibration mode (Fig. 6.9). Both G (1601.26 $cm^{-1}$) and D (1306.76 $cm^{-1}$) bands of MWCNTs were shifted ~8 $cm^{-1}$ for PAN1.0-OH and PAN2.0-OH compared to MWCNTs. Similar shifts were also observed by Baskaran et al. in nanocomposites of MWCNTs and polybutadiene [30]. The coverage of MWCNTs surface with polymer chains is enhanced at low loadings of MWCNTs. This affects the movement of C-C bonds in the graphene plane due to CH-$\pi$ interactions between the carbon atoms of the MWCNTs and the CH-groups of the polymer. Therefore, the observed peak shifts can be related to the CH-$\pi$ interaction between PAN and MWCNTs.

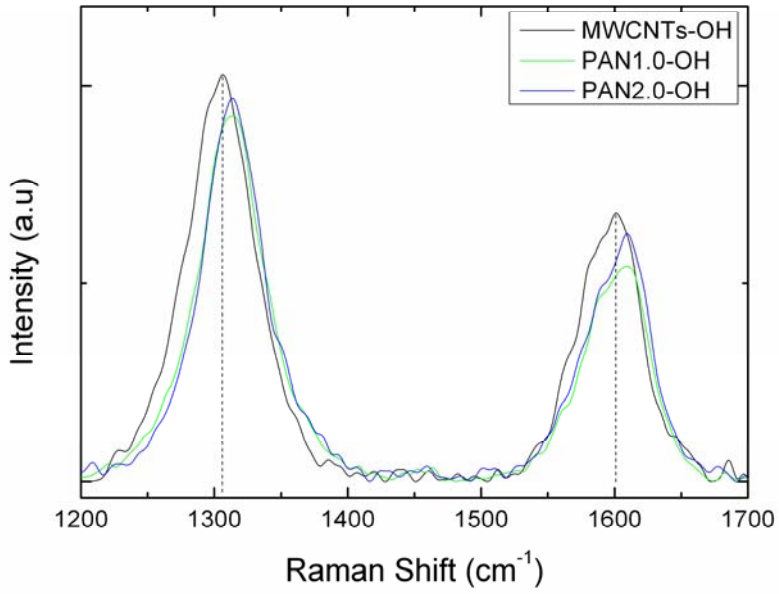


Figure 6.9: Raman spectra of MWCNTs-OH, PAN1.0-OH and PAN2.0-OH.

### 6.2.9 Mechanical Characterization

The tensile strength of PAN MMMs as a function of MWCNTs-OH content is shown in Fig. 6.10. The tensile strength at break increases with MWCNTs-OH addition. For PAN2.0-OH membranes it increased over 97 % compared to pure

PAN membranes. The increase in tensile strength of PAN MMMs is expected as it is also well-known from fibre reinforced polymer composites, where the fillers are sufficiently bound to the matrix, i.e. have some good interactions (here: CH-$\pi$ interactions as concluded from the Raman spectra shown in Fig. 6.9). As in the present case porous materials are investigated, another reason is the decreased porosity of the MMMs with increased filler loadings (Table 6.1). The similar effect is reported in literature where decrease in porosity of the PAN membranes was observed by increase in polymer solution concentration. Consequently, membranes with less porosity showed good mechanical strength compared to highly porous membranes [31]. The increased tensile strength of PAN2.0-OH membranes also supports the improved compaction properties.

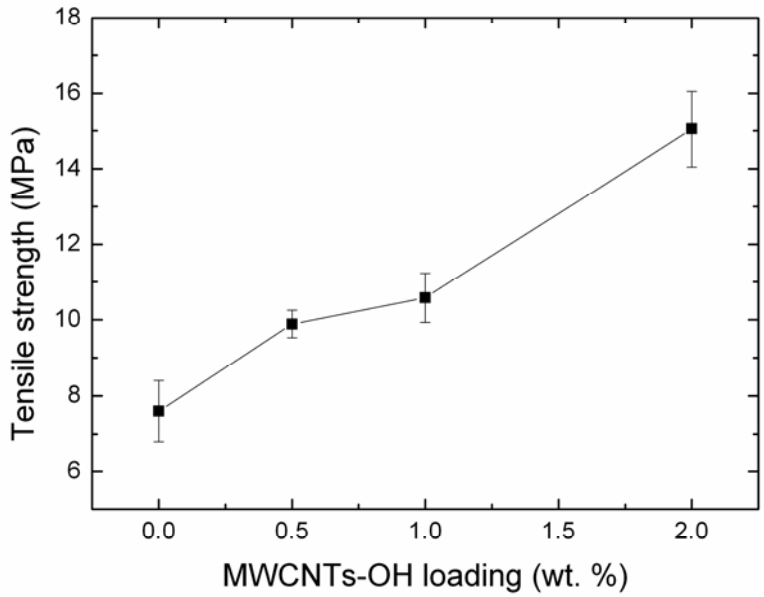


Figure 6.10: Tensile strength at break as a function of MWCNTs loading (wt. %).

## 6.3 Conclusions

PAN ultrafiltration MMMs with improved properties were successfully prepared by a phase inversion process. The addition of MWCNTs-P and MWCNTs-OH led to the increase in polymer solution viscosity. MWCNTs-OH showed better dispersion compared to MWCNTs-P which was confirmed by TEM. The increased solution viscosity with MWCNTs-OH suppressed the formation of

macrovoids and led to a reduced number of bigger sized macrovoids compared to pure PAN membranes. However, the surface pore sizes seemed not to be affected by the viscosity of the composite solution, which was also reflected by the similar molecular weight cut off observed for all membranes under study (dextran with a molecular weight of 50 Kg/mol was retained by approximately 90 % on the feed side). Introduction of MWCNTs enhanced the water flux of the membranes especially at 0.5 wt. % MWCNTs-OH loading. The water flux was reduced for membranes with higher loadings of MWCNTs-OH, but it was still higher compared to pure PAN membranes in all cases. PAN membranes loaded with MWCNTs-P showed higher water flux compared to membranes loaded with MWCNTs-OH. However, a lower retention of dextran was observed in the former. Moreover, the compaction of the membranes was significantly reduced upon larger pressures due to the reinforcement properties of the MWCNTs-OH. Therefore, by addition of well-dispersed MWCNTs-OH the transport properties of PAN membranes could be improved. Also the tensile strength of PAN MMMs was improved with the addition of MWCNTs-OH. An indication for a good interaction between MWCNTs-OH and PAN was given by Raman spectroscopy. The increase in tensile strength and resistance against compaction may result from the decrease in porosity and good interaction of MWCNTs-OH with PAN. Hence, MWCNTs-OH provide a way to improve the mechanical stability and transport properties of the PAN ultrafiltration membranes and enables their applications at high transmembrane pressures.

## 6.4 References

[1] A. F. Ismail, P.S. Goh, S.M Sanip, M. Aziz, Separ. Purif. Technol., 70 (2009) 12–26.
[2] M. Mulder, Basic Principles of Membrane Technology, 2nd edi., Kluwar Publishers, 1996.
[3] K. Ebert, D. Fritsch, J. Koll, C. Tjahjawiguna, J. Membr. Sci., 233 (2004) 71-78.
[4] V.R. Tarnawski, P. Jelen, J. Food Eng., 5 (1986) 75-90.
[5] K.M. Persson, V. Gekas, G. Trägårdh, J. Membr. Sci., 100 (1995) 155-162.

[6] L. Yan, S. Hong, M. L. Li, Y. S. Li, Separ. Purif. Technol., 66 (2009) 347–352.
[7] D. S. Kim, H. B. Park, Y. M. Lee, Y. H. Park, J. W. Rhim, J. App. Polymer Sci., 93 (2004) 209–218.
[8] C. Tang, Q. Zhang, K. Wang, Q. Fu, C. Zhang, J. Membr. Sci., 337 (2009) 240-247.
[9] E. Celik, H. Park, H. Choi, H. Choi, Water Res., 45 (2011) 274-282.
[10] L. Dumee, L. Velleman, K. Sears, M. Hill, J. Schutz, N. Finn, M. Duke, S. Gray, Membranes, 1 (2011) 25-36.
[11] L. F. Dumée, K. Sears, J. Schütz, N. Finn. C. Huynh, S. Hawkins, M. Duke, S. Gray, J. Membr. Sci., 351 (2010) 36-43.
[12] J. H Choi, J. Jegal, W. N. Kim, H. S. Choi, J. App. Polym. Sci., 111 (2009) 2186-2193.
[13] X. Peng, J. jin, Y. Nakamura, T. Ohno, I. Ichinose, Nature Nanotechnol., 4 (2009) 353-357.
[14] A. I. Skoulidas, D. M. Ackerman, J. K. Johnson,D. S. Sholl, Phy. Rev. Lett., 89 (2002) 185901-1-4.
[15] S. Joseph, N. R. Aluru, Nano Lett., 8 (2008) 452-458.
[16] M. Majumder, N. Chopra, R. Andrews, B. J. Hinds, Nature 438 (2005) 44.
[17] B. J. Hinds, N. Chopra, T. Rantell, R. Andrews, V. Gavalas, L. G. Bachas, Science, 303 (2004) 62-65.
[18] M. Majumdar, N. Chopra, B. J. Hinds, J. Am. Chem. Soc., 127 (2005) 9062-9070.
[19] S. Kim, J. R. Jinschek, H. Chen, D. S. Scholl, E. Marand, Nano Lett., 7 (2007) 2806-2811.
[20] S. Kim, T. W. Pechar, E. Marand, Desalination, 192 (2006) 330-339.
[21] J. H. Choi, J. Jegal, W. N. Kim, J. Membr. Sci., 284 (2006) 406-415.
[22] H. R. Lohokare, S. C. Kumbharkar, Y. S. Bhole, U. K. Kharul, J. App. Polym. Sci., 101, (2006), 4378-4385.
[23] Z. Q. Huang, Z. Y. Chen, X. P. Guo, Z. Zhang, C. L. Guo, Ind. Eng. Chem. Res., 45 (2006) 7905-7912.
[24] Y. Y. Huang, S. V. Ahir, and E. M. Terentjev, Physical Review B, 73 (2006) 125422.
[25] B. B. Khatua, D. J. Lee, H. Y. Kim, J. K. kim, Macromolecules, 37 (2004) 2454-2459.
[26] S. Qiu, L. Wu, X. Pan, L. Zhang, H. Chen, C. Gao, J. Membr. Sci., 342 (2009) 165-172.
[27] N. Stafie, D.F. Stamatialis, M. Wessling, J. Membr. Sci. 228 (2004) 103-116.
[28] D. R. Machado, D. Hasson, R. Semiat, J. Membr. Sci. 163 (1999) 93–102.
[29] O. Marie, F. T. Starzyk, J. C. Lavalley, Phys. Chem. Chem. Phys. 2 (2000) 5341-5349.
[30] D. Baskaran, J. W. Mays, M. S. Bratcher, Chem. Mater. 17, (2005) 3389-3397.
[31] N. Scharnagl, H. Buschatz, Desalination 139 (2001) 191-198.

# Chapter 7. Poly(dimethylsiloxane) (PDMS) Mixed Matrix Membranes (MMMs)

## 7.1 Introduction

PDMS is a well known rubbery polymer for the separation of hydrocarbons from permanent gases [1]. The transport of $H_2$, $O_2$, $N_2$, $CO_2$, $CH_4$, and $C_2$- $C_4$–based organic molecules through PDMS membranes are reported during various studies [2-6]. The gas separation performance of conventional polymeric membranes follow a trade-off between selectivity and permeability, as indicated by Robeson's upper bound [7]. This trade-off has led to the development of mixed matrix membranes (MMMs) with inorganic fillers embedded into polymer matrix [8-11]. Porous inorganic fillers have been reported to improve the separation performance of the conventional membrane materials e.g., zeolite mixed PDMS membranes has given rise to the remarkable improvement of selectivity of gases compared to pure PDMS membranes [12].

Carbon nanotubes possess excellent transport properties as reported by Ackerman et al. by atomic simulations results for self and transport diffusivity of light gases, e.g., $CH_4$ and $H_2$ etc. [13]. They found that transport rates of these gases in CNTs were higher than in zeolites. These basic theoretical transport studies laid the foundation of CNTs mixed matrix membranes for gas separation. Kim et al. reported the incorporation of CNTs into polyimide siloxane matrix to fabricate MMMs [14]. The increase in permeability of gases with CNTs was attributed to the increased diffusivity of these gases through the interior of CNTs.

The aim of this study is two fold: (1) incorporation of multi-walled carbon nanotubes (MWCNTs) in PDMS membranes to improve the gas separation performance compared to pure PDMS membranes (2) utilizing MWCNTs in PDMS to introduce electrical conductivity in PDMS composite membranes. Such conductive membranes, when applied in spiral wound membrane modules with plastic housing, can provide the opportunity to neutralize electrostatic charges and hence may provide, for example, a safer separation of hydrocarbons. In

order to avoid electrostatic charging, a surface resistivity lower than a range of $10^6$ Ω/□ and $10^9$ Ω/□ or bulk electrical conductivity above $10^{-6}$ $Sm^{-1}$ are required [15, 16].

It was a challenge to uniformly disperse non-functionalized MWCNTs in a thin PDMS selective layer because of their indispersibility in non-polar solvents like *n*-hexane or toluene. PDMS MMMs were prepared by incorporating purified MWCNTs (MWCNTs-P) and pyrene-POSS modified MWCNTs (MWCNTs-PPy). PDMS composite membranes were prepared using MWCNTs-P, MWCNTs-PPy and polystyrene functionalized MWCNTs (MWCNTs-*gf*-PS). The functionalization of the fillers has significant impact on their dispersion in composite membranes. The details of the functionalization procedure have been given in chapter 3 with subsequent discussion in chapter 4.

## 7.2 Results and Discussion

### 7.2.1 PDMS MMMs

PDMS dense MMMs were prepared by solvent evaporation. MWCNTs-P did not exhibit a stable dispersion in solvent (toluene) and the resultant MMMs showed the presence of MWCNTs agglomerates. Fig. 7.1 (a) shows the digital photograph of PDMS membrane loaded with 0.5 wt. % MWCNTs-P. The aggregation of MWCNTs in membrane is visually observable. There exist van-der-Waals and $\pi-\pi$ stacking interactions among MWCNTs which are responsible for their aggregation in organic solvents and in resultant polymer composites prepared by solvent evaporation. The aggregation of MWCNTs was much prominent at 0.5 wt. % loading of MWCNTs-P in MMMs without any aid of a microscope. However, at 1 wt. % MWCNTs loading, the unfilled space which is observable in Fig. 7.1 (a), was occupied by the additional MWCNTs making it completely black. A similar observation of SWCNTs agglomerates has been reported in polyamide siloxane membranes by Pechar [17]. The impact of functionalization of MWCNTs is quite obvious and can be observed in Fig. 7.1

(b), where the homogeneously black film was obtained at 0.5 wt. % loading of MWCNTs-PPy. Pyrene interacts with MWCNTs via $\pi-\pi$ interaction and POSS moiety enable their stable dispersion because of its solubility in toluene. Surface functionalization of MWCNTs reduced the intertube interactions which prevented their agglomeration in solvent and in resultant PDMS MMMs. The quality of dispersion of MWCNTs can be better observed by scanning electron microscope (SEM) analysis.

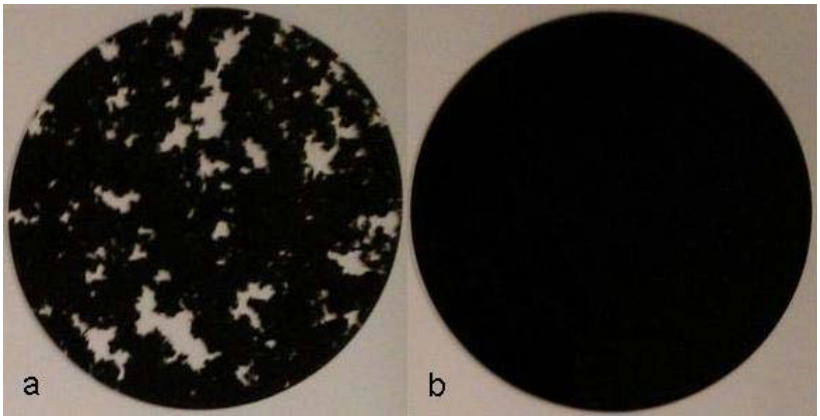


Figure 7.1: PDMS MMMs loaded with 0.5 wt. % (a) MWCNTs-P, (b) MWCNTs-PPy.

PDMS membranes, loaded with 1 wt. % MWCNTs-P, appeared completely black with no MWCNTs-free spaces perceived visually. SEM analysis was performed on PDMS membranes containing 1 wt. % MWCNTs. The dispersion quality of purified and modified MWCNTs can be observed in Fig. 7.2. The agglomerates of MWCNTs-P are visible along with the free spaces i.e. without MWCNTs (Fig. 7.2 (a-b)). During SEM analysis, there were found many regions without MWCNTs at micron scale, however, SEM images were taken from the places where MWCNTs were present. MWCNTs-PPy showed a much better dispersion compared to MWCNTs-P and there were observed no big agglomerates of MWCNTs like MWCNTs-P. Although, it is difficult to observe MWCNTs-PPy at low magnification but their presence can be proved by small dots observed in Fig. 7.2 (c). At higher magnification, the presence of well dispersed MWCNTs-

PPy was observed in Fig. 7.2 (d). A good dispersion of tubes indicates the effectivity of their functionalization. The homogeneous dispersion of the nanofillers is of prime importance to expect the better properties of the resultant nanocomposites especially in membranes.

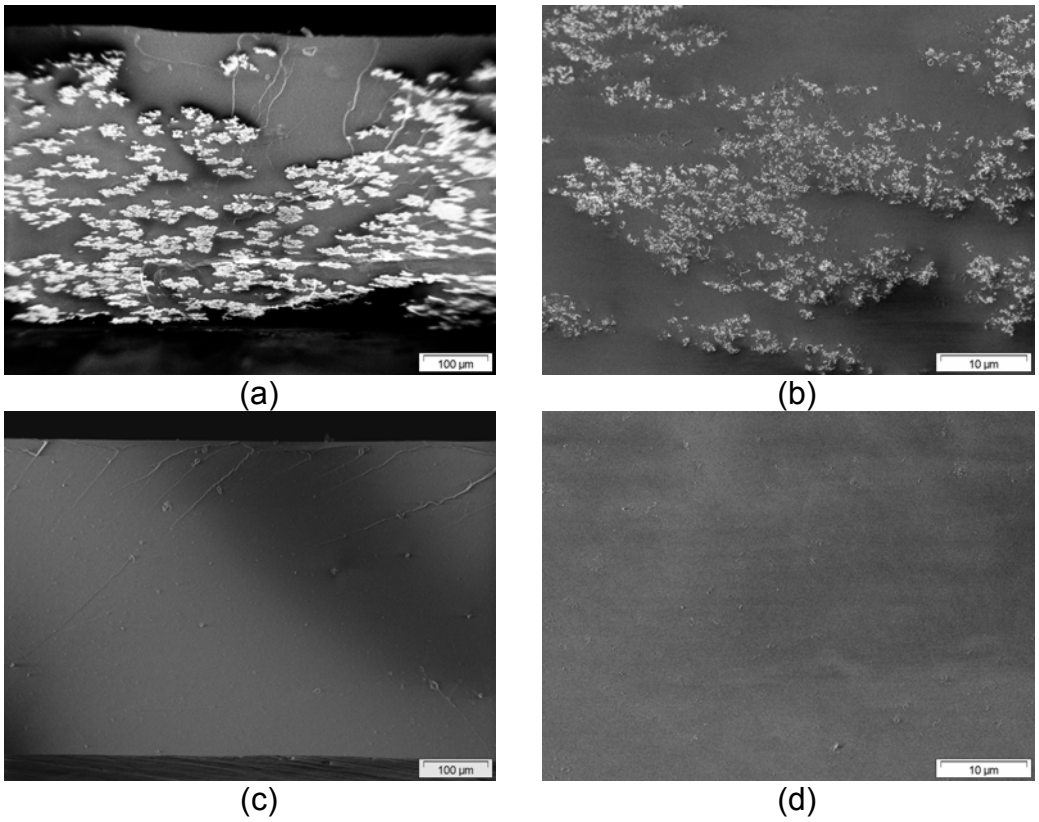


Figure 7.2: Cross-section images of PDMS MMMs containing 1 wt. % (a-b) MWCNTs-P, (c-d) MWCNTs-PPy.

### 7.2.2 Rheological Properties of PDMS Nanocomposites

In order to understand the structure properties relationships, the rheological properties of PDMS nanocomposites were studied. The samples for rheological measurements were prepared without using a catalyst and crosslinker system. It can be observed from Fig. 7.3 that the complex viscosity of PDMS increased with increasing MWCNTs contents. However, the increase in complex viscosity of the nanocomposites containing MWCNTs-P (Fig. 7.3 (a)) was higher compared to the MWCNTs-PPy (Fig. 7.3 (b)) containing nanocomposites. The storage

modulus of PDMS nanocomposite also increased with MWCNTs addition. Like the complex viscosity, the storage modulus of PDMS nanocomposites embedded with MWCNTs-P was higher compared to the PDMS nanocomposites containing MWCNTs-PPy (Fig. 7.4). This case study resembles the observation of Song et al. for MWCNTs embedded in epoxy [18]. They studied the rheological properties of epoxy nanocomposites with two different states of MWCNTs dispersion i.e., well dispersed and poorly dispersed MWCNTs. The elevation in complex viscosity and increased storage modulus were observed in epoxy nanocomposites embedded with poorly dispersed MWCNTs. The interactions between polymer and CNTs become more pronounced with an increase in CNTs loading, because of their high aspect ratio. CNTs possess CH–$\pi$ interactions with PDMS [19]. PDMS chains wrap around individual CNTs or their agglomerates and lead to increase in complex viscosity and storage modulus with MWCNTs loading. With the increase in MWCNTs loading more surface area of MWCNTs is available to interact with PDMS chains. In the case of MWCNTs-PPy the increasing order of complex viscosity is lower compared to MWCNTs-P. The shielding effect of pyrene-POSS on MWCNTs might hinder the feasible CH–$\pi$ interactions with PDMS and MWCNTs and thus leading to a lower complex viscosity and storage modulus of the system compared to MWCNTs-P system.

**(a)**

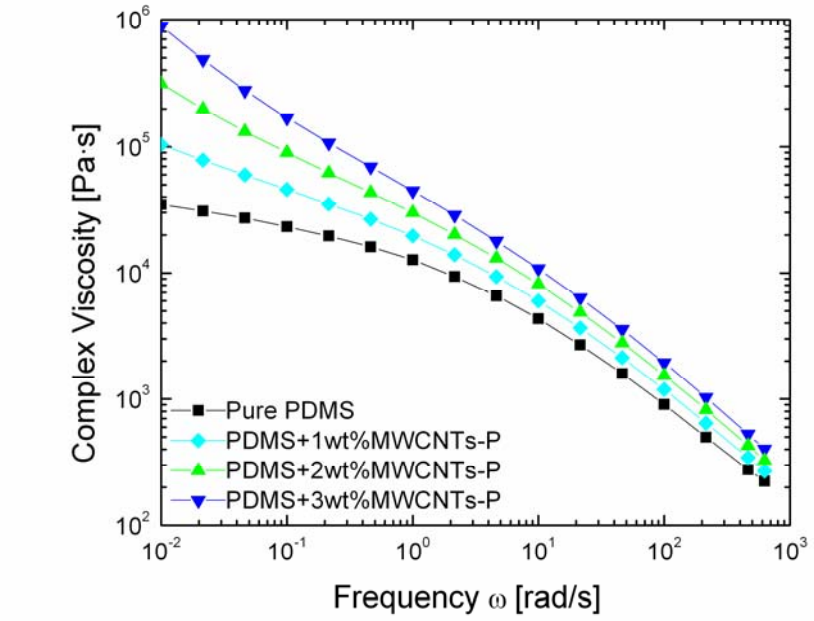


**(b)**

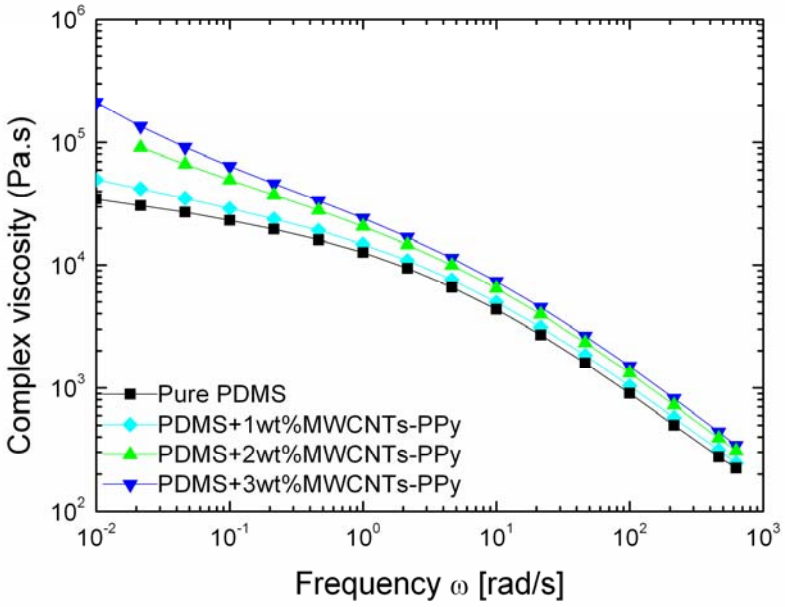


Figure 7.3: Complex viscosities of PDMS nanocomposites containing (a) MWCNTs-P, (b) MWCNTs-PPy.

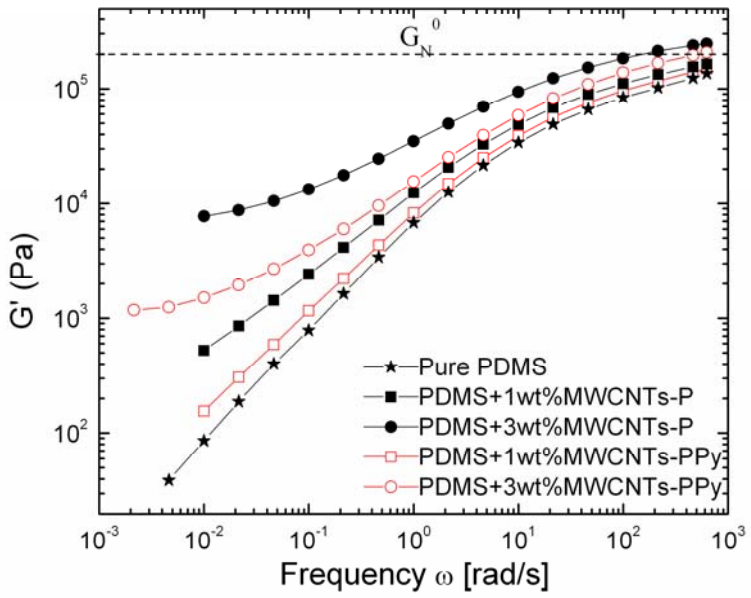


Figure 7.4: Storage modulus of PDMS nanocomposites as a function of frequency.

### 7.2.3 Gas Transport Properties of PDMS MMMs

The gas transport properties of PDMS MMMs were carried out by pressure increase setup where diffusion coefficients were measured by time lag measurements. Table 7.1 presents the permeability data of different gases through PDMS MMMs. The loading of MWCNTs-P and MWCNTs-PPy was kept as 0.5, 1, and 3 wt. %. The MMMs obtained by loading MWCNTs-P were named as MMMs-P0.5, MMMs-P1, and MMMs-P3 with respect to the contents MWCNTs-P. The membranes containing MWCNTs-PPy were named as MMMs-PPy0.5, MMMs-PPy1, and MMMs-PPy3. The values of gas permeabilities for pure PDMS membranes are in accordance with measurements reported in literature [2, 5]. The increasing order of permeability of different gases is as follows: $N_2$<$O_2$<$H_2$<$CH_4$<$C_2H_6$<$CO_2$. PDMS membranes containing poorly distributed MWCNTs-P did not show significant impact on the permeability of gases i.e. the permeability of gases remained unchanged at different loadings of MWCNTs-P. In the case of PDMS membranes containing well dispersed MWCNTs-PPy, a slight increase in permeability of all the gases was observed for

MMMs-PPy loading which decreased upon further increase in MWCNTs-PPy loading but still the permeability values were higher compared to neat PDMS membranes. This slight increase of permeability of gases can be attributed to the good dispersion of MWCNTs-PPy and presence of polyoligomeric silsesquioxane (POSS) on MWCNTs. The amount of agglomerates increases with further addition of MWCNTs-PPy beyond 0.5 wt. % loading which might be the reason for lower permeability. The selectivity of different gas pairs for PDMS MMMs was not significantly changed compared to pure PDMS membranes (Table 7.2). The values of selectivities were in agreement with pure PDMS membranes reported elsewhere [2, 5].

Table 7.1: Permeability data of different gases (measured in barrer) through PDMS MMMs at 30°C.

| Code | $N_2$ | $O_2$ | $H_2$ | $CO_2$ | $CH_4$ | $C_2H_6$ |
|---|---|---|---|---|---|---|
| Pure PDMS | 350 | 726 | 819 | 3688 | 1112 | 3133 |
| MMMs-P0.5 | 347 | 717 | 791 | 3453 | 1101 | 2917 |
| MMMs-P1 | 361 | 753 | 821 | 3804 | 1154 | 3235 |
| MMMs-P3 | 358 | 740 | 806 | 3758 | 1128 | 3197 |
| MMMs-PPy0.5 | 402 | 818 | 892 | 3909 | 1242 | 3320 |
| MMMs-PPy1 | 386 | 791 | 863 | 3773 | 1204 | 3229 |
| MMMs-PPy3 | 378 | 769 | 826 | 3578 | 1082 | 3010 |

1 barrer = $10^{-10}$ $cm^3$(STP)·cm/$cm^2$·s·cmHg.

Table 7.2: Selectivity data of different gas pairs in PDMS MMMs measured at 30°C.

| Code | $O_2/N_2$ | $CO_2/H_2$ | $CO_2/N_2$ | $C_2H_6/CH_4$ |
|---|---|---|---|---|
| Pure PDMS | 2.07 | 4.50 | 10.54 | 2.82 |
| MMMs-P0.5 | 2.06 | 4.37 | 9.95 | 2.65 |
| MMMs-P1 | 2.09 | 4.63 | 10.54 | 2.80 |
| MMMs-P3 | 2.07 | 4.66 | 10.50 | 2.83 |
| MMMs-PPy0.5 | 2.04 | 4.38 | 9.72 | 2.67 |
| MMMs-PPy1 | 2.05 | 4.37 | 9.77 | 2.68 |
| MMMs-PPy3 | 2.05 | 4.33 | 9.46 | 2.78 |

Permeability (P) is the product of diffusivity (D) and solubility (S) and can be represented by eq. 7.1:

$$P = S \cdot D \qquad 7.1$$

Permeability is dependent on the solubility and diffusivity of the gas molecules in polymeric membranes. The diffusivity of the gas molecules strongly depends on the size of the gas molecules i.e., the smaller molecules diffuse faster than the larger molecules. The diffusion coefficients of PDMS MMMs are enlisted in Table 7.3. The gas molecules with smaller kinetic diameter have the higher diffusion coefficient e.g. $H_2$. $C_2H_6$ with the largest kinetic diameter (among studied gases) has the lowest diffusion coefficient. In the case of PDMS MMMs, the diffusion coefficients of the gases reduced slightly compared to pure PDMS membranes. MWCNTs acted as solid barrier and reduced slightly the diffusion coefficients. Similar observation has been reported by Pechar for poly(imide siloxane) MMMs prepared by embedding single-walled carbon nanotubes (SWCNTs). At 1 wt. % loading of SWCNTs the diffusion coefficient decreased which was related to the impermeable behavior of the filler [17].

Table 7.3: Diffusion coefficients (D) of different gases through pure PDMS and PDMS MMMs measured at 30 °C.

| Code | D ($10^{-6}$·$cm^2$/s) | | | | | |
|---|---|---|---|---|---|---|
| | **$N_2$** | **$O_2$** | **$H_2$** | **$CO_2$** | **$CH_4$** | **$C_2H_6$** |
| Pure PDMS | 17.1 | 20.7 | 68.2 | 16.9 | 15 | 8.16 |
| MMMs-P0.5 | 16.9 | 19.95 | 62 | 16.5 | 14.65 | 8.01 |
| MMMs-P1 | 16.72 | 19.78 | 61.80 | 16.38 | 14.23 | 7.86 |
| MMMs-P3 | 16.46 | 19.81 | 61.0 | 16.43 | 14.44 | 7.76 |
| MMMs-PPy0.5 | 16.67 | 19.46 | 62.62 | 15.90 | 14.17 | 7.52 |
| MMMs-PPy1 | 16.48 | 19.30 | 62.01 | 16.26 | 13.94 | 7.50 |
| MMMs-PPy3 | 16.38 | 20.40 | 61.10 | 16.24 | 14.31 | 7.54 |

Solubility of the gases is another parameter determining their permeability. The solubility of the gases in polymeric membranes increases with increase in their molecular size. Hence, $C_2H_6$ has the highest solubility in PDMS membranes compared to the other small gas molecules (Table 7.4). The solubility of the gases increased slightly with the addition of MWCNTs. High solubility of gases

was observed for the MWCNTs-PPy incorporated membranes which might be due to their better dispersion and the presence of POSS on MWCNTs-PPy. The values of permeability, diffusivity, and solubility may still fall in the range of experimental error i.e. within 10 %. So based on this it can be stated that MWCNTs inclusion in PDMS membranes did not have significant improvement in gas separation properties.

Table 7.4: Solubility coefficient (S) of different gases for pure PDMS and PDMS MMMs measured at 30 °C.

| Code | S ($10^{-4}$·$cm^3$(STP)/ ($cm^3$.cmHg) | | | | | |
|---|---|---|---|---|---|---|
| | $N_2$ | $O_2$ | $H_2$ | $CO_2$ | $CH_4$ | $C_2H_6$ |
| Pure PDMS | 20.44 | 35.12 | 12.04 | 218.3 | 74.53 | 384 |
| MMMs-P0.5 | 20.53 | 35.94 | 12.76 | 209.27 | 75.15 | 364 |
| MMMs-P1 | 21.6 | 38.1 | 13.30 | 233 | 81.1 | 411 |
| MMMs-P3 | 21.77 | 37.41 | 13.25 | 229 | 78.16 | 412 |
| MMMs-PPy0.5 | 24.2 | 42.05 | 14.27 | 246 | 87.6 | 441 |
| MMMs-PPy1 | 23.50 | 41.04 | 13.94 | 232 | 86.43 | 431 |
| MMMs-PPy3 | 23.11 | 36.33 | 14.06 | 220 | 75.67 | 399 |

### 7.2.4 PDMS Mixed Matrix Composite Membranes (MMCMs)

The PDMS solution for MMCMs casting was comprised of toluene as solvent, Dehesive 940 as PDMS precursor, and MWCNTs as fillers. The solution was cast on a dry and wet porous polyacrylonitrile (PAN) membrane support using a dip-coating method. Wet PAN porous support was prepared by dipping the support in a water bath. Special care was taken to remove the water droplets on the membrane surface before casting of PDMS layer. Wet PAN support containing water in its porous structure rejects the penetration of PDMS solution into its porous structure. PDMS membrane cast on dry and wet PAN supports was evaluated for the membrane separation properties and surface electrical conductivity.

#### 7.2.4.1 PDMS MMCMs on Dry PAN Support

During the dip-coating process, the PDMS solution penetrates into the pores of the dry PAN substrate under the influence of capillary forces. Solution penetration leaves MWCNTs-PPy on the PAN surface which stick in the remaining PDMS. One advantage of using a dry porous support is the partial pore penetration of the solution which results in the increase of the effective percentage of MWCNTs-PPy on the membrane surface which, in turn, reduces the required quantity of MWCNTs-PPy to achieve percolation for electrical conductivity. After dip-coating the PDMS layer was cured at 70 °C for 1 h.

The PDMS coating was fabricated using MWCNTs-P and MWCNTs-PPy. A homogeneous black coating of PDMS was observed when PDMS was mixed with MWCNTs-PPy (Fig. 7.5 (b)). In contrary, the MWCNTs-P did not show homogeneous coating as black and white spots are clearly visible (Figure 7.5 (a)). It should be noted that the loading of MWCNTs-P in the digital image is twofold higher compared to MWCNTs-PPy. The homogeneous black coating, obtained using the MWCNTs-PPy, indicates the effectivity of the functionalization in terms of improvement of dispersion. The optical micrographs give a closer view of the PDMS coating (Fig. 7.6) where the connected aggregates of MWCNTs-P are present along with MWCNT-free spaces (Fig. 7.6 (a)). In contrary to these observations, the distribution of MWCNTs-PPy appears quite homogeneous on the coating surface (Fig. 7.6 (b)).

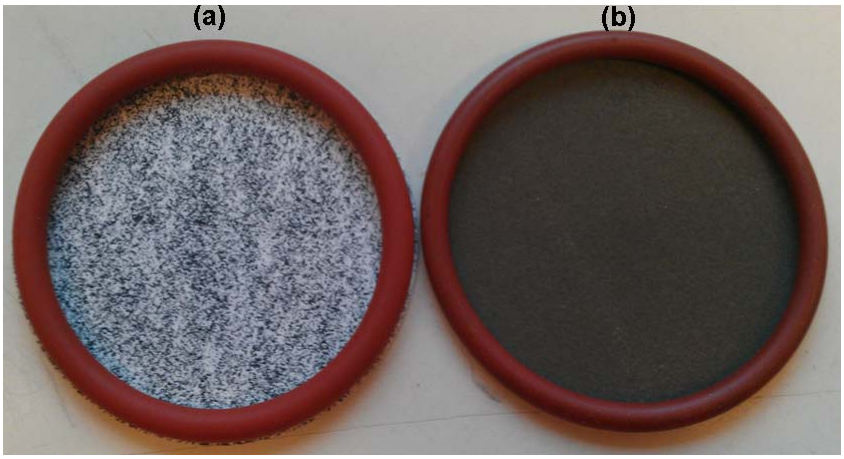


Figure 7.5: Digital photograph of PDMS MMCMs loaded with (a) 6 wt. % MWCNTs-P (b) 3 wt. % pyrene-POSS modified MWCNTs.

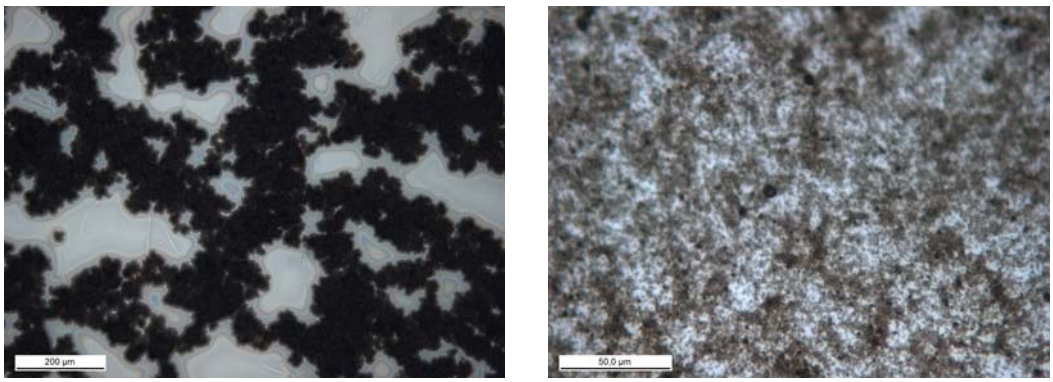


(a) (b)

Figure 7.6: Optical micrographs of PDMS MMCMs loaded with (a) 6 wt. % MWCNTs-P (scale bar 200µm) (b) 3 wt. % pyrene-POSS modified MWCNTs (scale bar 50µm).

#### 7.2.4.2 PDMS MMCMs on Wet PAN Support

In the case of a wet PAN support, MWCNTs were rejected from the casting solution during PDMS selective layer fabrication. Very few MWCNTs were picked up by wet PAN support and the rejection of MWCNTs by a wet support can be explained by the hydrophilic nature of the PAN support and hydrophobic nature of MWCNTs. Due to hydrophobic nature of MWCNTs and their agglomerates, they were rejected by the wet support. In the case of MWCNTs-P almost no MWCNTs were picked up by the wet support at the start of casting. However, with the passage of casting time the concentration of MWCNTs increased in the

casting bath. After time 't' of casting the agglomerates or even particulates of MWCNTs-P were picked up on the wet support. PDMS solution containing MWCNTs-PPy also showed the rejection behavior of MWCNTs by the wet support. However, in the case of MWCNTs-PPy, MWCNTs were picked up by the support right from the start and homogeneous light grey coating was observed for 1 wt. % MWCNTs-PPy which became darker with increase in concentration of MWCNTs in solution i.e. 3 and 5 wt. % MWCNTs-PPy. After the casting procedure, MWCNTs particulates were observed in the casting bath which clearly indicate the rejection of MWCNTs during casting and hence the effective loading of MWCNTs-PPy in the final selective layer is definitely reduced.

#### 7.2.4.3 Morphology of PDMS Selective Layer

PDMS composite membranes cast on a dry PAN support were abbreviated as $PDMS^{d}$ and those cast on wet support were abbreviated as $PDMS^{w}$. PDMS composite membranes were also prepared by loading with 1, 3, and 5 wt. % of MWCNTs-PPy. MMCMs cast on dry PAN support were abbreviated as MMCMs-$PPy1^{d}$, MMCMs-$PPy3^{d}$, and MMCMs-$PPy5^{d}$ with respect to the loading of MWCNTs-PPy. MMCMs cast on a wet PAN support were abbreviated as MMCMs-$PPy1^{w}$, MMCMs-$PPy3^{w}$, and MMCMs-$PPy5^{w}$ with respect to the loading of MWCNTs-PPy. SEM studies were carried out to analyze the surface and cross-sectional morphologies of the MMCMs. The surface and cross-sectional morphologies of the PDMS membranes, cast on a dry PAN support, can be observed in Fig. 7.7. The pure PDMS membrane has a smooth surface but it becomes rougher with the addition of MWCNTs-PPy. Although the membrane surface looks homogeneously gray for MMCMs-$PPy1^{d}$ by visual observation, however, in the SEM pictures MWCNTs-PPy agglomerates are visible on the surface along with PDMS patches. In case of MMCMs-$PPy3^{d}$ and MMCMs-$PPy5^{d}$, MWCNTs-PPy form dense carpets fixed with PDMS on the surface and in the pores. Also the color of the PDMS membranes becomes dark grey for MMCMs-$PPy3^{d}$ and black for MMCMs-$PPy5^{d}$ by visual observation. The PDMS

solution penetrates into the pores and covers the porous surface structure of the PAN membrane leading to a defect free PDMS selective layer, whereas the MWCNTs-PPy stick at the surface in the case of the MMCMs (Fig. 7.7 (b, d, f and g)). The PDMS layer of MMCMs-PPy5[d] was unstable and can be scratched off by lightly rubbing the membrane surface. The instability of PDMS layer at 5 wt. % loading is due to increased amount of MWCNTs with insufficient PDMS to bind them at the surface of PAN and it can be seen in cross-sectional view (Fig. 7.7 (h)).

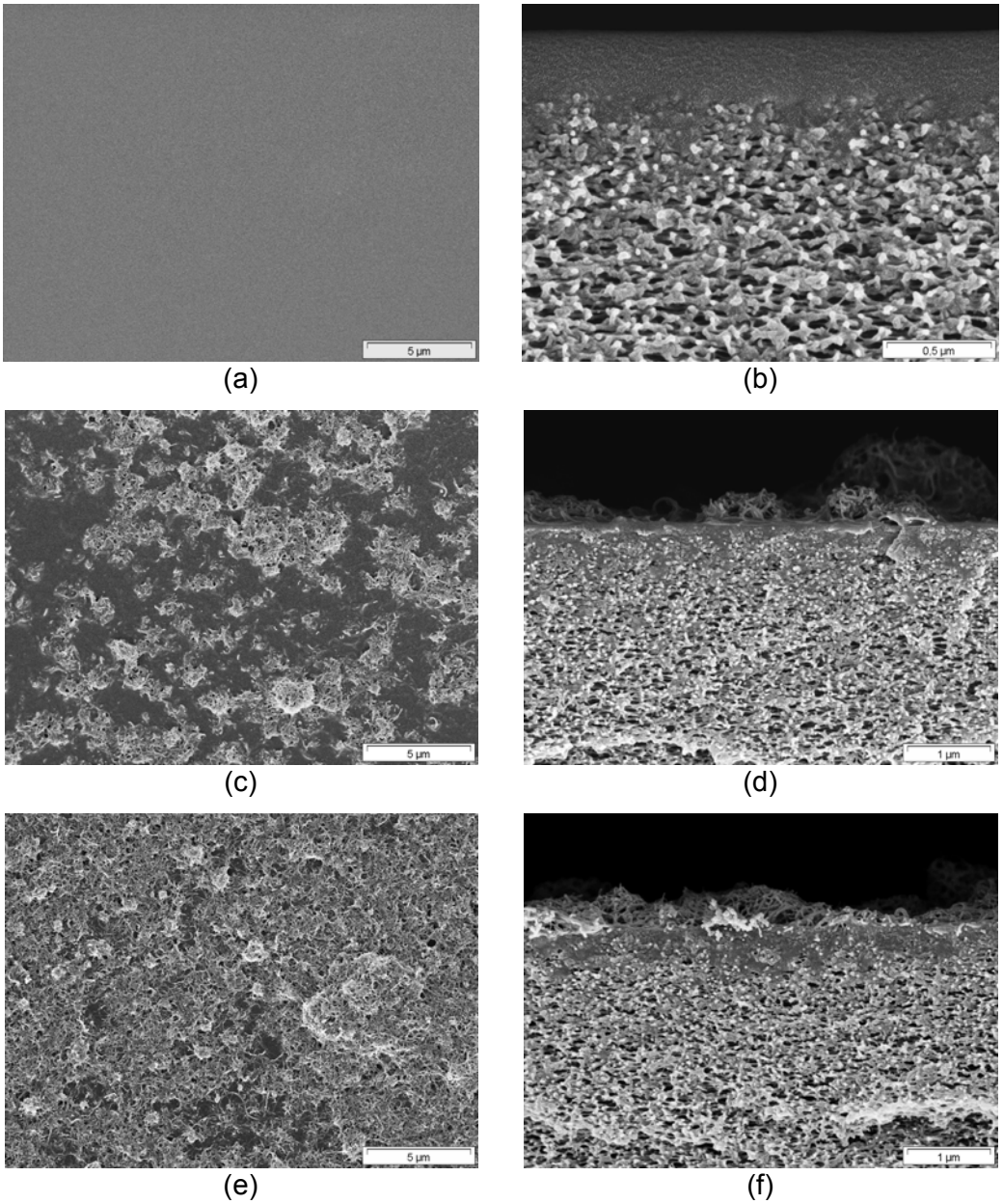


(a) (b)

(c) (d)

(e) (f)

*Figure 7.7 continued*

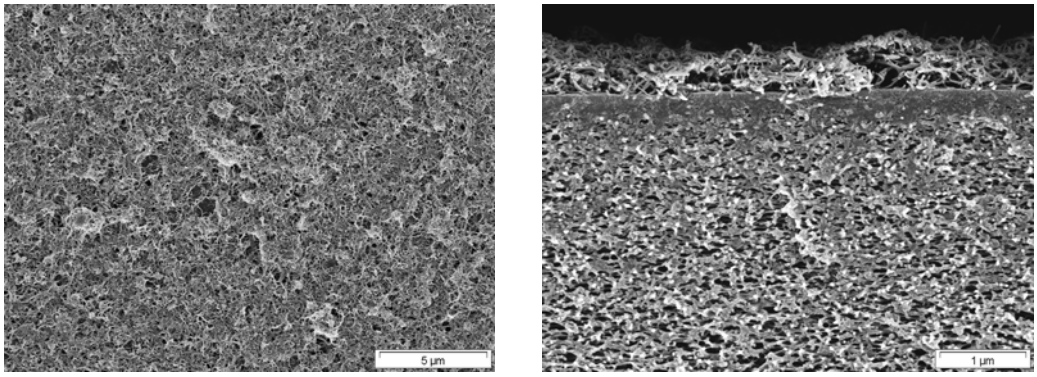


(g) (h)

Figure 7.7: Surface morphology of PDMS MMCMs cast on dry PAN support (a) PDMS$^{d}$, (c) MMCMs-PPy1$^{d}$, (e) MMCMs-PPy3$^{d}$, (g) MMCMs-PPy5$^{d}$. The corresponding cross-section morphology is shown in (b) PDMS$^{d}$, (d) MMCMs-PPy1$^{d}$, (f) MMCMs-PPy3$^{d}$, and (h) MMCMs-PPy5$^{d}$. The scale bar for surface images is 5 µm and 1 µm for cross-section images.

The surface and cross-sectional morphologies of PDMS membranes, cast on the wet PAN support, are shown in Fig. 7.8. Compared to PDMS membranes cast on a dry support, no penetration of PDMS solution into PAN pores was observed in the case of PDMS membranes cast on wet PAN support. The water filled pores of PAN restrict the entrance of solution into PAN pores. The smooth surface of PDMS$^{w}$ membranes can be observed by both surface and cross-sectional images (Fig. 7.8). The presence of MWCNTs-PPy can be viewed on the surface images of MMCMs where their agglomerates are visible at the surface. Due to MWCNTs repulsion, their fewer amounts were taken up by wet support. In the presence of MWCNTs-PPy, the surface of the membranes becomes rough which results in the membranes with non uniform thickness. MMCMs-PPy1$^{w}$ membranes showed light grey color which became darker for MMCMs-PPy3$^{w}$ and MMCMs-PPy5$^{w}$. The surface of MMCMs-PPy5$^{w}$ membranes was quite stable where MWCNTs-PPy embedded in PDMS can be observed by cross-sectional image (Fig. 7.8 (h)).

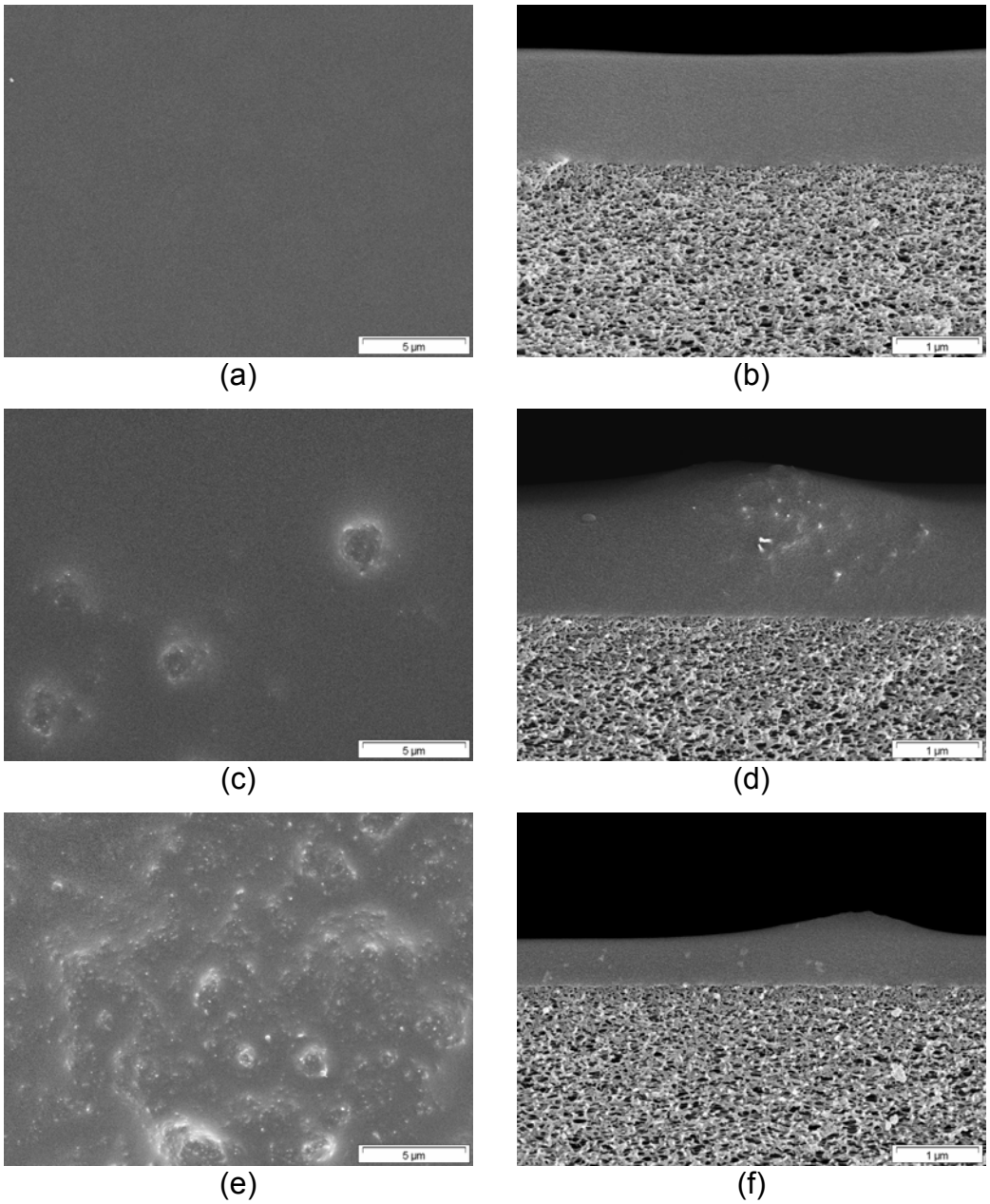


(a) (b)

(c) (d)

(e) (f)

*Figure 7.8 continued*

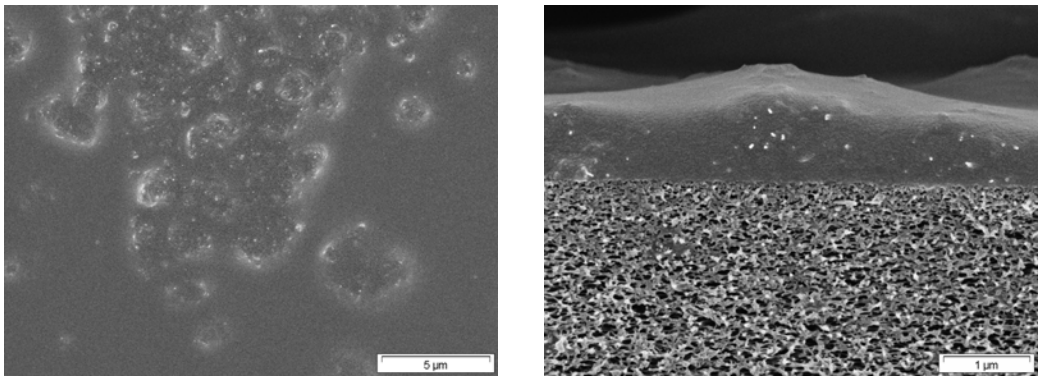


(g) (h)

Figure 7.8: Surface morphology of PDMS MMCMs cast on wet PAN support (a) PDMS$^{w}$, (c) MMCMs-PPy1$^{w}$, (e) MMCMs-PPy3$^{w}$, (g) MMCMs-PPy5$^{w}$. The corresponding cross-section morphology is shown in (b) PDMS$^{w}$, (d) MMCMs-PPy1$^{w}$, (f) MMCMs-PPy3$^{w}$, and (h) MMCMs-PPy5$^{w}$. The scale bar for surface images is 5 µm and 1 µm for cross-section images.

#### 7.2.4.4 Electrical Sheet Resistance Measurements

For measuring electrical properties, the membranes loaded with 1, 2, 3, 4, and 5 wt. % of MWCNTs-PPy were used. PDMS membranes cast on a wet support did not show any electrical conductivity even at 5 wt. % loading of MWCNTs. One possible reason for the absence of electrical conductivity property is the ineffective pick up of MWCNTs by the wet support which might have led to MWCNTs and their agglomerates having no sufficient contact points. The instrument showed contact limit during the measurement of these membranes indicating that the sheet resistance was not in the measurable range.

In the case of a PDMS membrane cast on a dry PAN support, the sheet resistance decreased upon the increase in MWCNTs-PPy content (Fig. 7.9). The percolation threshold of MWCNTs-PPy appeared at approximately 2 wt. % loading where the sheet resistance becomes lower than $10^6$ Ω/□. The decrease in sheet resistance with the addition of MWCNTs can be attributed to the sufficient contact points among the MWCNTs in the PDMS MMCMs. Electrostatic charging phenomenon can be neutralized by the surfaces having sheet resistance lower than a value in the range of $10^6$ Ω/□ and $10^9$ Ω/□ [15].

The application of conductive coatings on porous substrates like foams might improve their ability to avoid electrostatic discharge. In plastic housed spiral wound modules, electrostatic charges could be build up on the membranes surface by the friction of gas / vapor mixtures during the separation process reaching the limit of the breakthrough field strength and resulting in an electric discharge between membrane elements and causing severe membrane damage. The elimination of the static charge by a PDMS conductive coating may enhance the safety of the gas separation process in spiral wound membrane modules by dissipating / grounding the charges accumulated at the surface of the membranes.

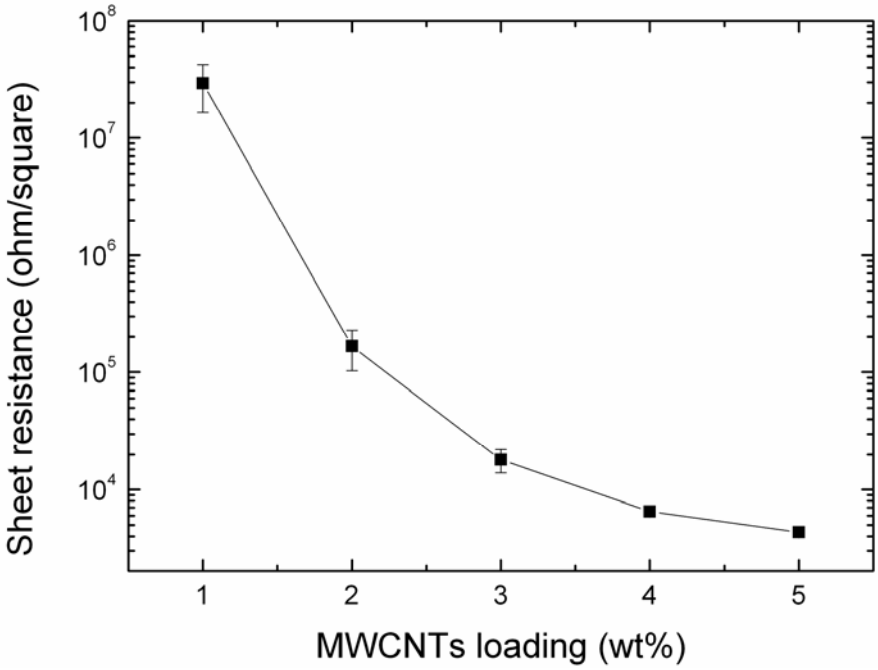


Figure 7.9: Electrical sheet resistance of PDMS membrane cast on dry PAN support as a function of MWCNTs-PPy.

#### 7.2.4.5 Gas Transport Properties of PDMS MMCMs

The characterization of the defect-free PDMS selective layer was done by gas permeance measurements. The permeance of different gases through PDMS MMCMs was measured by a “constant volume variable pressure” unit at 23 °C,

the standard method to evaluate gas fluxes through composite membranes. Table 7.5 depicts the gas permeance data of PDMS composite membranes. At 1 wt. % MWCNTs-PPy content, a slight decrease in the permeance for all gases is observable in comparison to a pure PDMS sample. With increasing MWCNTs-PPy content above 1 wt. %, the permeance increases again but does not reach the value of the pure PDMS sample even at MWCNTs-PPy content of 5 wt. %. It was shown that the dense membranes did not show significant improvement or reduction in the permeability (Table 7.1). So in the cases of MMCMs-PPy1[d] and MMCMs-PPy3[d], the decrease in permeance can be attributed to varying effective thickness of the PDMS layer. Since the solution penetrated in the porous support, so it is difficult to predict the accurate thickness of the selective layer as the extent of penetration of PDMS solution containing different amounts of MWCNTs may be different. The selectivity of the described gases remained same for composite membranes with pure PDMS layers and PDMS layers with incorporated MWCNTs-PPy (Table 7.6). The selectivity values of MMCMs are higher compared to the selectivity of different gas pairs in PDMS dense films (Table 7.2). The selectivity values clearly indicate the formation of defect-free PDMS selective layers.

Table 7.5: Permeance data of different gases for PDMS membranes cast on dry PAN support.

| Membrane | $N_2$ | $O_2$ | $CH_4$ | $CO_2$ | $C_2H_6$ |
|---|---|---|---|---|---|
| PDMS[d] | 0.53 | 1.12 | 1.73 | 6.11 | 4.98 |
| MMCMs-PPy1[d] | 0.43 | 0.93 | 1.43 | 5.10 | 4.17 |
| MMCMs-PPy3[d] | 0.46 | 1.00 | 1.53 | 5.40 | 4.42 |
| MMCMs-PPy5[d] | 0.53 | 1.11 | 1.71 | 5.97 | 4.91 |

[d]membrane cast on dry PAN support

Table 7.6: Selectivity data of different gas pairs for PDMS membranes cast on dry PAN support.

| Membrane | ($O_2/N_2$) | ($CO_2/N_2$) | ($C_2H_6/CH_4$) |
|---|---|---|---|
| PDMS[d] | 2.13 | 11.6 | 2.87 |
| MMCMs-PPy1[d] | 2.13 | 11.7 | 2.91 |
| MMCMs-PPy3[d] | 2.13 | 11.6 | 2.88 |
| MMCMs-PPy5[d] | 2.11 | 11.3 | 2.87 |

[d]membrane cast on dry PAN support

In the case of PDMS MMCMs cast on wet support, higher gas permeance values were observed compared to membranes cast on dry PAN (Table 7.7). The reason for higher permeances in case of wet support membrane is less or almost no penetration of the PDMS solution into the pores of PAN. The gas flux through the membrane depends on its thickness (eq. 7.2):

$$J_i = \frac{P_i}{l}.\Delta p \qquad 7.2$$

where '$J_i$' is the flux of a gas component 'I', '$P_i$' is the permeability, 'l' is the thickness of the membrane, and 'ΔP' is the pressure difference on the feed and permeate side. The gas flux is inversely proportional to the thickness of the membrane. From the permeance values it can be estimated that effective thickness of PDMS on dry support is higher compared to PDMS membrane cast on wet support. The gas permeance of membranes cast on wet support decreased with the loading of MWCNTs-PPy. One possible reason for the decrease of permeance is the increase in thickness of the selective layer with inclusion of MWCNTs-PPy. It is difficult to calculate the exact thickness of the PDMS selective layer containing MWCNTs-PPy because of irregular thickness (Fig. 7.8). This can be assumed on the basis of increased solution viscosities with MWCNTs-PPy i.e., higher viscous solutions might have given rise to thicker selective layers. The selectivity of different gas pairs was not influenced in the presence of MWCNTs-PPy.

Table 7.7: Permeance and selectivity data of different gases for PDMS membranes cast on wet PAN support.

| Membrane | $N_2$ | $O_2$ | $CH_4$ | $CO_2$ | $C_2H_6$ |
|---|---|---|---|---|---|
| PDMS$^w$ | 1.09 | 2.30 | 3.5 | 11 | 9.36 |
| MMCMs-PPy1$^w$ | 1.02 | 2.14 | 3.31 | 10.55 | 9.15 |
| MMCMs-PPy3$^w$ | 0.95 | 2 | 3.07 | 9.74 | 8.52 |
| MMCMs-PPy5$^w$ | 0.94 | 1.98 | 3.04 | 10.03 | 8.47 |

$^w$membrane cast on wet PAN support

Table 7.8: Selectivity data of different gas pairs for PDMS membranes cast on wet PAN support.

| Membrane | ($O_2/N_2$) | ($CO_2/N_2$) | ($C_2H_6/CH_4$) |
|---|---|---|---|
| PDMS$^w$ | 2.10 | 10.06 | 2.67 |
| MMCMs-PPy1$^w$ | 2.10 | 10.28 | 2.76 |
| MMCMs-PPy3$^w$ | 2.12 | 10.29 | 2.78 |
| MMCMs-PPy5$^w$ | 2.12 | 10.70 | 2.78 |

$^w$membrane cast on wet PAN support

#### 7.2.4.6 Effect of Temperature on Gas Permeance Properties of MMCMs

PDMS MMCMs cast on dry support were used to study the influence of temperature on the transport properties. Fig. 7.10 (a) presents the influence of temperature on the permeance of PDMS$^d$. The permeance of $N_2$, $O_2$, $H_2$, and $CH_4$ increased with the increase in temperature. However, the permeance of $CO_2$ and $C_2H_6$ decreased slightly or remained constant with an increase in temperature. Wilks et al. found the same trend of decreasing permeability of $CO_2$ with increase in temperature, in case of PDMS thick membranes [20]. Pinnau et al. reported the decrease in the permeability of $C_2H_6$ with increase in temperature for PDMS membranes [2]. In both cases, it has been reported that permeability of more condensable gases like $C_2H_6$ and $CO_2$ undergo a decrease in permeability as a function of temperature. From Fig. 7.10 (a), it is obvious that the permeance of $H_2$ increased remarkably compared to other gases which can be related to its small kinetic diameter and fast diffusion. PDMS membranes containing MWCNTs-PPy showed the similar behavior for the permeance of gases. There

was no significant change observed in permeance at any particular measurement temperature in case of MMCMs-PPy5[d] compared to PDMS[d].

The activation energy of permeation can be calculated using eq. 7.3:

$$L = L_{\circ} e^{\left(\frac{-E_p}{RT}\right)} \qquad 7.3$$

Where 'L' is the permeance, '$L_{\circ}$' is the exponential factor, '$E_p$' is the activation energy of permeation (KJ/mol), 'R' is the universal gas constant and 'T' is absolute temperature (K).

'$E_p$' can be calculated by taking the natural logarithm of permeance and plotting it against temperature. $E_p$ is calculated from the slope of the line. Table 7.9 shows the data of '$E_p$' for different gases in PDMS MMCMs. The negative values of '$E_P$' indicate the decrease in permeance with the increase in temperature. There was no significant difference in '$E_p$' values observed with or without the presence of MWCNTs-PPy. The measured '$E_p$' values are nearly in accordance with the values reported in literature except the values of $C_2H_6$ which are higher compared with reported in literature [2,20]. This deviation can arise because the values in this case are measured for thin composite membrane and they are being compared with PDMS thick films.

(a)

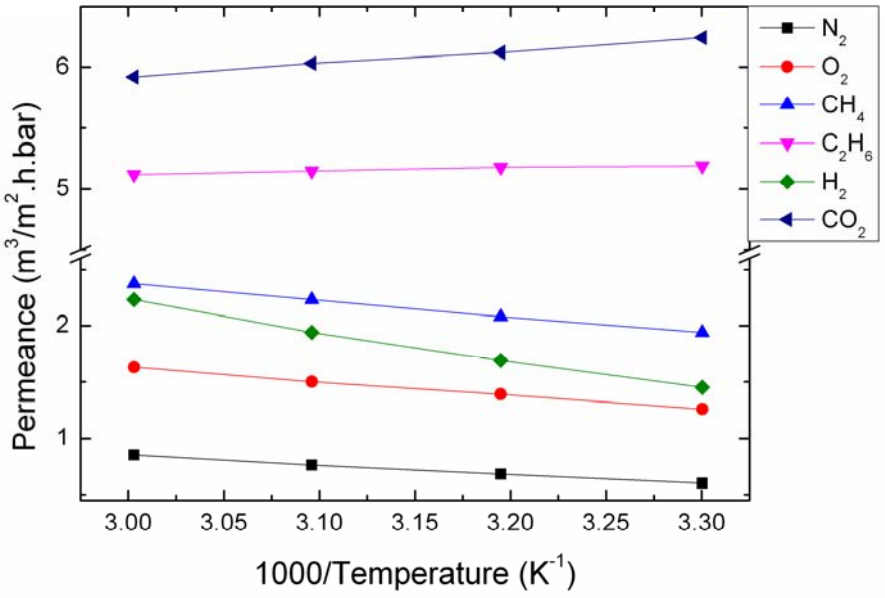


(b)

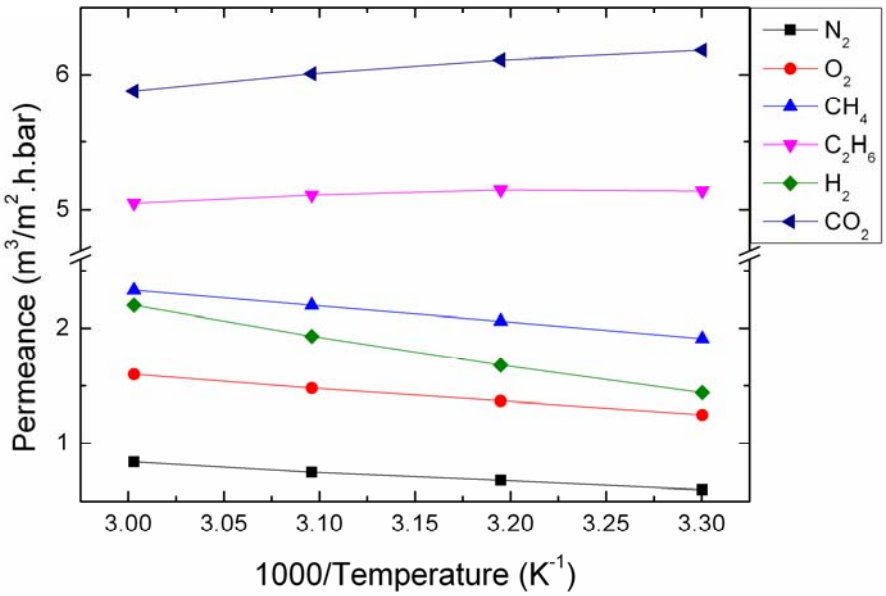


Figure 7.10: Influence of temperature on the permeance of gases through (a) PDMS[d] (b) MMCMs-PPy5[d].

Table 7.9: '$E_p$' (KJ/mol) of different gases through PDMS MMCMs cast on dry support.

| Membrane | $N_2$ | $O_2$ | $CH_4$ | $C_2H_6$ | $H_2$ | $CO_2$ |
|---|---|---|---|---|---|---|
| PDMS[d] | 9.64 | 7.06 | 5.57 | -0.38 | 11.96 | -1.44 |
| MMCMs-PPy1[d] | 9.47 | 7.89 | 5.73 | -0.7 | 12.54 | -2.07 |
| MMCMs-PPy3[d] | 9.97 | 7.23 | 5.73 | -0.14 | 12.13 | -1.18 |
| MMCMs-PPy5[d] | 9.22 | 6.81 | 5.57 | -0.49 | 11.8 | -1.33 |

The effect of temperature on the selectivity of different gas pairs is shown in Fig. 7.11. A decrease in selectivity of different gas pairs can be observed as a function of temperature. It was observed that selectivity of $CO_2$ over $H_2$ decreased drastically as a function of temperature in all the studied membranes. This trend is because of decreased permeance of $CO_2$ and increased permeance of $H_2$ as a function of temperature. The permeance trend of $CO_2$ and $H_2$ at different temperatures can be observed in Fig. 7.10. The decreased permeance of $CO_2$ is because of its condensability and lower solubility and increased permeance of $H_2$ is because of its fast diffusion as a function of temperature. These two parameters are responsible for the significant decrease in the selectivity of $CO_2$ with temperature. The selectivity of $C_2H_6/CH_4$ and $O_2/N_2$ pairs also decreased as a function of temperature. However, the trend of decrease in selectivity was of lower magnitude compared to $CO_2/H_2$.

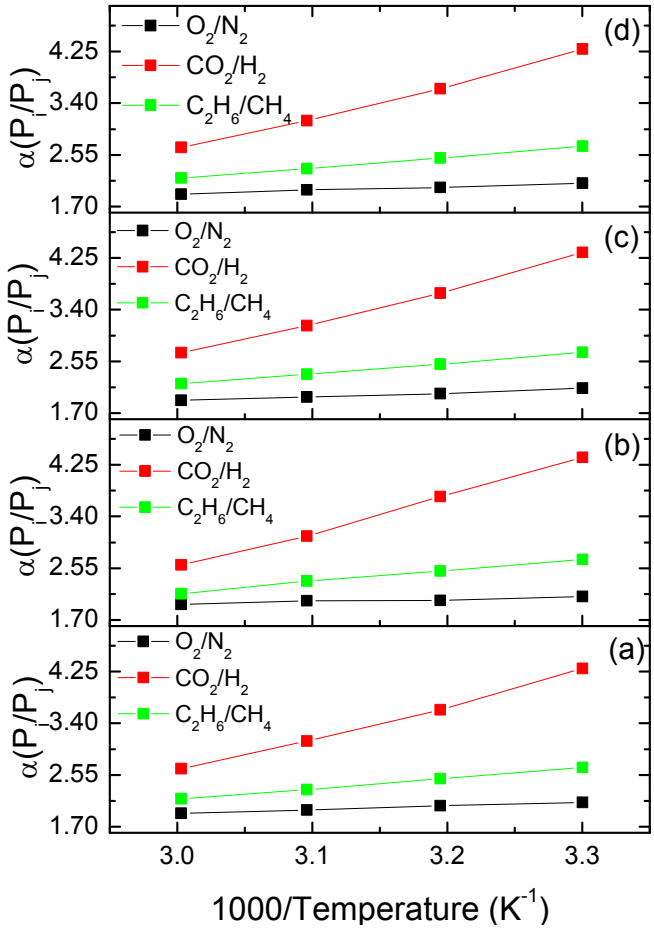


Figure 7.11: Selectivity of different gas pairs as a function temperature for (a) PDMS[d], (b) MMCMs-PPy1[d], (c) MMCMs-PPy3[d], and (d) MMCMs-PPy5[d].

### 7.2.4.7 PDMS MMCMs with PS Modified MWCNTs

PDMS MMCMs were also fabricated using PS grafted MWCNTs on a wet PAN support. MWCNTs-*gf*-PS were selected because of their stable dispersion in toluene; a solvent used in this study for the fabrication of PDMS MMCMs. MWCNTs containing less than 40 wt. % of PS contents led to their unstable dispersion in toluene. MWCNTs grafted with 40 wt. % (MWCNTs-*gf*-$PS_{40}$) and 90 wt. % (MWCNTs-*gf*-$PS_{90}$) polystyrene were used for the fabrication of membranes. The membranes fabricated using MWCNTs-*gf*-$PS_{40}$ were coded as MMCMs-$PS^{w}_{40}$ and membranes containing MWCNTs-*gf*-$PS_{90}$ were coded as MMCMs-$PS^{w}_{90}$. A good dispersion of MWCNTs was obvious visually where a homogeneous black coating of PDMS on wet PAN support was observed like

previously shown MWCNTs-PPy incorporated PDMS MMCMs (Fig. 7.5 (b)). The permeance data of the MMCMs containing MWCNTs-*gf*-PS is shown in Table 7.10:

Table 7.10: Gas permeance data of PDMS MMCMs containing MWCNTs-*gf*-$PS_{40}$ and MWCNTs-*gf*-$PS_{90}$.

| Code | MWCNTs-*gf*-PS loading (wt. %) | $N_2$ | $O_2$ | $CH_4$ | $CO_2$ | $C_2H_6$ |
|---|---|---|---|---|---|---|
| $PDMS^w$ | - | 1.09 | 2.30 | 3.5 | 11 | 9.36 |
| MMCMs-PS-$0.5_{40}{}^w$ | 0.5 | 1.01 | 2.16 | 3.30 | 11.39 | 9.46 |
| MMCMs-$PS2_{40}{}^w$ | 2 | 0.94 | 1.99 | 3.04 | 10.51 | 8.66 |
| MMCMs-$PS5_{40}{}^w$ | 5 | 0.87 | 1.83 | 2.90 | 9.76 | 8.0 |
| MMCMs-$PS20_{40}{}^w$ | 20 | - | - | - | - | - |
| MMCMs-$PS0.5_{90}{}^w$ | 0.5 | 0.88 | 1.86 | 2.85 | 9.72 | 7.95 |
| MMCMs-$PS2_{90}{}^w$ | 2 | 0.75 | 1.59 | 2.42 | 8.37 | 6.88 |
| MMCMs-$PS5_{90}{}^w$ | 5 | 0.28 | 0.61 | 0.91 | 3.24 | 2.60 |

Table 7.11: Gas selectivity data of PDMS MMCMs containing MWCNTs-*gf*-$PS_{40}$ and MWCNTs-*gf*-$PS_{90}$.

| Code | MWCNTs-*gf*-PS loading (wt. %) | ($O_2/N_2$) | ($CO_2/N_2$) | ($C_2H_6/CH_4$) |
|---|---|---|---|---|
| $PDMS^w$ | - | 2.11 | 10.06 | 2.67 |
| MMCMs-PS-$0.5_{40}{}^w$ | 0.5 | 2.14 | 11.27 | 2.86 |
| MMCMs-$PS2_{40}{}^w$ | 2 | 2.12 | 11.18 | 2.84 |
| MMCMs-$PS5_{40}{}^w$ | 5 | 2.10 | 11.21 | 2.76 |
| MMCMs-$PS20_{40}{}^w$ | 20 | - | - | - |
| MMCMs-$PS0.5_{90}{}^w$ | 0.5 | 2.11 | 11.04 | 2.79 |
| MMCMs-$PS2_{90}{}^w$ | 2 | 2.12 | 11.16 | 2.84 |
| MMCMs-$PS5_{90}{}^w$ | 5 | 2.18 | 11.57 | 2.85 |

A depression in permeance was observed with the addition of MWCNTs-*gf*-PS which was very prominent in case of membranes containing MWCNTs-*gf*-$PS_{90}$. The decrease in permeance of the membranes can be attributed to the presence of PS on MWCNTs. The increased amount of glassy polymer affected the permeance of PDMS membranes; however, the selectivity of different gas pairs did not change (Table 7.11). PDMS membranes fabricated using 20 wt. % of MWCNTs-*gf*-$PS_{40}$ showed defects and gas permeance measurement was not possible.

Electrical sheet resistance of PDMS membranes containing MWCNTs-*gf*-PS was beyond the limit of the measurement setup. There was no electrical conductivity found for PDMS composite membranes even loaded with 20 wt. % MWCNTs-*gf*-$PS_{40}$. The reason for the absence of electrical conductivity might be the shielding effect of PS on MWCNTs. Ma et al. reported the electrical properties of MWCNTs / epoxy nanocomposite filled with non-modified and epoxy silane modified MWCNTs [21]. In the case of silane modified MWCNTs no significant improvement was observed in the conductivity values up to a loading of 0.5 wt. % compared to the pure epoxy. However, untreated MWCNTs showed an increase in electrical conductivity. Low electrical conductivity of nanocomposites, containing epoxy silane modified MWCNTs, was due to covalent anchoring of epoxy silane on MWCNTs. Epoxy silane reacts with amine hardener leading to the attachment of epoxy chains of the matrix on MWCNTs after curing. The attachment of polymer perturbed $\pi$ electronic structure of MWCNTs and resulted in the significantly lower electrical conductivity compared to the untreated MWCNTs.

## 7.3 Conclusions

PDMS MMMs were prepared by incorporating purified and functionalized MWCNTs. Pyrene-POSS modified MWCNTs (MWCNTs-PPy) showed a better dispersion compared to purified MWCNTs (MWCNTs-P). Pyrene-POSS stacking on MWCNTs decreased the intertube interactions leading to a better dispersion of MWCNTs-PPy in PDMS MMMs. The complex viscosity and storage modulus of the nanocomposites increased with the addition of MWCNTs-P and MWCNTs-PPy. However, complex viscosity and storage modulus of PDMS nanocomposites, incorporated with MWCNTs-P, were higher compared to nanocomposites incorporated with MWCNTs-PPy. This might be due to better interactions of MWCNTs-P with PDMS. The shielding effect of pyrene-POSS stacked on MWCNTs might be the reason for weaker interactions of PDMS and MWCNTs-PPy. The gas transport properties of PDMS dense membranes,

loaded with purified and functionalized MWCNTs, did not increase or decrease significantly compared to pure PDMS membranes. Also, the selectivity of gas pairs ($O_2/N_2$, $CO_2/N_2$, and $C_2H_6/CH_4$) did not change upon the addition of MWCNTs in PDMS. The addition of MWCNTs in PDMS did not influence the solubility or diffusivity of gases significantly.

PDMS composite membranes were fabricated on dry and wet PAN support. MWCNTs uptake on wet PAN support was not efficient compared to dry PAN support because of MWCNTs repulsion on wet support. The better dispersion of MWCNTs-PPy was observed compared to MWCNTs-P. PDMS membranes showed irregular surface with the addition of MWCNTs. PDMS membranes cast on dry support showed electrical conductivity which increased as a function of MWCNTs while the membranes cast on wet support showed insulating behavior. The absence of electrical conductivity might be because of insufficient pick up of MWCNTs by wet support leading to no or very less contact points among MWCNTs. Higher gas permeance values of PDMS composite membranes cast on a wet PAN support were observed compared to PDMS membranes cast on a dry support. The decreased permeance of gases in dry PAN support indicates the increased effective thickness of the selective layer. The selectivity of different gas pairs also did not change significantly with the addition of MWCNTs. The gas permeance values decreased with the addition of polystyrene modified MWCNTs. Incorporation of MWCNTs grafted with 90 wt. % polystyrene showed prominent decrease in gas permeance compared to MWCNTs grafted with 40 wt. % MWCNTs. The decrease in permeance of gases is because of the glassy polystyrene phase attached to MWCNTs. PDMS composite membranes grafted with polystyrene did not show surface electrical conductivity, most likely because of shielding.

## 7.4 References

[1] S. P. Nunes, K. V. Peinemann, Membrane Technology in the Chemical Industry, 2nd edi., Wiley-VCH, 2006.

[2] I. Pinnau, Z. He, J. Membr. Sci., 244 (2004) 227-233.

[3] M. Sadrzadeh, K. Shahidi, T. Mohammadi, J. Appl. Polym. Sci., 117 (2010) 33-48.
[4] I. Blume, P. Schwering, M. Mulder, C. Smolders, J. Membr. Sci., 61 (1991) 85-97.
[5] T. Merkel, R. Gupta, B. Turk, B. Freeman, J. Membr. Sci., 191 (2001) 85-94.
[6] M. Mulder, Basic Principles of Membrane Technology, 2nd edi., Kluwar Publishers, 1996.
[7] L. M. Robeson, J. Membr. Sci., 62 (1991) 165-185.
[8] S. Sanip, A. Ismail, P. Goh, T. Soga, M. Tanemura, H. Yasuhiko, Separ. Purif. Technol., (2011) 208-213.
[9] S. Kim, L. Chen, J. K. Johnson, E. Marand, J. Membr. Sci., 294 (2007) 147-158.
[10] A. Fonseca, S. Reijerkerk, J. Potreck, K. Nijmeijer, Z. Mekhalif, J. Delhalle, Desalination, 250 (2010) 1150-1154.
[11] A. Ismail, P. S. Goh, S. Sanip, M. Aziz, Separ. Purif. Technol., 70 (2009) 12-26.
[12] M. Jia, K. V. Peinemann, R. D. Behling, J. Membr. Sci., 57 (1991) 289-292.
[13] D. M. Ackerman, A. I. Skoulidas, D. S. Sholl, J. K. Johnson, Mol. Simulat., 29 (2003) 677-684.
[14] S. Kim, T. W. Pechar, E. Marand, Desalination, 192 (2006) 330-339.
[15] M. Narkis, G. Lidor, A. Vaxman, L. Zuri, J. Electrostatics, 47 (1999) 201-214.
[16] J. Sandler, M. Shaffer, T. Prasse, W. Bauhofer, K. Schulte, A. Windle, Polymer, 40 (1999) 5967-5971.
[17] T. W. Pechar, Virginia Polytechnic and State University (2004).
[18] Y. S. Song, J. R. Youn, Carbon, 43 (2005) 1378-1385.
[19] A. Beigbeder, M. Linares, M. Devalckenaere, P. Degée, M. Claes, D. Beljonne, R. Lazzaroni, P. Dubois, Adv. Mater., 20 (2008) 1003-1007.
[20] B. Wilks, M. E. Rezac, J. Appl. Polym. Sci., 85 (2002) 2436-2444.
[21] P. C. Ma, J. K. Kim, B. Z. Tang, Composites Sci. Technol., 67 (2007) 2965-2972.

## Chapter 8. Summary

Attempts to improve the membrane separation performance have led to an important class of membranes known as mixed matrix membranes (MMMs). It is an emerging class of membranes with inorganic fillers embedded in polymer matrix. The addition of inorganic fillers provides a way for better membrane mechanical stability and permeability and / or selectivity. The main goal of this study was the fabrication and characterization of MWCNTs containing mixed matrix polymeric membranes with the aim of improving the mechanical stability, separation performance, and electrical conductivity of the membranes. Purified MWCNTs (MWCNTs-P) and functionalized MWCNTs were embedded in poly(vinylidene fluoride) (PVDF), polyacrylonitrile (PAN), and poly(dimethylsiloxane) (PDMS) to fabricate the membranes. PVDF and PAN integral asymmetric membranes were prepared via water induced phase inversion process while dense PDMS membranes were prepared by solvent evaporation.

Functionalization of MWCNTs was employed to improve their dispersibility in organic solvents and in resultant membranes. Surface functionalization of MWCNTs was carried out via non-covalent / physical and covalent / chemical functionalization method. For non-covalent functionalization, pyrene-POSS was used as dispersant. Pyrene-POSS nanohybrid dispersant was prepared by amidation reaction between 1-pyrenebutyric acid and aminopropylisobutyl POSS. NMR and FTIR spectroscopy confirmed the successful synthesis of the dispersant. TGA confirmed the adsorption of pyrene-POSS on MWCNTs (MWCNTs-PPy). Silicone mapping of functionalized MWCNTs showed the presence of POSS moiety adsorbed on MWCNTs surfaces. Pyrene-POSS enabled stable dispersion of MWCNTs in THF, *n*-hexane, chloroform, and toluene. Covalent functionalization of MWCNTs was performed by grafting polystyrene (PS) and poly(methyl methacrylate) (PMMA) under ATRP conditions via “grafting from” technique (MWCNTs-*gf*-PMMA and MWCNTs-*gf*-PS). The polymer content on MWCNTs was controlled by varying the reaction duration.

The successful grafting of PMMA and PS from MWCNTs was observed by TGA and FTIR analysis. TEM analysis confirmed the presence of grafted polymer on MWCNTs. PS and PMMA modified MWCNTs showed stable dispersion in THF and chloroform. PMMA was also grafted onto MWCNTs via “grafting onto” technique (MWCNTs-*gt*-PMMA). MWCNTs-*gt*-PMMA showed a low polymer content and less grafted density compared to MWCNTs-*gf*-PMMA.

PVDF membranes were prepared by incorporating MWCNTs-P, hydroxyl functionalized (MWCNTs-OH), and PMMA functionalized (MWCNTs-*gf*-PMMA, and MWCNTs-*gt*-PMMA). The viscosity of the PVDF solution increased with the addition of MWCNTs. The viscosity of PVDF solution containing MWCNTs-*gf*-PMMA was comparatively lower which was related to the presence of MWCNTs aggregates. The aggregation of MWCNTs-*gf*-PMMA resulted during ATRP reaction on MWCNTs bundles. The better dispersion of MWCNTs-OH and MWCNTs-*gt*-PMMA was observed in PVDF membranes compared to MWCNTs-P and MWCNTs-*gf*-PMMA. The addition of MWCNTs to PVDF led to membranes with large surface pore size but relatively low pore density compared to pure PVDF. The cross-section morphology indicated the decrease in macrovoid size with the addition of MWCNTs. The surface electrical conductivity of PVDF membranes, incorporated with MWCNTs-P, was higher compared to functionalized MWCNTs. The structural defects on functionalized MWCNTs and the shielding effect of polymer chains resulted in a decrease in electrical conductivity of PVDF membranes. Water permeance of all PVDF membranes decreased with time. Addition of MWCNTs to PVDF resulted in an increase of water permeance at the start of the measurement. After 3 hours measurement, water permeance was slightly higher compared to pure PVDF membranes. PVDF MMMs did not show a significant improvement in resistance against compaction which was due to ineffective load transfer from polymer to MWCNTs. The prepared PVDF membranes showed 100 % rejection of ~ 50 nm sized PS nanoparticles dispersed in water.

PAN membranes were fabricated by incorporating MWCNTs-P and MWCNTs-OH. The addition of MWCNTs increased the viscosity of PAN solution. MWCNTs-OH showed better dispersion in PAN membranes compared to MWCNTs-P. The hydroxyl functional groups on MWCNTs overcome the van-der-Waals and $\pi-\pi$ stacking interactions among MWCNTs thus leading to a better dispersed system compared to MWCNTs-P. The separation performance of PAN membranes with MWCNTs-OH was better than PAN membranes with MWCNTs-P. Molecular weight cut-off (MWCO) of PAN membranes, incorporated with MWCNTs-OH, was 50 Kg/mol. The addition of MWCNTs-OH resulted in membranes with lesser and bigger macrovoid structures in cross-section. The surface pore size was not significantly changed with the addition of MWCNTs-OH. The resistance against compaction of PAN membranes incorporated with MWCNTs-OH was higher compared to MWCNTs-P. The tensile properties of PAN membranes increased significantly with the addition of MWCNTs-OH. The improvement in tensile properties and resistance against compaction resulted from the non-covalent interactions of MWCNTs-OH with PAN and lower porosity of the membranes. Incorporation of MWCNTs-P and MWCNTs-OH in PAN membranes did not show surface electrical conductivity at a maximum loading of 2 wt. %. The absence of electrical conductivity was due to insufficient contact points among MWCNTs.

PDMS membranes were prepared by the solvent evaporation method. MWCNTs-PPy and MWCNTs-P were incorporated in PDMS membranes. MWCNTs-P showed bad dispersion in PDMS films, where the aggregates of MWCNTs were visually visible at low MWCNTs-P loading. MWCNTs-PPy showed a better dispersion in PDMS membranes compared to MWCNTs-P. Surface modification of MWCNTs reduced the intertube interactions which led to the stable dispersion of MWCNTs-PPy in solvents like toluene and good dispersion in resultant membranes. The complex viscosity and storage modulus of the membrane material increased with the addition of MWCNTs. The extent of increase in complex viscosity and storage modulus was higher in the case of PDMS

containing MWCNTs-P compared to MWCNTs-PPy. The shielding effect of pyrene-POSS adsorbed on MWCNTs reduced both storage modulus and complex viscosity. The addition of MWCNTs did not change the membrane separation performance significantly. However, a slight improvement in gas permeability was found in PDMS membranes loaded with MWCNTs-PPy. PDMS composite membranes were prepared by casting polymer solution on PAN support. PDMS composite membranes, cast on dry PAN support, showed surface electrical conductivity which increased upon the addition of MWCNTs-PPy. PDMS composite membranes did not show significant change in selectivity of different gas pairs measured at different temperatures. Composite membranes prepared by incorporating MWCNTs-*gf*-PS showed a decrease in permeance of gases with the degree of loading. The decrease in permeance was due to presence of glassy polymer on MWCNTs-*gf*-PS. Although MWCNTs-*gf*-PS showed better dispersion in PDMS membranes, the absence of electrical conductivity was not found even at a loading of 20 wt. % of MWCNTs-*gf*-PS. The shielding effect of PS grafted layer on MWCNTs led to the absence of electrical conductivity.

The fabrication of MWCNTs MMMs was successfully achieved. Functionalization of MWCNTs gave rise to their better dispersion in a membrane matrix. PAN ultrafiltration membranes with better separation performance were fabricated using functionalized MWCNTs. PVDF and PDMS membranes showed an electrically conductive surface. Membranes with a conductive surface can be used in spiral wound membrane modules made of plastic housing. The conductive membranes can provide the safety in gas separation against static charges. The improved dispersibility of functionalized MWCNTs can be utilized for the fabrication of polymer coatings for electrostatic discharge ESD applications.

PAN MMMs showed insulating behavior at the maximum possible loading of MWCNTs. In order to obtain PAN conductive membranes, the future approach

can be the lowering of polymer solution concentration and increasing the loading of MWCNTs. The possibility for the improvement of gas separation of PDMS membranes can be the utilization of shortened MWCNTs. The short sized and open ended MWCNTs can lead the passage of gases though the MWCNTs interiors giving rise to higher diffusivities of gases which can improve their permeability. The shortened MWCNTs can also play an important role for the fabrication of thin layered composite membranes where the length of MWCNTs lower or comparable to the selective layer may provide the possibility of some fraction of aligned MWCNTs which can improve the gas flux.

**Acknowledgements**

I am greatly thankful to Prof. Volker Abetz for providing me the opportunity to carry out my PhD work at Helmholtz-Zentrum Geesthacht. His continuous encouragement for new ideas, valuable inputs, and patience enabled me to compile my work. He has been quite friendly and kind during discussions which gave me a lot of confidence.

I would like to thank Dr. Volkan Filiz, Head of PMS department, for his guidance and support during the work. Although, I joined PMS group last year but his friendly and helping attitude made me fit in PMS. Dr. Adriana Boschetti-de-Fierro, former Head of department PMM, is greatly acknowledged for her inputs in the work. Her communication and collaboration contributed a lot in my work.

I am indebted to Dr. Sergey Shishatskiy for his help during gas separation measurements and useful suggestions for modeling studies of carbon nanotubes. I am thankful to Dr. Julio Albuerne for his guidance and support to carry out polymerization reactions on carbon nanotubes. My special thanks go to Dr. Daniel Fierro and Kristian Buhr who helped me in porous membrane fabrication and evaluation of the results.

I would like to thank Clarissa Abetz for TEM analysis, especially her dealing with porous membrane samples which were not easy to prepare and measure. Jan Wind, Holger Pingel, and Gunter Lührs are acknowledged for their support during composite membrane fabrication. Very special thanks goes to Maren Brinkmann for GPC analysis, Silvio Neumann and Dr. Mona Wambach for NMR measurements, Karen-Marita Prause, Sabrina Bolmer, and Anne Schröder for SEM analysis, Carsten Scholles for pressure increase instrument, Berthold Wendland and Martin Kroll for providing their quick assistance in the Labs, and Joachim Koll for his help in evaluation of surface pore size analysis.

I am thankful to PMT, PMM, and PMS group members for their support in my work and keeping a nice and pleasant working environment. My office mate, Bahadir Gacal, has been quite cooperative and had nerves to share the place with me. I would like to thank my friends and colleagues specially Bing Du, Ahnaf Usman Zillohu, Dr. Rakibul Kabir, Dr. Prokopios Georgopanos, Mushfequr Rahman, and Muntazim Khan for their support and making my stay pleasant at HZG.

Financial support from EU project HARCANA under the Grant Agreement No. NMP3-LA-2008-213277 is greatly acknowledged.

I would like to thank my parents, sisters, and brother for their affection and moral support throughout my career. My wife and son are hearty acknowledged for their patience and moral support.